2017

Manipulating physical properties of complex materials by processing

Mohammad Saghayezhian
Louisiana State University and Agricultural and Mechanical College, m.saghayezhian@gmail.com

MANIPULATING PHYSICAL PROPERTIES OF COMPLEX MATERIALS BY PROCESSING

A Dissertation

Submitted to the Graduate Faculty of the
Louisiana State University and
Agricultural and Mechanical College
in partial fulfillment of the
requirements for the degree of
Doctor of Philosophy

in

Department of Physics and Astronomy

by
Mohammad Saghayezhian
B.Sc., Shahed university, 2008
M.Sc., Isfahan university of Technology, 2011
May 2017

Acknowledgments

The present work would have been impossible without the guidance and help of so many people. I have always been trying to learn from my peers, especially benefiting from their experience. Having wonderful mentors at LSU made this task feasible for me.

I would like to express my deepest gratitude to my advisors Prof. Ward Plummer and Prof. Jiandi Zhang for their unwavering support, collegiality and mentorship throughout this work. Their patience, substantial insight and immense knowledge have paved my way through this work. Learning critical and innovative thinking would be the most precious thing that I learned from them.

I am extremely grateful to Prof. Rongying Jin. I cannot thank her enough for her generosity in sharing her lab with us and valuable suggestions throughout this work.

My sincere thanks also goes to Prof. Ilya Vekhter for many many fruitful discussions, in class and outside. He helped me to clearly see what I did not know and also understand better what I thought I knew. I thank my committee member Prof. Ye Xu for his helpful comments on the thesis. Also, I would like to thank Prof. Mark Jarrell and Prof. Juana Moreno, their advice and wisdom helped me to find my passion in physics.

I have been privileged with having the best friends and labmates. Their help and encouragement was elemental for this work. My dearest friends Dr. Mostafa Siadat Mousavi and Dr. Arash Karimpour, their support, encouragement and kind advice helped me to power through the ups and downs of life in graduate school. Dr. Hangwen Guo, Dr. Chen Chen and Dr. Fangyang Liu, with them the lab was just like home, filled with kindness and joy, I cannot thank them enough for sharing their valuable experience with me. I thank my good friends Dr. Jisun Kim, Dr. Zhenyu Diao, Dr. Zhenyu Zhang, Dr. Lina Chen, Dr. Guixin Cao, Gaomin Wang, Guorong Li, Weimei Xie, David Howe,

Joel Taylor, Yifan Yang and Jiayung Pan.

Last but not least, from the bottom of my heart, I send my sincere gratitude to my wife Zahra Chinipardaz and my family. Their love and endless support is the reason for all of my achievements.

Table of Contents

List of Tables

List of Figures

Abstract

Transition metal oxides (TMOs) are a class of materials in which charge, orbital, spin and lattice strongly interact with each other. In the present thesis, a special attention is paid to the physical properties of TMOs as a function of processing. First, TMOs are studied as substrates, where the surface is of prime importance. Second, the thin films are fabricated and their physical properties are presented.

The $SrTiO_3$ (001) and (111) surfaces are weakly and strongly polar and the free energy of intact surfaces should diverge. It is shown that in TiO_2 terminated $SrTiO_3$ (001) the top most layer shows rumpling of O and Ti atoms. Rearrangement of atoms at the surface is one way of minimizing the surface free energy and avoiding polar catastrophe. In the case of $SrTiO_3$ (111), we have systematically investigated the annealing effect on the structure and composition of the polar surface of $SrTiO_3$ (111). Heteroepitaxial growth of transition-metal oxide films on the open (111) surface of $SrTiO_3$ results in significant restructuring due to the polar mismatch. Using processing condition that we found for $SrTiO_3$ (111), we have solved the polar catastrophe issue that occurs between materials with polar mismatch.

we have studied $La_{0.67}Sr_{0.33}MnO_3/SrTiO_3$ (001) under specific processing conditions and found a new interfacial magnetic interaction which is primarily driven by broken symmetry in oxide heterostructures. We show direct evidence that the symmetry breaking between conventional ferromagnetic metal and diamagnetic band insulator leads to dramatic modification of structure and chemistry at the interface. As a result, antiferromagnetic coupling emerges at the interface region which leads to spontaneous magnetic reversal and inverted hysteresis persisting well above room temperature. By further processing the $La_{1-x}Sr_xMnO_{3-\delta}$ thin films, it was shown that fine control of growth parameters can drastically change the physical properties of transition metal oxides. Magnetic properties of $La_{1-x}Sr_xMnO_{3-\delta}$ was shown to differ from the target material

$La_{0.67}Sr_{0.33}MnO_3$. Appearance of exchange bias, inverted hysteresis and spontaneous magnetic reversal once more show that intimate competition in electronic, spin and lattice degrees of freedom in transition metal oxides can lead to new functionality, even in a monolithic thin film.

Chapter 1
Intoduction

The physical properties of transition metal oxides (TMO) have been in the center of attention of physicists and engineers at least for the past half a century. Despite the age of the subject, these materials still keep amazing and sometimes confusing the scientists. In TMOs, electrons, spins and lattice strongly interact with each other. Concomitantly, an incredible variety of functional properties, unattainable in conventional semiconductors, emerges such as metal-insulator transition, superconductivity and colossal magnetoresistence. With the advent of state-of-art experimental methods to fabricate heterostructures from TMOs, it has been possible to create functionalities that was not possible to achieve in any of hererostructures constituents. It is fascinating that each of TMOs present such a rich physical properties. When two TMOs come together and form an interface, even more exciting physics start to emerge and most the times, it is completely unexpected. Famous example is the superconductivity, 2 dimensional electron gas and ferromagnetism all happening at the interface of $LaAlO_3/SrTiO_3$ [14–16]. In TMOs, while displaying a remarkable diversity in physical properties, their underlying crystal structure is similar, creating a unique opportunity for fabrication of various heterostructures. This has attracted a tremendous cumulative effort in academia as well as industry to explore and study them.

The physical properties of TMOs heavily depend on growth and processing condition. Famous example is $LaMnO_3$ which it is a well-known antiferromagnetic Mott insulator. However, depending on the growth and processing condition, as it will be discussed in chapter 6, it shows ferromagnetism and metallicity. In thin films of TMOs, in addition to growth condition and processing, the substrate plays a pivotal role as well. Therefore,

prior to growth, understanding the physical properties of the substrate is a key to a successful thin film growth. In this thesis, the surface and interface of TMOs and their emergent properties are studied as a function of processing condition. Our goal is to control and understand the underlying physical properties and look for new physical properties and functionalities.

In chapter 2, the instruments used in this thesis are introduced. In chapter 3, a detailed attention is paid to photoemission spectroscopy as this technique is used to understand the electronic properties and stoichiometry at the surface and bulk of studied materials. Chapter 4, focuses on the polar surfaces and interfaces. The polarity at the surface of TMOs is of great importance since it will affect interfacial properties. $SrTiO_3$ is widely used as a substrate and therefore understanding its surface is of prime importance. The surface of $SrTiO_3$ in (001) and (111) direction shows weak and strong polarity, respectively. The evolution of the surface as a function processing and growth condition is studied. It will be shown how these surfaces compensate their polarity and minimize their surface energy. In the second part of Chapter 4, the polar interface of $LaNiO_3/SrTiO_3$ (111) is studied. The polar catastrophe at this interface is studies and it is shown that it could be avoided by proper processing conditions. In Chapter 5, the different magnetic interactions and magnetic phase are introduced and provides theoretical foundation for the forthcoming chapters. Chapter 6 is dedicated to understanding the role of broken symmetry at the interface of $La_{0.67}Sr_{0.33}MnO_3/SrTiO_3$ (001). A surprising functionality is revealed which underscores the importance of interface interactions. Finally in chapter 7, it is shown by controlling the thermodynamic condition prior and after growth, a new magnetic structure emerges that shows exchange bias, inverted hysteresis and spontaneous magnetic reversal.

Chapter 2
Review of Instruments

In this chapter I will review the basic principles of laboratory instruments that I will be using for my thesis.

2.1 Electron Diffraction for surface structure characterization

To understand the surface structure, based on scattering methods, electrons and photons can be used. Both method rely on diffraction. In case of electrons, one can use either low energy electron diffraction (LEED) or reflection high energy electron diffraction (RHEED). As the name of these two methods suggests, one relies on low energy electrons ($20 < \mathrm{E_{electrons}(eV)} < 1000$) while the other relies on high energy electrons ($10^4 < \mathrm{E_{electrons}(eV)} < 10^6$). As is seen in fig.2.1, the scattering amplitude depends on the energy of the electrons. At low energies, backward scattering is strong, which is the situation in the LEED. On the other hand, at high energies, the forward scattering is dominant, which is the situation for RHEED. This is why RHEED is configured at grazing angles and LEED is configured at normal angle with respect to the surface.

2.1.1 Low energy electron diffraction

This method is used to understand the arrangement of atoms at the surface. LEED uses the Bragg's diffraction law to investigate the surface structure. The wave length of the (elastically) scattered electrons is related to their kinetic energy,

$$\lambda \sim 0.1\sqrt{\frac{150}{E}} \tag{2.1}$$

where E is the beam energy in electron volts.

Electrons at a defined energy accelerate toward a single crystalline surface, then the back scattered electrons will be collected on a phosphorus screen. Diffraction spots

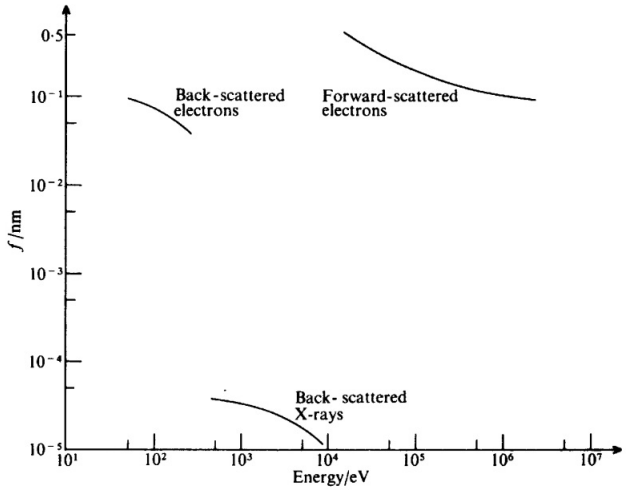

Figure 2.1: Approximate atomic scattering amplitudes for Aluminum as a function of energy of electrons and X-rays [2].

determine the surface structure in reciprocal space. It is very important that the electron path is field free, otherwise electrons might deviate from their original path. As shown in Fig.2.2, LEED has electric lenses that act just like optical lenses. They are used to focus the backscattered electrons on the screen and remove the electrons which have lost their energy through inelastic scattering. In order to remove all diffracted electrons that have lost energy through inelastic scattering events with the sample atoms, a retarding field with spherical symmetry is created by applying voltages slightly lower than the primary beam energy to the grids situated in front of the screen. The electrons that overcome this retarding field are accelerated toward the phosphorescent screen, where they produce bright spots whose intensity is proportional to the number of electrons in the corresponding beams.

Despite the surface sensitivity of LEED, the electrons used in LEED experiments penetrate a few atomic layers into the substrate, and therefore they can provide information on the subsurface structure. In practice, this is achieved by varying the primary beam energy (which, in turn, modifies the electron wavelength and their mean free path inside the solid) and measuring the changes in the diffracted beam intensity.

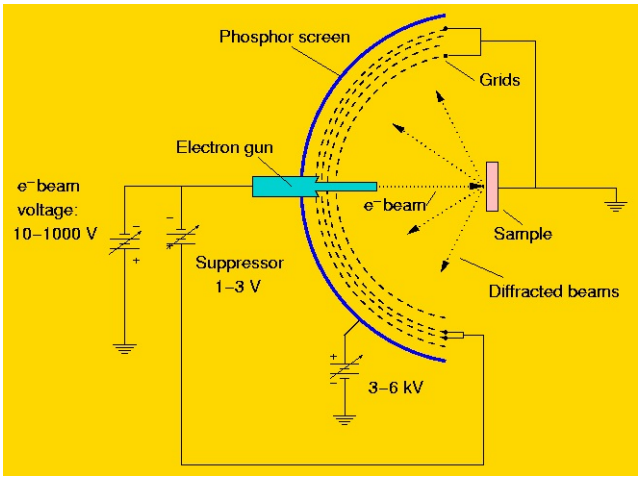

Figure 2.2: The schematic of LEED. Between first grid (from sample) and screen the electrons are radially accelerated so they have enough energy to excite fluorescence in the screen. The second and third grid are functioning as a filter for inelasticaly scattered electrons, these two grids are the suppressors. Another grid helps to reduce the effects of penetration of the high positive potential on the screen through the open mesh of the grids. The electron gun has its own optics to control the beam size and focus. There are four lenses which help positioning the electron beam. Also there is a Wehnelt voltage which is negative and focuses the beam. Wehnelt is a cylinder on top of filament with a small hole ($1\,mm$ to $100\,\mu m$ in diameter) on it that electrons pass through. Immediately after Wehnelt cylinder, there is an anode at high positive voltage that accelerates electrons through Wehnelt hole to the sample.

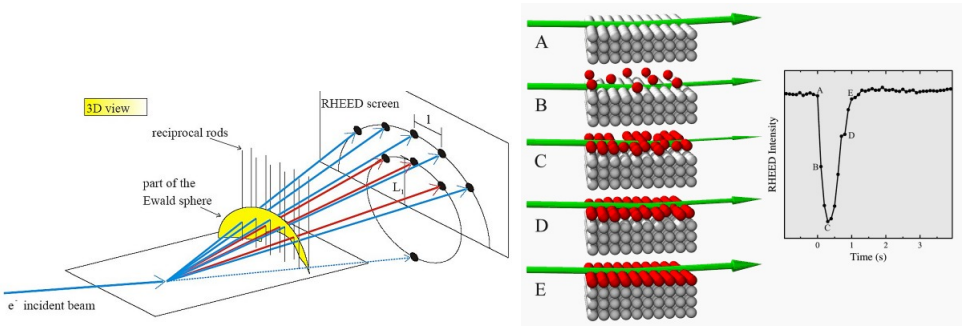

Figure 2.3: LEFT: The diagram above shows the basic set-up for a RHEED experiment, with the sample viewed edge-on. In practice the display screen is usually a phosphorus coating on the inside of a vacuum window (viewport) and the diffraction pattern can be viewed and recorded from the atmospheric side of the window. The small scattering angles involved are compensated for by using relatively large sample/screen distances. RIGHT: This figure shows surface models illustrating the growth of a single monolayer of film on a flat surface in layer by layer mode. The graph shows real measured RHEED intensity during homoepitaxial growth of a single unit cell layer of $SrTiO_3$.

2.1.2 Reflected High Energy Electron Diffraction

As mentioned, LEED utilizes the inherent surface sensitivity associated with low energy electrons in order to sample the surface structure. As the primary electron energy is increased not only does the surface specificity decrease but two other effects are particularly noticeable,

- forward scattering becomes much more important (as opposed to the backward scattering observed in LEED)
- the scattering angle (measured from the incident beam direction) tends towards 180 degrees for back-scattering and 0 degrees for forward scattering.

The surface sensitivity of RHEED is affected significantly by surface roughness. If small bumps stick out of surface, then the incident beam will pass through them. Therefore the beam will be diffracted by 3D atomic arrangement within the bumps. This feature can be used to monitor the surface morphology during material growth. For growth mode monitoring, we look at the intensity of the specular reflection. The intensity of the reflected beam is proportional to the surface roughness. Smooth surfaces give a high reflected intensity, rough surfaces don't reflect well and the intensity is lower. From RHEED oscillation it is possible to understand the growth mode. Fig.2.3 RIGHT, shows the RHEED oscillation as a layer is formed at the surface. Number of oscillations is a measure of number of layers which have been grown epitaxially. RHEED can help to better understand the growth mode as well. There are three growth mode,

- Layer growth, or Frank-van der Merwe: Layer-by-layer growth is possible in many lattice-matched oxide systems. In an ideal case a layer is completely filled before the next layer starts to grow. In reality the next layer gets nucleated before the previous layer is finished, resulting in a spread of the growth front over several

monolayers. Due to this RHEED intensity oscillates, but also drops in intensity. Layer-by-layer growth requires higher mobility of adatoms than island growth

- Island growth, or Volmer-Weber: Island growth can be useful for growing nanostructures on a surface but RHEED intensity monitoring is not particularly useful in this case. Most likely the RHEED pattern would show a regular array of transmission spots.

- Wetting layer and island growth, or Stranski-Krastanov: It is an intermediary process characterized by both 2D layer and 3D island growth. Transition from the layer-by-layer to island-based growth occurs at a critical layer thickness which is highly dependent on the chemical and physical properties, such as surface energies and lattice parameters, of the substrate and film.

2.2 Scanning Tunneling Microscopy

Scanning tunneling microscopy (STM) was invented by Binnig and Rohrer[1] in 1981 [3]. By integrating scanning capacity into vacuum tunneling capability, STM enables us to image the surfaces of conducting samples and study their local electronic properties down to atomic scales. The essential components of an STM include a sharp probing tip; a piezoelectric scanning unit, which controls the vertical and lateral movement of the tip; a coarse positioning unit, which brings the tip-sample separation to within the tunneling range ($\sim$ Å); a vibration isolation stage; and a set of electronics, which detects the small tunneling current ($\sim$ $10\,\mathrm{pA} - 1\,\mathrm{nA}$), controls the piezo-tube scanner with feedback, and drives the coarse positioning.

To initiate the tunneling process, the STM tip is brought to within several angstroms from the sample surface by the coarse approach walker. Applying a bias voltage between the sample and the tip electrode gives rise to a quantum mechanical tunneling

[1]Gerd Binning (1947) and Heinrich Rohrer (1933-2013). In 1986, they were awarded half of Nobel prize in physics "for their design of the scanning tunneling microscope".

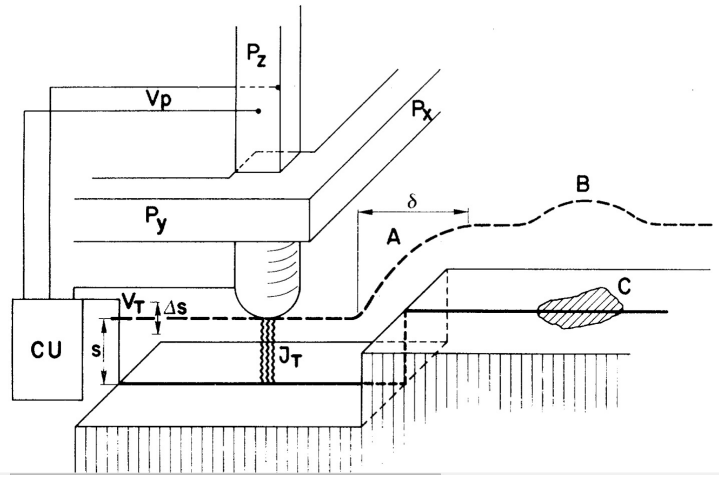

Figure 2.4: Principle of operation of the scanning tunneling microscope. The piezodrives move the tip over the surface. The control unit (CU) applies the appropriate voltage to P_z driver for constant tunneling current. Figure taken from the original paper of Binning and Rohrer [3].

current. Since the tunneling probability amplitude is an exponential function of the tip-sample separation, the value of the tunneling current is extremely sensitive to the sample surface corrugation. For instance, given a work function $\sim 1\,\mathrm{eV}$, a decrease in separation of $1\,\text{Å}$ increases the tunneling current by a factor of three. During topographical image scanning, by keeping the tunneling current constant with the feedback adjustment, the output voltages from the feedback loop to the z-electrode of the piezo tube are converted to deduce the vertical position of the tip as a function of its lateral position, $\mathrm{z(x, y)}$. This is called constant-current topographic imaging. Via constant-current imaging, we can identify the feature of interest and zoom in to investigate its local electronic structure, more specifically, its local density of states (LDOS), with the tunneling spectroscopy capability. Studying the differential conductance $\frac{dI}{dV}$ in a planar-junction-type of tunneling experiment, the averaged DOS of the sample is extracted. To obtain the spatially resolved LDOS, we measure the tunneling spectra point by point on target areas. During a set of scanning tunneling spectroscopy measurements, a constant tip-sample separation is first established by fixing the set-point current at a given bias

Figure 2.5: Left: Original publication on the discovery of x-rays by Rontgen. Right: One of the first diffraction patterns obtained by Laue.

voltage. Next, the feedback is turned off and a small sinusoidal modulation is added to the DC bias voltage. The resulting current modulation ($\propto \frac{dI}{dV}$) is then read off from a lock-in amplifier, into which the tunneling current signal from the current pre-amplifier is fed. We record the output signal from the lock-in amplifier as a function of the DC bias voltage to generate a tunneling spectrum $\frac{dI}{dV}(\mathbf{r}, V)$, and hence the LDOS. By taking $\frac{dI}{dV}$ along a line or by taking a two-dimensional $\frac{dI}{dV}$ map, changes in LDOS around a impurity, across a step-edge, or among grains with different crystalline orientations can be revealed and compared with theoretical predictions.

2.3 X-ray Diffraction

X-ray diffraction (XRD) is one of the most established experimental methods in physics. It is one of most crucial experimental tools in physics, biology, chemistry, geology and so many other major fields of science and technology. Any method that exploits X-rays is based upon their discovery in 1895 by W. C. Röntgen[1] by chance while studying the charge transport in gases. This achievement was rewarded the first Nobel

[1]Wilhelm Conrad Röntgen 1845-1923. Awarded the first physics Nobel prize "in recognition of the extraordinary services he has rendered by the discovery of the remarkable rays subsequently named after him".

prize in the field of physics, in 1901. The first diffraction experiment was performed by Max v. Laue in 1912[1]. Fig.2.5 displays the observed diffraction pattern. With this single photograph, Laue solved at once two major problems of his days: It clearly reveals the crystalline nature of solids and proves that x-rays behave like waves. This finding was rewarded the Nobel prize in 1914. In a similar effort, W. H. and W. L. Bragg[2] found that substances whose macroscopic forms were crystalline gave remarkably characteristic patterns of reflected X-ray, quite different from patterns produced by liquids. To explain the diffraction patterns, Bragg assumed two conditions

- The x-ray should be specularly reflected, meaning the angle of incidence and reflection are the same, by ions in any plane.
- Reflected waves from successive plane should interfere constructively.

The two conditions are summarized in Fig.2.6. The path difference between two reflected waves is 2d$sin\theta$. For constructive interference, the path difference should be an integer number of wavelengths. Eq.2.2 shows the Bragg's diffraction:

$$n\lambda = 2d\, sin\theta \tag{2.2}$$

where n is the order of the corresponding reflection, λ is the wavelength, θ is angle of incidence and d is lattice spacing that depends on Miller's indices which are related to crystallographic directions. For example for a simple cubic single crystal substrate in [001] direction, the plane spacing relates to Miller's indices by,

[1]Max Theodor Felix von Laue 1879-1960. Awarded Nobel prize "for his discovery of the diffraction of X-rays by crystals".

[2]Willian Henry Bragg (father, 1862-1942) and Wlilliam Lawrence Bragg (son, 1890-1971), awarded Noble prize in physics "For their services in the analysis of crystal structure by means of X-ray".

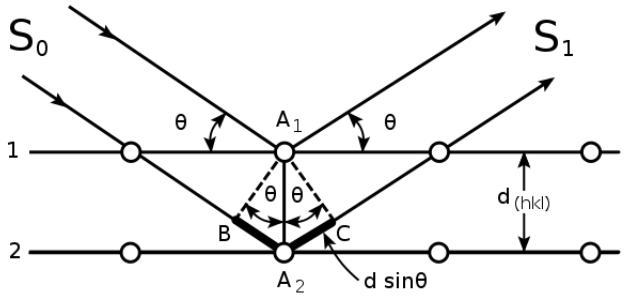

Figure 2.6: The x-rays are reflected from a family of planes, with d_{hkl}, the wave length and path difference $2d sin\theta$ determine the Bragg condition.

$$d_{hkl} = \frac{a}{\sqrt{h^2 + k^2 + l^2}} \tag{2.3}$$

where a is the lattice constant and h,k and l are the Miller indices. Having d_{hkl} defined as above, family of planes in $[00\,n]$ satisfy Bragg's condition.

Another way of treating of x-ray diffraction is done by von Laue. In this method there is not assumption of specular reflection. The crystal is composed of identical microscopic objects placed at Bravias lattice sites. Each object at lattice site reradiate the incident radiation in all directions. In this approach, the diffraction is treated as a scattering process, where incoming x-ray and outgoing x-ray have $\mathbf{k}$ and $\mathbf{k}'$ wave vector. The diffraction condition is met if $\mathbf{k} - \mathbf{k}'$ is a reciprocal lattice vector.

XRD is a valuble tool in determining the structural detail of epitaxial thin film. In this case a thin film is grown on a crystalline substrate with single direction. The epitaxial thin film follows the crystal direction in-plane lattice constant of the substrate. If the lattice constant of the thin film is different from that of substrate, then the thin film will be under stress and as a result will strain. If the lattice constant of the substrate is larger (smaller) than thin film, then the strain is tensile (comperessive). The strain is defined as,

$$\epsilon = \frac{a_{film} - a_{substrate}}{a_{substrate}} \tag{2.4}$$

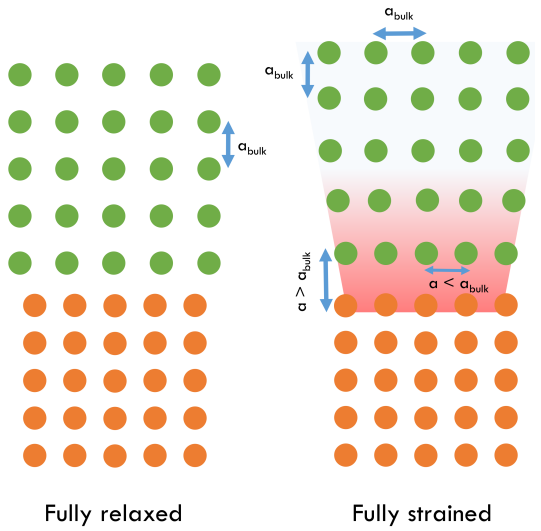

Figure 2.7: *Left*: Fully relaxed thin film. The thin film lattice constant is the same as bulk. *Right*: Fully strained. The strain from the substrate changes the lattice constant of thin film near the interface.

If the lattice mismatch between the substrate and thin film is large (small), then the thin film will (not) follow the in-plane lattice constant of the substrate. The thin film in this case is called *Fully relaxed* (*Fully strained*). Fig.2.7 *left* shows the fully relaxed thin film above the substrate. Fig.2.7 *right*, shows the effect of compressive strain on the thin film. The out of plane lattice constant is expanded while the in plane lattice constant for layers close to the substrate are similar to the lattice constant of substrate. The strain field vanished away from the substrate and the thin film retains its bulk structure. Using High-Resolution XRD (HRXRD), it is possible to measure the strain in the thin film and determine if the thin film is fully relaxed or fully strained.

Since usually the lattice constant of thin film and substrate are close, special experimental equipment has to be introduced in order to resolve the very closely spaced peaks that occur in the diffraction pattern of epilayersubstrate material systems. This is the reason for naming the field HRXRD. It often happens that observable peaks are as close as 0.001° apart and that the structural information to be derived deserves the precise measurement of this spacing. This cannot be obtained with the diffractometer

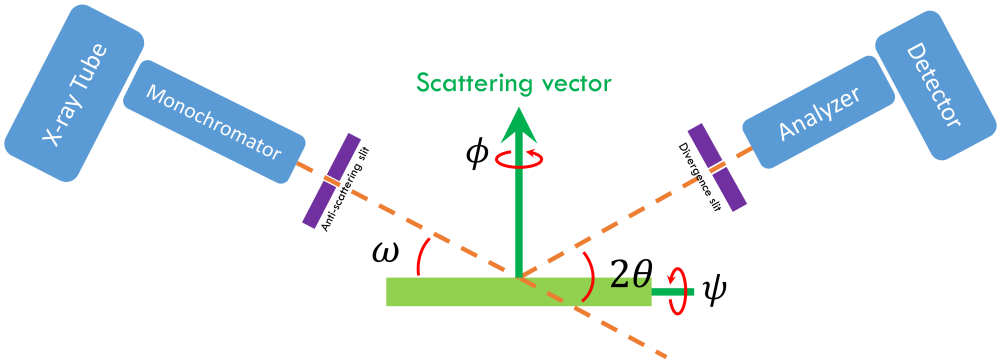

Figure 2.8: Schematic of HRXRD is shown. On the source side, the monochromator and anti-scattering slit, and on the detector side, the divergence slit and analyzer are shown.

settings presented so far for the investigation of polycrystalline material. The precision $^{\Delta d}/_{d}$ by which interplanar spacings may be determined is given by,

$$\frac{\Delta d}{d} = \frac{\Delta \lambda}{\lambda} + \frac{\delta}{tan\theta} \tag{2.5}$$

where $\Delta\lambda$ is the spectral width (FWHM of incoming x-ray photon), δ is the beam divergence. In order to arrive the required high resolution, using monochromatized x-ray and analyzer is necessary. The monochromator is consist of two parallel Ge (220) crystals and a mirror to focus the x-ray. On the detector side, an analyzer is very helpful to further reduce the beam divergence and remove diffused scattered x-rays. Careful alignment plays a critical role in obtaining fine details of thin film structure. Fig.2.8 shows the XRD set up for high resolution measurements. The incidence angle is $\omega = \theta$+offset and the reflection angle is 2θ. There are two types of measurements for thin films, symmetric (also called $\theta - 2\theta$) and asymmetric scans ($\omega - 2\theta$). In symmetric scan, the scattering vector is perpendicular to the surface of thin film, while in asymmetric scan the scattering vector has an offset from normal to the surface. Symmetric scan is used to measure the lattice constant, crystallinity and phase of the thin film while asymmetric scans are often used to measure mosaicity.

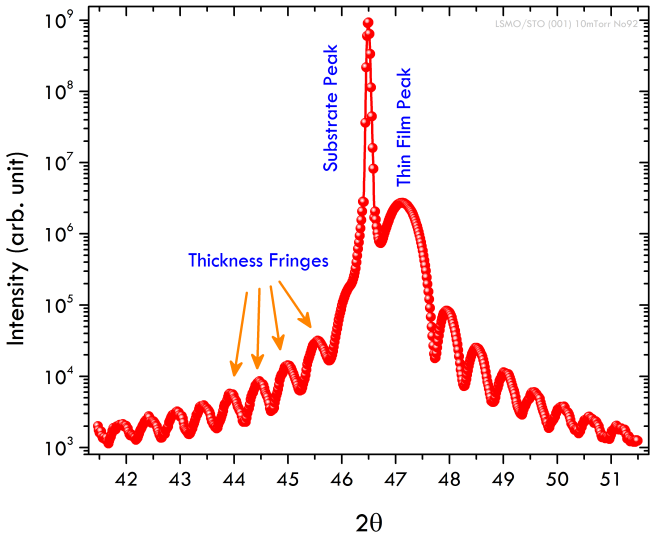

Figure 2.9: $\theta - 2\theta$ scan is shown. The substrate, thin film and thickness fringes peaks are showed.

Fig.2.9 shows an example of symmetric or $\theta - 2\theta$ scan. There are three types of peak in the spectra[1]. The peak with highest intensity is the substrate. The second intense peak belongs to the thin film and depending on the type of strain, tensile or compressive, the thin film peak can be on the right or the left of substrate peak, respectively. In Fig.2.9, the thin film peak is at higher angles, therefore the strain is tensile. The lattice constant is related to thin film position by Bragg's condition, $n\lambda = 2d\,sin\theta$. Third type of peaks are thickness fringes. The distance between thickness fringes $\Delta\theta_m$ which is due to interference of of rays coming from surface and interface, is related to the film thickness,

$$t = \frac{\lambda}{\Delta\theta_m} \frac{1}{2\,cos\theta_B} \tag{2.6}$$

where λ is wave length of incoming x-rays and θ_B is the Bragg peak position. The observation of the the fringing proves the high quality of thin film, since for the appearance of thickness fringes the thin film surface and interface should be very well-defined and also it shows the high crystallinity of the thin film.

[1]In XRD literature, sometimes they are called S (substrate), L (thin layer) and F (thickness fringes).

Figure 2.10: SPECS PHOIBOS 150 WAL energy analyzer.

2.4 Electron/Ion Energy Analyzer

The SPECS PHOIBOS hemispherical electrostatic energy analyzer is designed to measure the energy of electrons or ions (charged particles). It can measure the kinetic energy of admitted particle from $0\,eV$ to $3.5\,keV$.

Every hemispherical electron energy analyzer should have three major parts: electron admission lens system[1], hemisphere part[2], counting system[3]. We will go through all parts one by one.

It is notable and (somehow obvious!) that *every* energy analyzer should work under UHV (ultra high vacuum) because the electrons which are coming out of surface might collide with the gas molecules and lose energy and momentum.

2.4.1 The Lens System

The lens system has two main jobs, one is to focus the electrons (or image) onto the entrance slit[4], and the second is to retard the incoming electrons to pass energy of

[1]It will give angular or spatial resolution.

[2]Only electrons with a well-defined energy can go through it, hence counting is possible. Otherwise it is not possible to resolve the kinetic energy of electrons

[3]It can be a single channel or multi-channel detector, our energy analyzer (PHOIBOS 150) has a 9-channel detector.

[4]The focusing has different applications, for example, the spatial resolution, i.e. magnification, or angular resolution, or just maximizing the transmission the electrons, basically integrating on space and angles.

the analyzer. The idea is just like optical lenses. The goal is to gather some electrons from a spot on the sample (which is the object) and produce an image of that object. So here since the rays are electrons (or ions), then the lens should be electrostatic lens, since one should work with charged particles. The main difference between optical and electrostatic lens is that the quantity analogous to the refractive index, namely the particle velocity, varies continuously across an electrostatic lens, whereas a discontinuous change of refractive index occurs at the surface of an optical lens. The optics that lots of us may remember deals with thin lenses, while here, for charged-particle lenses, one is dealing with *thick lenses*, meaning that the axial dimension (thickness) of the lens is comparable with the focal points of the lens.

Fig.2.11 shows the principle of geometrical optics for lenses[1]. The same principles apply for electrostatic lenses.

In our analyzer, the sample, which is the object, is located at some distance from the opening of the analyzer[2], which is the pupil. Then the lenses will produce an image right at the entrance slit of hemisphere, finally that image will be characterize by detecting system.

2.4.2 Principles of electrostatic lenses

In this section, I will try to give a brief introduction on the electrostatic lenses. The main purpose this section is to understand the basics of this subject.

It is know that axially symmetric electrodes, which are electronically biased, can produce an electrical potential that can work as a lens, because it can change the

[1]According to Snell's law,the image pencil is determined by the object pencil angle. This relation is given to first order by the Helmholtz-Lagrange law:

$$x_1\theta_1\sqrt{E_1} = x_2\theta_2\sqrt{E_2} \qquad \sqrt{\frac{E_1}{E_2}} = Mm \qquad M = \frac{x_2}{x_1} \qquad m = \frac{\theta_2}{\theta_1} \tag{2.7}$$

where M and m are the linear and angular magnification, respectively. One important consequence of this law, which I mention without proof, is that *the ratio of brightness to energy is conserved from object to image.*

[2]According to manual, it should be around $40mm$.

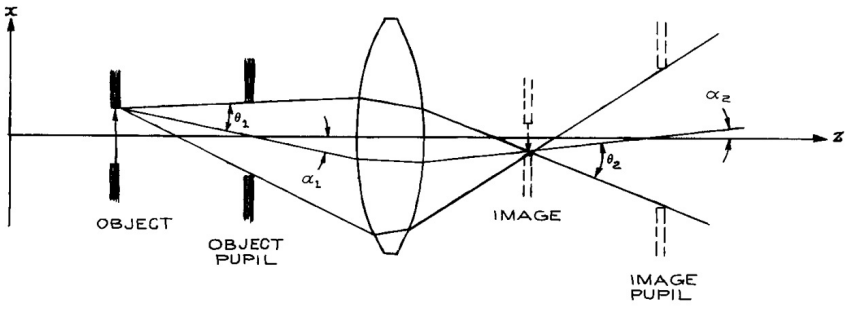

Figure 2.11: In this picture, the object is being defined by the window, *object pupil*. The rays emanating from the object are limited by the pupil (part of your eyes the lets the light in is called pupil too!). This pupil defines a cone of rays with angle θ_1 which is called *pencil angle*. α_1, the angle of incidence of the central ray from the object on the plane of the pupil is referred to as the *beam angle*. It is seen that once the rays passed the lens, they will have a new beam and pencil angle. For most application, the pencil and beam angles are small and the approximation $sin\theta = \theta$ is valid. Working in this regime is called *Gaussian* or *paraxial* optics.

electrons path, therefore it can produce a focal point for the electrons. The most widely used lens for focusing the charged particles is consist of two or more coaxial cylinders which can be biased. Just like what an optical lens does (changes the velocity of light), these cylinder lenses can change the velocity of the electron. Hence they accelerate of decelerate the electrons. Fig.2.13 shows two cylinder lenses that are hold at different potential(cross-sectional view). The potential change happens continuously in space, so the kinetic energy of the electron changes as it passes through the lenses, meaning that it can bring the electron from E_1 to E_2. The focal point of this lens[1] depends on the dimensions of the cylinder, the spacing between two cylinders (gap) and the ratio of initial and final kinetic energy. Since the gap is so important (because it can increase the edge effects dramatically) usually the gap is $g = 0.1D$, where D is diameter. To obtain the desired focal properties for a wide range of energies and acceleration ratio, two or more (ours has 10!) cylinder can be used in series(look at Fig.2.12). One advantage of

[1]By the way, it is clear that each lens should at least have two cylinders.

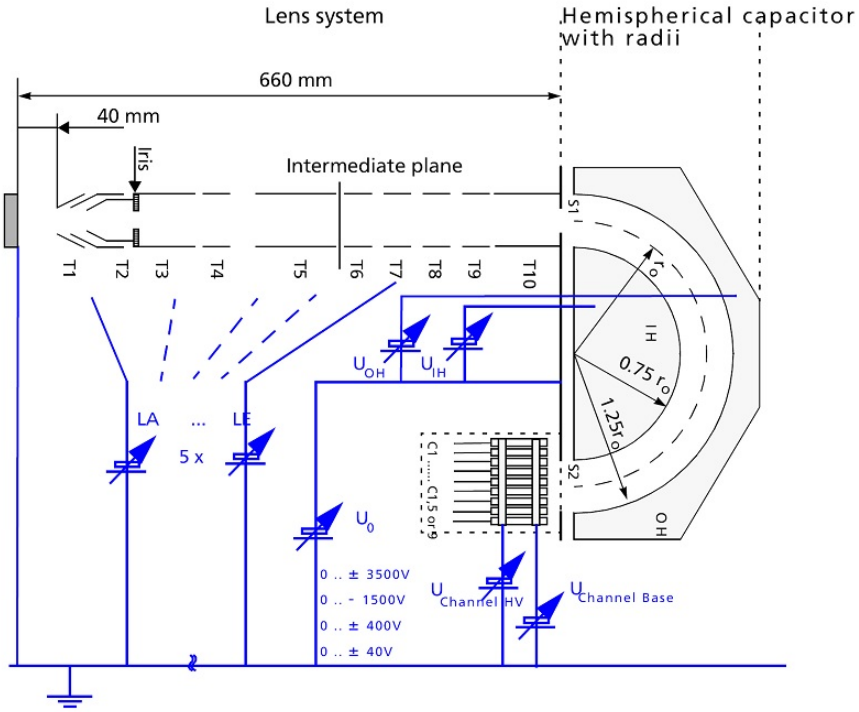

Figure 2.12: The lens system of our analyzer. The 10 lenses of the analyzer are seen. Notice the iris at the opening. It can help to reduce aberrations and get a better focus at the entrance slit. Depending on the lens mode, an intermediate image is produced around intermediate plane.

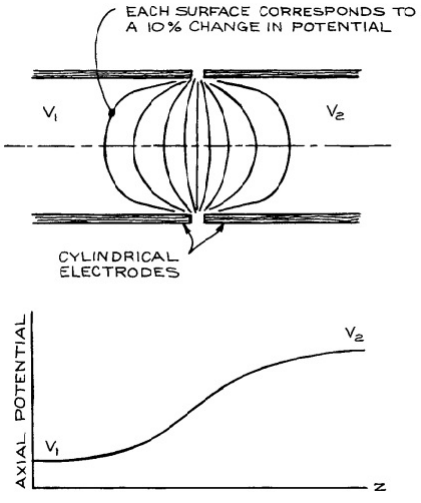

Figure 2.13: Two cylinder lens system, which constitutes one lens. The gradual change of potential, going from one cylinder to another will continuously change the electron's kinetic energy. The down plot shows the potential change as the electron travels through the cylinder.

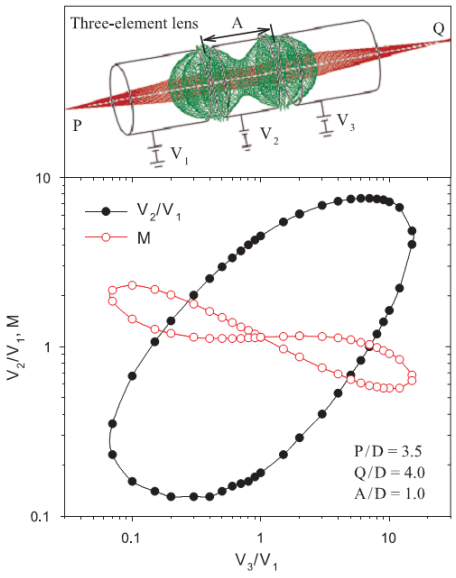

Figure 2.14: TOP: Three equi-diameter lens system. The width of the middle cylinder is equal to its diameter. The green lines shows the variation of electrical potential with position. BOTTOM: As the voltage ratios changes, the magnification changes too. P is object position, Q is the image position and D is the diameter. With fixed D,Q and P as the potential changes the image size changes. The decelerating mode corresponds to $\frac{V_2}{V_1} < 1$ while $\frac{V_2}{V_1} n > 1$ corresponds to accelerating mode (if $V_1 = V_3$).

multi-cylinder lenses (more than two) is that, since the gaps are small, the lens field overlap, so it is possible to treat the hole thing as a single lens. Fig.2.14 shows an example of three cylinder lens system. This lens system is able to produce image of a fixed object at a fixed image plane for a range of final-to-initial energy ratio, or it can produce a variable image location with a fixed energy[1]. The particle should be accelerated or decelerated to the pass energy, usually accelerating is preferred because decelerating will cause the expansion of beam in the middle region of lens, which can cause unnecessary interaction of beam with the wall of lens.

2.4.3 Aberration

An optical aberration is a departure of the performance of an optical system from the predictions of paraxial optics, i.e. image being out of focus or blurry. In an imaging system, it occurs when light from one point of an object does not converge into (or does not diverge from) a single point after transmission through the system. Aberrations occur because the simple paraxial theory is not a completely accurate model of the effect of an optical system on light, rather than due to flaws in the optical elements.

[1]This is called FAT or fixed analyzer energy. This fixed energy is the famous *pass energy*

Light source	VUV laser	The best synchrotron	Gas discharge lamp
Bulk sensitivity	30∼100 Å	5∼20 Å	5 Å
Energy resolution (meV)	0.26	5∼20	1.2
Momentum resolution	best		
Photon flux (/s)	2×10^{15}	$10^{12}10^{13}$	10^{12}
Spot size	∼0.2 mm	∼0.2 mm	1∼3 mm
Polarization	tunable	tunable	no or part
Photon energy (eV)	5∼7	tunable 5∼1000	21.2He I
Momentum region	about 1 BZ	many BZs	many BZs
Sample quality	high	rigorous	rigorous
Cost	high	very high	high

Figure 2.15: Comparison of different ARPES systems. Table taken from *Photoemission Spectroscopy on High Temperature Superconductor* by Springer.

Remember, there was an assumption that says $sin\theta = \theta$ which is NOT completely true. This assumption causes one class of aberration which is called *geometrical aberration*. *Chromatic aberration* caused by variations in the kinetic energy of transmitted particles. Electrons coming out of surface with different energies which make a non-coherent beam. *Space charge*[1] is due to repulsive interactions between the charged particles. The electrons repel each other because of Coulomb interaction, therefore it is not possible to merge, or focus all of them at the focal point.

For the systems that have cylindrical symmetry, the main type of geometrical aberration is *third-order focusing*, which is *spherical aberration*. If the sample is on or near the axis of lens then non-spherical types of aberration (like coma, field curvature, distortion and astigmatism) can be ignored. Therefore, it is important to minimize the spot size and locate the sample ON the AXIS of the lens system to minimize the geometrical aberration. Due to geometrical aberration, as shown in Fig.2.16, the pencil of

[1]This is the main problem of laser based ARPES systems. The pulse length of regular laser is very short and the number of photons in each pulse is high, so large number of photo-electrons will leave the sample at a very short time interval, which deteriorates the focus of electrons on the entrance slit. To overcome this problem, quasi-continuous wave violet laser is used. Also the newly discovered nonlinear optical crystal $KBe_2BO_3F_2$(KBBF) gives the ability to of frequency multiplication in ultraviolet waveband. The ultimate energy resolution using this system is 0.36 meV(PRL 94 057001). Fig.2.15 shows features of different ARPES systems.

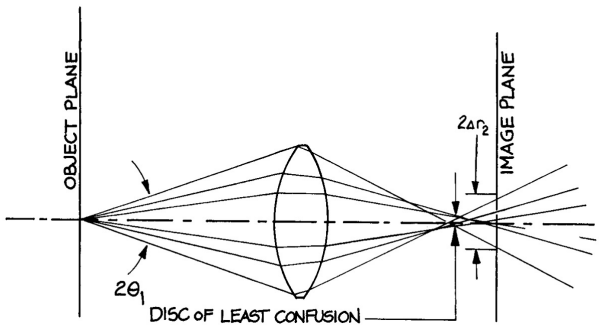

Figure 2.16: Geometrical aberration of the image of a point on the lens axis. There is no focal *point*.

rays emanating from an object point reaches a minimum diameter at a point slightly in front of the image plane. This minimum diameter is the *circle of least confusion*. To reach the sharpest focus, it is often possible to vary the lens voltage in order to place the circle of least confusion on the desired image plane.

2.4.4 Lens modes

In this section we will go through the mechanism of getting an image our analyzer. Our analyzer has 10 lenses(see Fig.2.12) which are placed in a way that they can produce the image twice, i.e. focus the electrons twice. There are several different modes that one can work with, like angular and spatially resolved.

Electrons which are coming from the sample (photoelectrons) will be admitted to the lens system at the opening of analyzer. The lens system will produce an image of the sample at the entrance slit of hemisphere. As the electrons pass through the lens system, they will produce an intermediate image and then they will be focused at the entrance slit of analyzer. At this point, electrons have been retarded to the pass energy. The amount of retardation is simply the difference between E_{kin} and E_{pass}.

2.4.5 Hemispherical Analyzer

There are thee methods to measure the energy of beam of charged particles.

- Measuring time of flight over a pre-defined distance. Since the velocity of particles

are high, and the distance is of order of centimeters, the time would be of order of nano-seconds. Therefore the electronics involved in this experiment should be very sensitive. *Time-of-flight analyzers* are used for electrons with kinetic energy less than 10 eV and for ions less then 1 keV.

- Measuring the applied retarding potential to decelerate and finally stop the particle. The technique requires a grid with appropriate potential, to retard the incoming particles. The Cons of this method is its compactness and low cost. But for high-resolution measurements it is not a good choice. The problem is, when the low energy particles approach the grid, the spacial variation electric potential can change the particle's energy, also only the normal component of kinetic energy is measurable.

- Measuring the deviation from the path in a known electric or magnetic field. This type of analyzers are called *dispersive analyzers*. For very high energy particles, deflection using magnetic field is preferred, because of high energy particles demand a very large electric field to deviate them. There are three types of dispersive analyzers:

  - Parallel plate analyzers
  - Cylindrical analyzers
  - Spherical analyzers

In this section, the main focus will be on the spherical analyzers. Comparing to parallel plate and cylindrical analyzers, the spherical analyzer has the advantage of requiring relatively low electrical potential on the electrodes. Also since the electrodes are closely spaced, the fringing fields are less of a problem and can be easily controlled. The main drawback of this class of analyzers is the difficulty of fabrication and mounting.

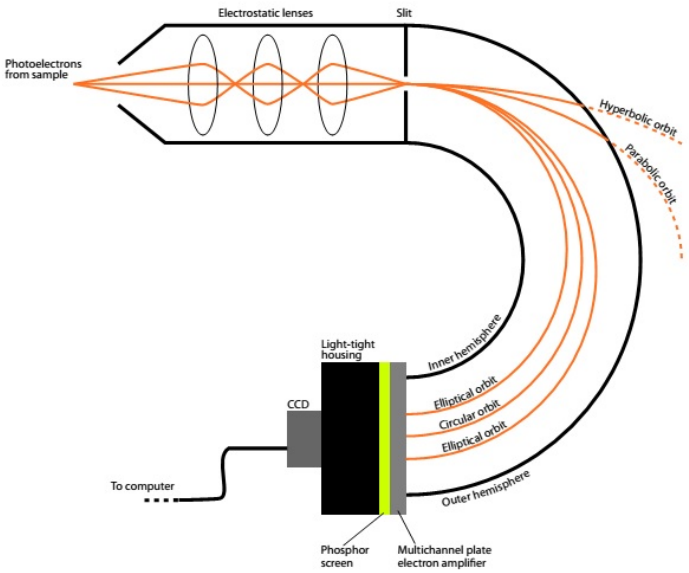

Figure 2.17: Schematic image of energy analyzer. It shows the main parts of an energy analyzer. The path of electrons with energies around pass energy is seen. Electrons with higher energy, will hit the outer hemisphere.

SPECS 150WAL analyzer has two concentric hemi-sphere with inner and outer radius of 112.5 and 187.5 millimeter. Hence the mean radius of analyzer is

$$R_0 = \frac{R_{in} + R_{out}}{2} = 150\,mm \tag{2.8}$$

The hemisphere has two slits: entrance and exit slit. These two slits are centered on the mean radius of analyzer R_0. For electrons to be detected, they have to travel their path through the slits and analyzer hemisphere. For an electron to make it through the hemisphere, it should has an appropriate energy, which is called pass energy. Suppose the at the entrance slit the electron does not have any energy, so for this particle to pass the hemisphere, it should follow the main potential line of analyzer, V_0, so its energy should be $-eV_0$. Thus particles with this amount of energy can pass through the hemisphere. Now, since there is some space between two hemispheres, there is a little range for passing energy. Particles with higher energy than pass energy will hit the outer hemisphere, while particles with lower energy will collide with the inner hemisphere(see Fig.2.17).

The resolution of energy analyzer is function of a lot of factors. The main factor which is tunable by user, is the pass energy. Theoretically it is possible to set the pass energy to zero. But in practice it is not possible! because the count rate decrease dramatically and the effect of stray fields becomes dominant. Very small pass energy means the electron has a negligible kinetic energy. This electron will be affected dramatically by the non-desired fields, like fringing field. SO the signal will be scrambled. Therefore it is necessary to optimize the pass energy for your experiment. Large pass energy might lead to production of artifacts, because a lot of electrons are being admitted. The resolution of analyzer, ΔE_{An} is related to pass energy, E_{pass}, mean slit size, S, mean radius of analyzer, R_0 and maximum angular deviation of incident particle in plane of dispersion, $\Delta\alpha$,

$$\frac{\Delta E_{An}}{E_{pass}} = \frac{S}{2R_0} + \frac{\Delta\alpha^2}{4} \tag{2.9}$$

There are other contribution to the line width of peaks in the spectra.

- The inherent line width of state, i.e. lifetime.
- The lifetime of the source, because the photon is coming from a state with a finite lifetime.

Therefore, the total broadening of a peak in the spectra, FWHM (Full Width at Half Maximum) is:

$$FWHM_{total} = \sqrt{\Delta E_{An}^2 + \Delta E_{level}^2 + \Delta E_{photon}^2} = \Delta E \quad \text{Final resolution} \tag{2.10}$$

It is useful to know that the best resolution that one can get from our source/analyzer set up is $FWHM_{extreme} = 0.44eV$. Also, according to SPECS, the natural line width of AlK_α and monochromatized AlK_α are $0.85eV$ and $0.3eV$, respectively. Therefore there is a hard limitation on the resolution that you can get from this setup which is the line

width of photon (source). In practice, SPECS people claim that FWHM of $0.6eV$ is good. Alignment has a massive impact on the line width. It is not hard to go below $0.6eV$.

It is important to note that if the potential on the two hemisphere is decreased by some amount δV, the pass energy will not change because pass energy is function of potential difference, not the absolute value of the potential on the hemispheres. It means that by altering the hemispheres potential simultaneously and equally, it is possible to scan all electrons with different kinetic energy, with the same value of pass energy[1].

2.4.6 Analyzer modes

The analyzer can work in two modes, that basically work based on this equation:

$$I \sim \frac{E_{pass}^2}{E_{kin}} \tag{2.11}$$

where I is the intensity. This relation says how the intensity changes as pass energy and kinetic energy change. Based on playing with these two variables, there can be different modes.

- Fixed retarding ratio, FRR.

  In FRR mode, as the name suggests, the ratio of pass energy and kinetic energy is kept fixed during data acquisition. So if $R = \frac{E_{pass}}{E_{kin}}$ is fixed, then you can relate the pass energy to kinetic energy, therefore the intensity depends directly E_{kin}. So as the kinetic energy goes up, the intensity increases too, but the pass energy increases as well which will adversely affects the resolution. So in this mode,

[1] If an electron exits from a grounded sample, all its energy is kinetic energy, changing the hemisphere potential can act as a retarding lens system, remember that the total energy of the electron is $KE+PE$, when the electron escapes from the sample, its potential energy is zero and all it has is kinetic energy, now if the hemisphere potential increase by δV, then the kinetic energy of admitted electrons will decrease by δV(conservation of energy $E_{pass} = eV_{slit} = KE + PE$ if $V_{slit} \Rightarrow V_{slit} + \delta V$ then $KE \Rightarrow KE - \delta V$). But the signal will NOT be angle resolved. Also, change in hemisphere potential can change the electron trajectory between the sample and entrance slit. The presence of lens system can keep the focusing properties of analyzer constant as the potential changes.

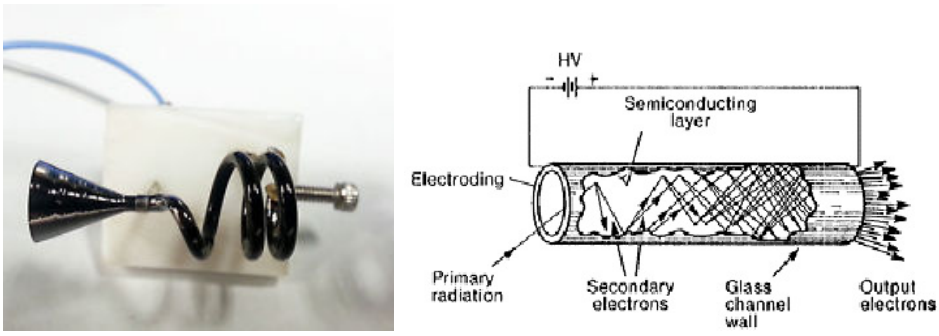

Figure 2.18: A continuous channeltron electron multiplier. Outside is glass and inside has a coated layer of SiO_2. It has a high gain, usually of order of 10^7 or higher.

the user defines the ratio R, and the analyzer changes pass and kinetic energy accordingly. It is important to note that for 2D mapping, the analyzer works in FRR mode, hence the window of energy is proportional to pass energy.

- Fixed analyzer transmission, FAT.

  In this mode, according to 2.9, the resolution and pass energy are fixed. Actually the resolution here is just the energy step. So having these two fixed, the intensity will be inversely proportional to E_{kin}. Thus in this mode all of the electrons will be admitted regardless of their kinetic energy. FAT is preferred for XPS and UPS measurements where the detailed spectra are required.

2.5 Electron detecting system

In the old days people used to use channeltron, which is a fancy name for electron multiplier, to detect or count electrons, measure their energy and find out the spectrum. Fig.2.18 shows a channeltron, the cone shaped part admits the electron, the spiral part multiplies the electrons. Because of the high gain[1] of this devices, they have to be very responsive to charging effect, i.e. the channeltron is connected to a positive high voltage (around 2kV) to supply electrons for the channeltron. We will not get into this class of electron multipliers, rather I prefer to discuss the our detecting system which is

[1]If one electron comes in the multiplier, how many more electrons will be gathered at anode, this is gain.

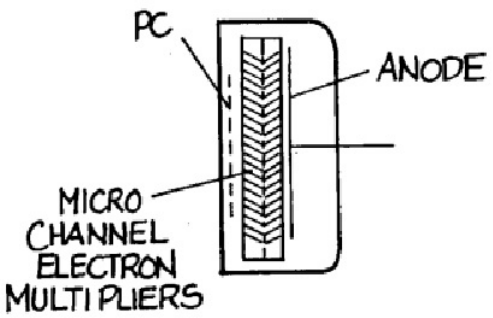

Figure 2.19: Schematic of MCP. PC is photo cathode, which in our system we do not have, because we are looking for electrons, not photons. The pattern of secondary electron multipliers is seen and on the right side the anode (electron collector) is placed.

micro-channel plate (MCP), although it used to be multichannel detector (MCD).

MCPs[1] are arrays of channel electron multipliers (CEM). Thus the fundamental of their working are the same, an electron comes, a cloud of electrons gets out. Instead of traditional dynodes (electron multiplier), electrons enter a bundle (can be a 2D array) of capillary tubes fused together in an array. Each tube has a resistive coating on its inner surface that acts as a continuous electron multiplier. Each capillary individually can be referred to as a channel electron multiplier (CEM). In these capillaries electrons make multiple reflections from the tube walls generating secondary electrons. MCPs have fast time response, good immunity from external magnetic fields, and position-sensitive capability when provided with multiple anodes. Fig.2.19 shows the schematic of an MCP.

The gain of MCPs is determined by length to diameter ratio. Usually the ratio for CEM is more than 50. An array of CEMs can make a MCP which can be of order 10 centimeter on side. For MCPs the ratio is smaller, therefore people may use to MCP in series that makes MCPs very compact and efficient. A particle striking the front of the plate triggers an electron avalanche in only one channel. The position of the charge cloud emitted at the output of a channel can be located with an accuracy

[1]For this section I am borrowing some of discussions of Moore in his book [17].

approaching the diameter of the channel. Both one-dimensional and two-dimensional position information can be extracted.

Our MCP is consisted of millions of very thin conductive glass capillaries, $10\mu m$ in diameter. Each of this CEMs can act independently which enables to resolve the position of impinging electron as well, hence producing a picture using a phosphor screen and CCD is possible.

Chapter 3
Photoemission Sepectroscopy

3.1 General Ideas of Photoemission Spectroscopy

The first signs of photo-emission spectroscopy emerged when Hertz observed in 1887, when he exposes ultraviolet light to his sample, there were some sparks across the gap. Those sparks were actually electrons were escaping from a metallic surface. Since it was prior to discovery of electron, nobody was able to explain this effect [18]. Later in 1905 Einstein explained this phenomena by introducing light quanta. He brought forward the hypothesis in which the energy of each quanta is $h\nu$ and the maximum kinetic energy of escaped electron is E_{kin}^{max}, i.e. the fundamental equation of photoelectric effect,

$$E_{kin}^{max} = h\nu - \Phi_0 \tag{3.1}$$

where Φ_0 is a characteristic constant of sample surface, i.e. the work function.

Today, a photoemission spectroscopy is being performed basically the same way as 100 years ago, only more accurate and more detailed. Photons came from a monochromatized light source, like soft X-ray, UV or synchrotron radiation[1]. As in Fig.3.1, electrons are directed on a sample and the ejected electron, i.e. photoelectrons, will move toward an analyzer which can resolve the energy and angle of emission of photoelectron. Knowing the kinetic energy of the electron, one can find the binding energy of the electron. So 3.1 takes the form of

$$E_{kin} = h\nu - \Phi - |E_B| \tag{3.2}$$

[1]The energy of incoming photon can bein the ultraviolet regime (5 to 100eV, UPS), in the soft X-ray regime (100 to 1000eV, SXPS) or in the X-ray regime (> 1000eV, XPS).

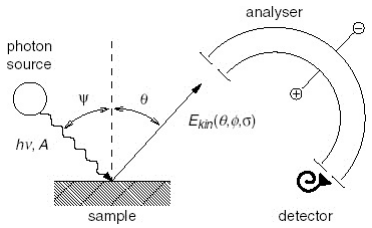

Figure 3.1: Schematic of photoemission spectroscopy apparatus. Monochromatic beam of photons with energy $h\nu$ will impinge on the sample and release the electrons (**A** is vector potential of electromagnetic (EM) field). The electrons will be directed to analyzer. The whole set up is at ultra high vaccum (UHV). The analyzer is consisted of two concentric hemisphere which are at different potentials in order to guide the electrons to the detector.

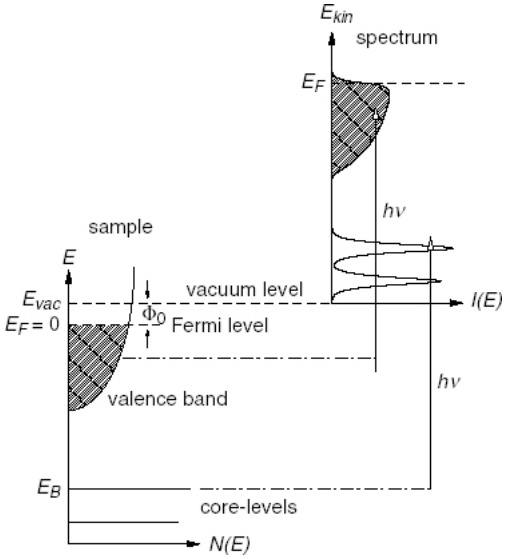

Figure 3.2: Relation between the energy levels in a solid and the energy distribution of ejected electrons. The energy reference level is Fermi energy. Valence electron contribute to near Fermi energy side of spectrum while core level electron will make sharp peaks relatively far from Fermi energy. The energy distribution of electrons is a resemblance of density of states (amount of states per energy) of a solid. Figure taken from [4].

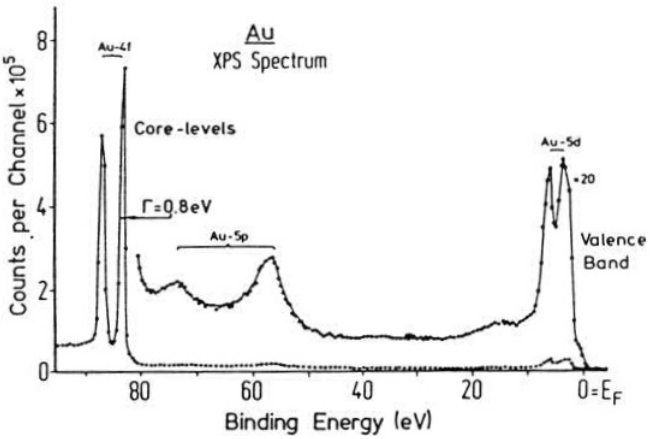

Figure 3.3: The XPS spectra of polycrystalline Gold. The Fermi edge of spectra is shown. The photon energies are 1487 eV which comes from AlK_α source. The famous spin-orbit splitting of $5d_{\frac{5}{2}}$ and $5d_{\frac{3}{2}}$ is seen. Usually the gold sample is used as a reference for calibration and finding Fermi energy different materials. Figure taken from [4].

where E_B is the binding energy of ejected electron. The ejected electron has a simple Hamiltonian which relates its momentum p to its kinetic energy,

$$\begin{aligned} E_{kin} &= \frac{p^2}{2m} \\ p &= \sqrt{2mE_{kin}} \end{aligned} \tag{3.3}$$

The direction of momentum is accessible using ϕ and θ which are azimuthal and polar angles of the ejected electron when it leaves the surface. Figure 3.2 shows the energy diagram of valence and core electrons. Valence electrons will have higher kinetic energy (according to 3.2) while core electrons are highly bounded to the material and will have a lower kinetic energy.

X-ray photoemission spectroscopy (XPS) provides an asset to probe some of electronic properties of materials. Figure 3.3 shows the XPS of polycrystalline gold using photons with energy of 1487 eV. This energy comes from core transition of Aluminum, which is commonly called AlK_α. Al determines the material, K introduces the shell in

which the electron excited (K,L,M,N,...) and α indicates the level in the relevant shell. The gold sample presented here, was prepared by evaporating gold and depositing it on a substrate. The commercially available samples are usually Au[111] which are grown on Mica. The main purpose of XPS is to probe core level characteristic. In order to probe the valence electrons, especially near Fermi energy, another source with a better resolution is needed. The resolution of X-ray sources are of order of a tenth of electron volt. The resolution is bounded by full width at half maximum (FHWM) of photons.

Regarding to the position of Fermi edge, it is highly recommended to use sources with low energy. Ultra violet source (UV) is a very reliable option. The advantage of working with low energy photons is that they a negligible momentum. The momentum of UV photons are thousand times less than crystal momentum. Therefore it is possible to resolve the momentum of electrons as well. Figure 3.4 shows the spectra of copper [110] at normal emission using UV source. The photon energy is related to He Iα which is 21.2 eV. In the first 2 eV of binding energy, the flat 4s state is visible and after that a sharp peak shows 3d state. After 6 eV the secondary electons[1] are presented. The secondary electron background suddenly drops at $E_{kin} = 0$ which means there is no photon with sufficient energy to eject any more electron. This cutoff energy with respect to Fermi energy can be used to measure the work function of sample, hence the width of the spectral distribution is given by $h\nu - \Phi$.

3.2 The electron mean free path

The mean free path of electron is the distance that electron can travel without energy lost, i.e. no inelastic collision. One of the main concern about photoemission spectroscopy (PES) is ultra high vacuum (UHV) condition. Figure 3.5 shows the mean free path of electron as a function of kinetic energy. According to this figure, the minimum mean free path occurs at $E_{kin} = 50eV$, which is about 3**Å** whihc is very small. This small value suggests that with this kinetic energy, only electrons near the

[1]Electrons which undergo an inelastic process and they lose energy.

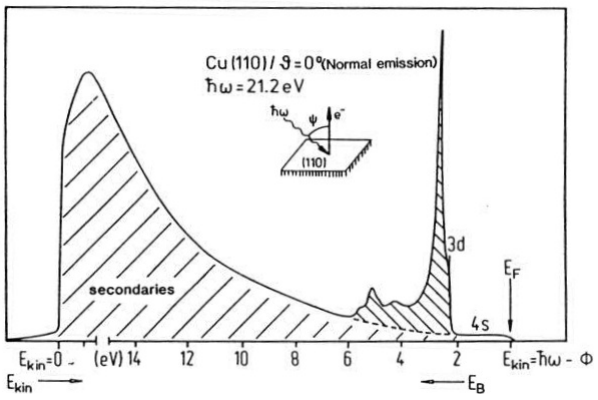

Figure 3.4: The UPS spectra of copper.Figure taken from [4].

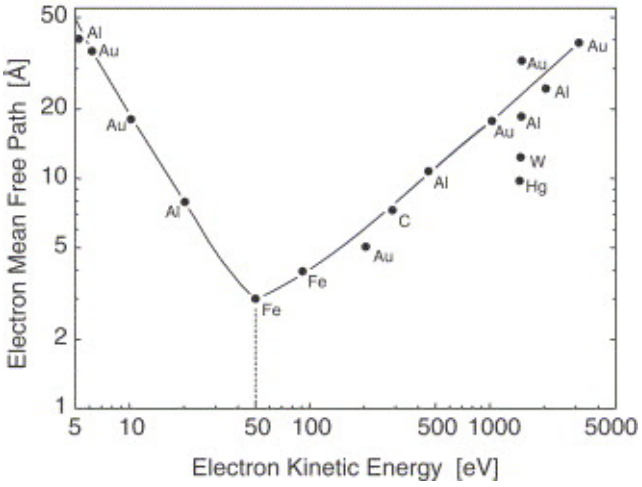

Figure 3.5: Electron mean free path a a function of kinetic energy for various metals. In UPS the mean free path is a few angstrom while in XPS it is significantly larger.

surface can escape, so basically one probes the surface of solid. As kinetic energy goes higher or lower, mean free path increases. In a typical UPS, the photon energy is of order of $20eV$ (for helium discharge source $h\nu = 21.2$) which corresponds to the mean free path of several angstrom. Therefore the surface should be extremely clean, hence UHV is of great importance. In a typical XPS, $h\nu = 1487eV$ which can penetrate to the depth of $30\mathbf{\AA}$.

Having such a surface sensitive spectra requires a very good vacuum. Let us quantify these considerations. With sticking coefficient of 1, which says every molecule or atom that hits the surface, will stick to it. Thus with vacuum of $2.5 \times 10^{-6} torr$, after *one*

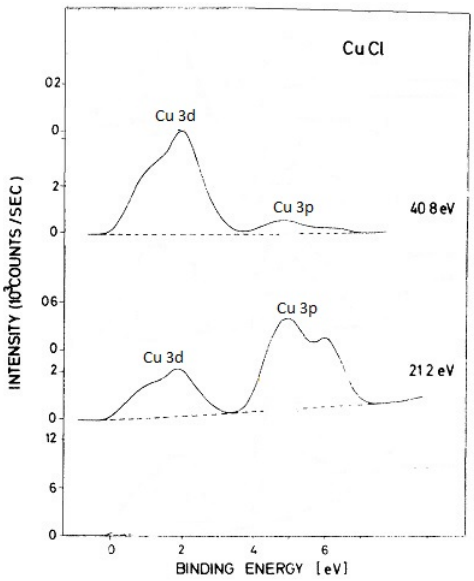

Figure 3.6: Comparison of PES of solid CuCl taken with He I (21.2eV) and He II (40.8eV) radiation. the intensity of the higher momentum (less extended) electrons increases with increasing photon energy relative to the lower momentum (more extended) 3p orbitals. Figure taken from [5].

second to obtain a coverage of one monolayer on the surface. So if the vacuum is $10^{-9}torr$, it will take about 1000 seconds, i.e. less than an hour! The sticking coefficient equal to 1 is quiet normal for highly active materials like alkali metals. Therefore, in order to acquire a good spectra, vacuum of $10^{-10}torr$ is obligatory.

Another interesting feature of PES is that the photon energy and the intensity of final state on energy dispersion curve are related. In other word, this feature is due to dependence of transition matrix element on the photon energy. Increasing photon energy, states with high angular momentum, like d orbitals, tend to show a greater intensity comparing with states with lower angular momentum, like p orbitals(Figure 3.6). This is a very useful property and can be employed to analyze complicated spectra.

3.3 The theory of photoemission

In PES, there are a lot photons which are coming onto surface to interact with electrons in solid. So basically we are looking at the interaction of electrons with electromagnetic field. Since there are enormous number of electrons in a solid, the problem

is a many-body problem which is very complicated. In this case, people usually make some approximations to simplify the perplex problem and solve it. At the heart of almost all theories of PES, there is an approximation which is called *sudden approximation*. It assumes that the response of system to the creation of a photohole is instantaneous and there is no interaction between escaping electron and the rest of system. Basically, escaping electron, on the way out, does not see other electrons, also other electrons do not realize that one electron is missing! because the hole is filled at no time. The consequence of this approximation is that the initial and final state are the same. This approximation works best for high energy PES.

3.3.1 Core level PES

The photocurrent produced in PES will bring the system from initial configuration i with wave function Ψ_i to final configuration f with wave functin Ψ_f by EM field with vector potential $\mathbf{A}$[1]. Assuming that the EM wave (photons) are causing a small perturbation Δ to the system, the transition probability ω per unit time between many-electron state Ψ_i an Ψ_f is given by Fermi's Golden Rule,

$$\omega \propto \frac{2\pi}{\hbar} \mid \langle \Psi_f \mid \Delta \mid \Psi_i \rangle \mid^2 \delta \left(E_f - E_i - \hbar\omega \right) \tag{3.4}$$

In the most general form the perturbation has the form of,

$$\Delta = \frac{e}{2mc}(\mathbf{A}\cdot\mathbf{p} + \mathbf{p}\cdot\mathbf{A}) - e\phi + \frac{e^2}{2mc^2}(\mathbf{A}\cdot\mathbf{A}) \tag{3.5}$$

where $\mathbf{A}$ and ϕ are vector and scalar potentials and $\mathbf{p}$ the momentum operator, $\mathbf{p} = i\hbar\nabla$, ($\phi$ is not the work function). The commutation relation between $\mathbf{A}$ and $\mathbf{p}$ yields, $\mathbf{A}\cdot\mathbf{p} + \mathbf{p}\cdot\mathbf{A} = 2\mathbf{A}\cdot\mathbf{p} + i\hbar\nabla\cdot\mathbf{A}$. Coulomb gauge makes $\phi = 0$, also neglecting two

[1]Remember for EM wave in Coulomb gauge the electric potential is zero (no charge source) and one can write down Maxwell equation just by vector potential.

photon process[1], $\mathbf{A}\cdot\mathbf{A}$ which implies that the spacial variation of vector potential is negligible, thus $\nabla\cdot\mathbf{A}=0$. If the EM wave length is large, it is legitimate to assume vector potential is constant over lattice. Therefore the only remaining term is

$$\Delta=\frac{e}{mc}\mathbf{A}\cdot\mathbf{p} \tag{3.6}$$

Having in mind that the commutation relation[2] for conjugate coordinate of $\mathbf{p}$, i.e. $\mathbf{r}$, and $\mathbf{H}$ is,

$$[\mathbf{r},\mathbf{H}]=i\hbar\nabla\mathbf{H}=i\hbar\frac{\mathbf{p}}{m} \tag{3.7}$$

where $\mathbf{H}=\frac{\mathbf{p}^2}{2m}+V(\mathbf{r})$, so the transition rate is proportional to,

$$\langle\Psi_f\mid\mathbf{A}\cdot\mathbf{p}\mid\Psi_i\rangle\propto\langle\Psi_f\mid\mathbf{A}\cdot\nabla V(\mathbf{r})\mid\Psi_i\rangle\propto\langle\Psi_f\mid\mathbf{A}\cdot\mathbf{r}\mid\Psi_i\rangle \tag{3.8}$$

the first outcome of Eq.3.7 is, if $V(\mathbf{r})=0$, i.e. free electron gas, there is no photoemission[3].

Now that the perturbative Hamiltonian is ready, in order to find the transition probability, one has to determine the wave functions. The simplest approximation is to assume that the excited (then escaped) electron is independent of other electrons. So the total wave function of system will be the product of the single electron orbital (the one which wants to escape) and the rest of electrons,

$$\begin{aligned}\Psi_i(N)&=C\phi_{i,k}\Psi^k_{i,R}(N-1)\qquad\text{(R stands for remaining)}\\ \Psi_f(N)&=C\phi_{f,E_{kin}}\Psi^k_{f,R}(N-1)\end{aligned} \tag{3.9}$$

where C antisymmetrizes the wave function, $\phi_{i,k}$ is the initial single electron orbital with

[1]If the EM wave length is much larger than reciprocal lattice vector, $\mathbf{A}\cdot\mathbf{A}$ is small. For $\hbar\omega=10eV$, $\lambda=10^3\mathring{A}$.

[2]Remember Ψ_i and Ψ_f are eigenstates of unperturbed Hamiltonian, i.e. $\mathbf{H}$.

[3]Conservation of linear momentum prohibits absorption of a photon by a free, unbound electron.

wave vector k, $\Psi^k_{i,R}(N-1)$ is the wave function of whole system where one electron with wave vector k is missing, $\phi_{f,E_{kin}}$ is the final wave function of escaped electron, $\Psi^k_{f,R}(N-1)$ is the final state of system which misses one electron with wave vector k. Therefore the transition matrix elements are proportional to,

$$\langle \Psi_f \mid \mathbf{r} \mid \Psi_i \rangle = \langle \phi_{f,E_{kin}} \mid \mathbf{r} \mid \phi_{i,k} \rangle \left\langle \Psi^k_{f,R}(N-1) \mid \Psi^k_{i,R}(N-1) \right\rangle \tag{3.10}$$

it is clear that the matrix elements are products of one electron orbitals by $(N-1)$ overlap integrals. The first step is to calculate the overlap integral. One can assume the rest of system stays intact after excitation , i.e. initial and final state of other orbitals (passive orbitals) are the same, which is called *frozen-orbital approximation*. In this case overlap integral is one(inner product of two identical state is one!). Now, having all these assumption, one may attain the PES of Hartree-Fock system. Therefore, binding energy is the same as negative of Hartree-Fock orbital energy of orbital k[1],

$$E_{B,k} \simeq -\varepsilon_k \tag{3.11}$$

The main problem of these assumptions (*frozen orbitals* and *sudden approximation*) is that the relaxation (response of system) is completely ignored! It means that the system that has been left behind is not at its ground state. In reality, system will relax and will response to charge perturbation through dielectric function (density-density response function).

Now lets assume that the initial and final states are *not* the same, i.e. the final state is a combination all available states. So the $N-1$ system has s excited state (final state is a combination of s initial state). Keep in mind that these states are eigenstates of unperturbed Hamiltonian. Therefore the Eq.3.10 becomes,

[1]This is sometimes called Koopman's binding energy.

$$\langle \Psi_f \mid \mathbf{r} \mid \Psi_i \rangle = \langle \phi_{f,E_{kin}} \mid \mathbf{r} \mid \phi_{i,k} \rangle \sum_s c_s$$
$$\text{where} \qquad c_s = \left\langle \Psi^k_{f,R}(N-1) \mid \Psi^k_{i,R}(N-1) \right\rangle \tag{3.12}$$

Now the problem is not completely one-particle problem in a sense that the ejected electron will see other electrons on the way out. The $|c_s|^2$ is the probability of removal of an electron from orbital ϕ_k of N-electron ground state, which then brings the system to a excited state which is combination of s N-1 electron system. For a highly correlated system, many of c_s are non-zero. This rather simple picture has a real nice physical interpretation. The result of having a mixed final state is that in the PES for $s = k$ one has the so-called *main line* and the other non-zero c_s are additional *satellite lines*. On the other hand, if the correlation is weak $|c_s|^2 \simeq 1$ for $s = k$ and for $s \neq k$, $|c_s|^2 \simeq 0$, meaning there is only one delta-like peak.

Eq.3.4 gives the transition probability of one electron, the photocurrent will the summation on all final, initial and single-electron orbitals of system, i.e.,

$$\begin{aligned} I \propto & \sum_{f,i,k} |\langle \phi_{f,E_{kin}} | \mathbf{r} | \phi_{i,k} \rangle|^2 \sum_s |c_s|^2 \\ & \times \delta \left(E_{f,kin} + E_s(N-1) - E_0(N) - \hbar\omega \right) \end{aligned} \tag{3.13}$$

where $E_0(N)$ is the ground state of N-electron system. Eq.3.13 says that the photocurrent consists of s delta-functions which are signatures of different k orbitals. Eq.3.13 shows that the excited electron on the way out will excite several (s) N-1 states which all are degenerate, for one specific k, (because delta function should be non-zero). So if the photon excites an electron from orbital k, depending on $E_{f,kin}$, different kinds of satellite lines can be produced, if the electron excite s N-1 electron state.

We can introduce a useful quantity, A which is called spectral function,

$$A = \sum_s |c_s|^2 \tag{3.14}$$

it should not be confused with vector potential.

For core-level PES, the formulation is slightly different, because they have itinerant electrons in valence band which can lead to almost infinite degrees of freedom for the final state of N-1 electron system. Remembering that c_s was an overlap integral, we can rewrite it as,

$$A(E) = \sum_c |\langle i \mid f_s \rangle| \tag{3.15}$$

The itinerant picture suggests that we have to consider the time evolution of outer electron due to its interaction with the core hole,

$$|f(t)\rangle = exp(-(\frac{i}{\hbar})(H - E_0)t)|i\rangle \qquad \text{this is in interaction picture} \tag{3.16}$$

where $H = H_0 + H_{int}$ is the final state Hamiltonian with $H_0 \mid i\rangle$ and $H \mid f\rangle = E_f \mid f\rangle$. From this, the dynamical response of the outer electron system (valence electrons) to the core hole is obtained as $g(t) = \langle i \mid f(t)\rangle$. Therefore the Spectral function is calculated by Fourier transform of $g(t)$,

$$A(E) = \frac{1}{\pi}\mathbf{Re}\int_0^{+\infty} dt \quad exp\left[i\left(\frac{E - E_B}{\hbar}\right)t\right] g(t) \tag{3.17}$$

where E_B is the binding energy of core electron and the many body effects are summarized in $g(t)$, the dynamical response of valence electron system to the core hole. If the

interaction is zero, than $\mid f(t)\rangle = \mid i\rangle$ which $g(t) = 1$ and the spectral function will be,

$$A(E) = \frac{1}{\pi}\delta(E - E_B) \tag{3.18}$$

that recovers our previous results for *frozen orbital* and *sudden approximation*. In simple word, spectral function determine how many states (N-1 electron states) are excited as the electron travels through the material to the surface, or in another words, how strongly the escaping electron interacts with the system.

3.3.2 Valence-state PES

In the previous section we assumed that core level states are k-independent (localized), while for valence electrons this is not the case. The valence electrons are itinerant, so they are k-dependent (delocalized).

The photocurrent for valence electrons is similar to Eq.5.9, but we have to keep in mind that now the matrix elements are k-dependent, i.e. like Bloch functions are periodic with respect to $\mathbf{G}$, reciprocal lattice vector.

$$\begin{aligned} I \propto |\widetilde{M}^1_{i,f}|^2 \delta(\mathbf{k}_{i\parallel} - \mathbf{k}_{f\parallel} + \mathbf{G}_\parallel)\delta(\mathbf{k}_i - \mathbf{k}_f + \mathbf{G}) \\ \times \delta(E_f - E_i - \hbar\omega)\delta(E - E_f + \phi) \end{aligned} \tag{3.19}$$

This one looks tedious!!! lets break it part by part. The first part represents the transition matrix elements which are taken between Bloch states[1]. Due to Fresnel equations[2], the parallel component of momentum is conserved. There two delta function

[1]When the matrix element is written as $\widetilde{M}^1$, it means that the momentum conservation has been written out explicitly and it has been taken between Bloch states. But when it is written as M^1 it means that the matrix elements contain the momentum conservation. Also if the matrix element is written as $\widetilde{M}$ or M, it is taken between an initial Bloch state and a final inverse LEED state.

[2]In case you forgot: Frensel equations says that when an EM wave travels from medium 1 to medium 2 (they have different index of refraction) the in-plane component of wave is conserved. Here since the photon carries small amount of momentum (in case of UV) then $\hbar k + p^e_i = p^e_f \Rightarrow p^e_i \simeq p^e_f$, also remember that the in-plane coordinate is periodic while the perpendicular component is not! the

for momentum to emphasize that the parallel component of momentum is conserved. It is known that the total (parallel and perpendicular) momentum is conserved, but also the parallel component is conserved too. The third delta function ensures the conservation of energy while the last delta function shows that only electrons with energy above the work function can be detected[1].

The photoexcited electrons have a short mean free path[2] inside crystal, therefore they are losing momentum, but the parallel component of momentum is conserved so they are losing the perpendicular part of their momentum. So lets introduce the complex perpendicular component of momentum as:

$$k_\perp = k_\perp^{(1)} + \mathtt{i} k_\perp^{(2)} \tag{3.20}$$

Writing $\mathbf{k}$ like this means that if $k_\perp^{(2)}$ goes to infinity, the perpendicular component of momentum will no longer conserve or basically all of perpendicular momentum will be lost which will smear the conservation of momentum equation,

$$\begin{aligned} I \propto \frac{|\widetilde{M}_{i,f}^1|^2}{\left(k_{i\perp}^{(1)} - k_{f\perp}^{(1)}\right)^2 + \left(k_{f\perp}^{(2)}\right)^2} \delta(\mathbf{k}_{i\parallel} - \mathbf{k}_{f\parallel} + \mathbf{G}_\parallel)\delta(\mathbf{k}_i - \mathbf{k}_f + \mathbf{G}) \\ \times \delta(E_f - E_i - \hbar\omega)\delta(E - E_f + \phi) \end{aligned} \tag{3.21}$$

The above equation means that the out coming electron, on the way out, interacts with other electrons in the solid. It means that the final state will be a hole (belongs to photoexcited electron) and series of electronic excitation that stem from electron-electron interaction. So one hole and N-1 electrons of system constitute the final state (the photo

lattice has a sudden termination at the surface. So the conservation of perpendicular component does not depend *only* on the electron, but also on the whole system!

[1]Actually here E is the measured kinetic energy of the electron which is $\hbar\omega + E_i - \phi$. Here the energy reference is at zero

[2]The mean free path is a function of kinetic energy of photoexcited electron, so for low energies, like laser ARPES, it is quite large and by large I mean you can probe the bulk properties.

excited electron will be out of solid!). The N-1 electrons can arrange themselves in many ways with the same energy, therefore the system will be highly degenerate. In order to include electron-electron interaction, in analogy with what is been done in Eq.3.13,

$$\begin{aligned} I \propto & \frac{\left|\left\langle \tilde{\phi}_{f,E_{kin}}|\mathbf{r}|\tilde{\phi}_i\right\rangle\right|^2 \left|\left\langle \tilde{\Psi}_{f,s}(N-1)|\tilde{\Psi}_i(N-1)\right\rangle\right|^2}{\left(k_{i\perp}^{(1)}-k_{f\perp}^{(1)}\right)^2+\left(k_{f\perp}^{(2)}\right)^2} \\ & \times \delta(\mathbf{k}_{i\parallel}-\mathbf{k}_{f\parallel}+\mathbf{G}_{\parallel})\delta(\mathbf{k}_i-\mathbf{k}_f+\mathbf{G}) \\ & \times \delta\left(E_{kin}+E_s(N-1)-E_0(N)-\hbar\omega\right)\delta(E-E_f+\phi) \end{aligned} \tag{3.22}$$

The wave functions with tilde mean that the conservation of energy has been satisfied explicitly.

The term $\left|\left\langle \tilde{\Psi}_{f,s}(N-1)|\tilde{\Psi}_i(N-1)\right\rangle\right|^2$ is to see how the final state in the solid (without the outgoing electron) is different from an initial state (again without that outgoing electron), so if there is no electron-electron interaction it is simply just unity. In a system with electron-electron interaction the final state is not an eigenstate of the Hamiltonian, usually it is a combination of a lot of many-body excited states, therefor each of those excited states will have finite overlap with the initial N-1 electron system. So the total overlap is,

$$A(\mathbf{k},E)=\sum_s \left|\left\langle \tilde{\Psi}_{f,s}(N-1)|\tilde{\Psi}_i(N-1)\right\rangle\right| \tag{3.23}$$

Here $A(\mathbf{k},E)$ is the spectral function of an electron with energy E and momentum $\mathbf{k}$. This function describes the probability of removing an electron from a system in its ground state. Spectral function determines that how the electron depends to the other electrons in the system, is it correlated or not. In second quantization language, it can be written as,

$$A(\mathbf{k},E)=\sum_s |\langle N-1,s|c_{\mathbf{k}}|N\rangle|^2 \tag{3.24}$$

where $c_{\mathbf{k}}$ is the electron annihilation operator. The spectral function is related to a

fundamental property of an N-electron system, one particle Green's function $G(r_1, r_2, t)$, which shows the probability of finding an electron at r_1 at $t = 0$ will be found at r_2 at a later time t. Going from real space and time to momentum and energy will give us $G(\mathbf{k}_1, \mathbf{k}_2, E)$. In this picture, Green's function gives the probability of scattering of an electron in state $\mathbf{k}_1$ to state $\mathbf{k}_2$ with transferring energy E. If we neglect the non-diagonal parts of Green's function[1] then we will have $G(\mathbf{k}, E)$, which means scattering from momentum $\mathbf{k}$ to $\mathbf{k}$ (i.e. the momentum is conserved) with transferring energy E. The imaginary part this Green's function is spectral function $A(\mathbf{k}, E)$. To be more explicit,

$$\begin{aligned} G(\mathbf{k}, E) &= \left\langle \Psi_i(N) \left| c_{\mathbf{k}}^{\dagger} \frac{1}{E - H + \mathtt{i}\delta} c_{\mathbf{k}} \right| \Psi_i(N) \right\rangle \\ &= \sum_s \left\langle \Psi_i(N) \left| c_{\mathbf{k}}^{\dagger} \frac{|\Psi_s(N-1)\rangle \langle \Psi_s(N-1)|}{E - H + \mathtt{i}\delta} c_{\mathbf{k}} \right| \Psi_i(N) \right\rangle \end{aligned} \tag{3.25}$$

where δ is an infinitesimal positive number. Rearranging the above equation,

$$G(\mathbf{k}, E) = \sum_s |\langle \Psi_s(N-1) | \Psi_i(N-1) \rangle|^2 \frac{1}{E - E(\mathbf{k}) + \mathtt{i}\delta} \tag{3.26}$$

Now clearly you can see the spectral function in the above equation. Using the delta function property,

$$\frac{1}{E - E' \pm \mathtt{i}\delta} = P\left(\frac{1}{E - E'}\right) \mp \mathtt{i}\pi\delta(E - E') \tag{3.27}$$

we get

$$\mathrm{Im}G(\mathbf{k}, E) = \pi \int_{-\infty}^{+\infty} \mathtt{d}E' A(\mathbf{k}, E') \delta(E - E') \tag{3.28}$$

or

$$A(\mathbf{k}, E) = \frac{1}{\pi} |\mathrm{Im}G(\mathbf{k}, E)| \tag{3.29}$$

[1]The Green's function here is a matrix in k-space basis.

In the simplest case, absence of interaction, Green's function is,

$$G^0(\mathbf{k}, E) = \frac{1}{E - E^0(\mathbf{k}) - \mathtt{i}\delta} \tag{3.30}$$

where $E^0(\mathbf{k})$ is $\frac{\hbar^2\mathbf{k}^2}{2m}$ which is the kinetic energy of a free electron with momentum $\hbar\mathbf{k}$, so the spectral function will be

$$A^0(\mathbf{k}, E) = \frac{1}{\pi}\delta(E - E^0(\mathbf{k})) \tag{3.31}$$

where as we expect for non-interacting system, spectral function is a delta function at the energy of the electron, i.e. the Koopmann energy. Now if we switch on the electron-electron interaction, the change in the energy of independent electron can be added to it. The addition is called self-energy $\Sigma(\mathbf{k}, E)$ (provided the perturbation theory is valid, since we are adding the change in the system to the original system).

$$\Sigma(\mathbf{k}, E) = \mathrm{Re}\Sigma + \mathtt{i}\Sigma \tag{3.32}$$

which gives the interaction green's function

$$G(\mathbf{k}, E) = \frac{1}{E - E^0(\mathbf{k}) - \Sigma(\mathbf{k}, E)} \tag{3.33}$$

therefore the spectral function is

$$A(\mathbf{k}, E) = \frac{1}{\pi}\frac{\mathrm{Im}\Sigma}{(E - E^0(\mathbf{k}) - \mathrm{Re}\Sigma)^2 + (\mathrm{Im}\Sigma)^2} \tag{3.34}$$

For non-interacting system, we have to be able to recover the previous results. So the poles of $G(\mathbf{k}, E)$ are spectroscopic energies in the interacting system, in the same way, the poles of $G^0(\mathbf{k}, E)$ are the non-interacting spectroscopic energies. To the first order,

and assuming $\mathrm{Re}\Sigma \gg \mathrm{Im}\Sigma$, the poles (roots of denominator) are:

$$E^1(\mathbf{k}) - E^0(\mathbf{k}) - \Sigma(\mathbf{k}, E^1(\mathbf{k})) = 0 \tag{3.35}$$

For $\Sigma = 0$ the pole is at $E^1(\mathbf{k}) = E^0(\mathbf{k})$ as we expect, since there is no interaction. The pole energy is usually written as

$$E^1(\mathbf{k}) = \mathrm{Re}(E^1(\mathbf{k})) + \mathtt{i}\mathrm{Im}(E^1(\mathbf{k})) \tag{3.36}$$

where the pole occurs at the real part and the imaginary part is the width of the pole.

If the self-energy is small, i.e. there is a weak interaction, it is better to decompose the Green's function into a pole part (which gives $G^0(\mathbf{k}, E)$ for vanishing Σ) and a term that contains the "rest", which is called the incoherent part of Green's function, G_{inc},

$$G(\mathbf{k}, E) = \frac{Z_{\mathbf{k}}}{E - (\mathrm{Re}E^1(\mathbf{k}) + \mathtt{i}\mathrm{Im}E^1(\mathbf{k}))} + (1 - Z_{\mathbf{k}})G_{inc} \tag{3.37}$$

and

$$A(\mathbf{k}, E) = \frac{1}{\pi} \frac{Z_{\mathbf{k}}\mathrm{Im}(E^1(\mathbf{k}))}{\left[E - \mathrm{Re}E^1(\mathbf{k})\right]^2 + \left[\mathrm{Im}E^1(\mathbf{k})\right]^2} + (1 - Z_{\mathbf{k}})A_{inc} \tag{3.38}$$

where $Z_{\mathbf{k}}$ is a normalization constant, which is called weight of the quasi-particle[1] pole and $E^1(\mathbf{k}) = E^0(\mathbf{k}) + \Sigma(\mathbf{k}, E^1(\mathbf{k}))$. Now Eq.3.38 gives information about the quasi-particle picture of interacting system. The pole part of G gives the spectrum of electron excitations with a renormalized energy (mass) and a finite width. In the same way G^0, which is the Green's function for non-interacting system, yields the spectrum with

[1]Quasi-particle is particle plus its environment, or plus its interaction. When an electron interacts with lattice (i.e. environment), it gains an effective mass(like your body weight on moon! your mass is constant, but your weight is depends on where do you live or your environment). Therefore its energy is somewhat different too. The *bare particle* plus its interaction is is called a *dressed* particle. the dressed particle has a different energy, $\epsilon_{quasi} - \epsilon_{bare} = \epsilon_{selfenergy} \equiv \Sigma$. Σ is self-energy which is a complex quantity. The real part gives the change in the energy of quasi-particle (as it enters the new environment) and the imaginary part represents the change in the life time of quasi-particle.

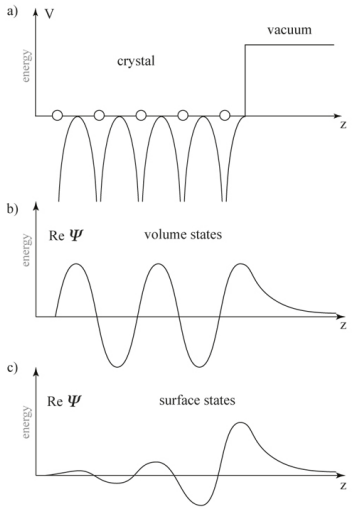

Figure 3.7: a) Left shows the periodicity of lattice and right is the vacuum. Notice the vacuum has a higher energy, so electrons inside the material will see the interface like a step potential. b) The wave function inside the material is periodic while in vacuum it is exponentially decaying. c) The surface state decays inside the crystal, and it mainly exist near the surface, hence surface state.

single-electron energy $E^0(\mathbf{k})$ with infinite life time (remember this spectrum are delta functions). The electron in an interacting system are "dressed" by virtual excitation that move with them coherently.

3.4 PES at the Surface

This chapter is closely based on Hufner's book.

3.4.1 Surface states

Surface is where the periodicity of crystal is truncated, i.e. at one side there are atoms which are repeated in an order and on the other side, there is nothing, vacuum. The interface between the material and vacuum is called surface. At one side of surface (material side) the electronic wave function is *propagating*, while on the other side (vacuum) wave function is *exponentially decaying*. This abrupt change in the wave function can produce new electronic states which are fundamentally happening because of this abrupt truncation of lattice, i.e. surface.

One can look at this problem like a scattering problem, electron waves scatter from the step potential (vacuum). The back-scattered part decays as an oscillatory function (because electron wave function still sees the periodic lattice potential). The transmitted part again decays, but exponentially, Fig.5.7 shows this behavior.

At the surface of a real material, the interface is not a step function, but the interface smears out due to surface reconstruction, dangling bonds and etc. Therefore some of the electrons can actually leak into the vacuum near the surface. This type of states that live near the surface are called *Shockley states*. As mentioned before, Shockley states are near the surface, but they are not traveling waves, but they are decaying waves. Thus their wave vector is not real like bulk states. Surface states wave vector is complex. Because of the imaginary part, surface states do not belong to bulk states, therefore they will happen in the band gap where there are no bulk state. In the Shockley picture, one should distinguish between surface state (located in energy gaps and decay rapidly in the crystal) and surface resonance (may overlap with bulk-band states and decays slowly into crystal).

In Shockley picture, a surface state exist because there is sudden truncation in the periodicity of lattice. Another way of introducing surface states is brought by Tamm. In Tamm picture, a surface state happens because near the surface, the crystal field is not symmetric (the same) on both sides of atom (hence orbitals), thus part of bulk-band splits into a surface state.

3.4.2 Experiments on surface state

- Surface state should not depend on the photon energy, because it only depends on $\mathbf{k}_{\|}$
- Surface state should be in the gap of bulk band structure
- Contamination immediately destroys surface state. Small amount of H or O can diminish the surface state

One way to predict existence surface state is to determine in which direction there is a gap in Fermi surface. For example in Au, there is a gap from Γ to toward (111) direction in Brillouin zone. So Au (111) is expected to have a surface state.

3.4.3 Surface core-level shift

Density of States (DOS) for bulk valence electrons is larger than valence electron DOS at surface. The reason is due to the fact that the coordination number for surface atoms is smaller (surface is truncated), basically surface atoms have fewer neighbor atoms. Also the energy of core-level states depends on valence electron configuration, which leads us to the conclusion that surface atoms have a different core-level shift comparing to bulk atoms. This difference will produce another peak, next to bulk core-level peak, which shows the core-level shift. To make sure that this shift is only due to surface core-level, one can deposit an over layer on the surface, like hydrogen gas. A layer of hydrogen atoms on the surface will greatly reduce the surface core-level peak intensity while the bulk intensity will remain as before(like fig. 8.28 Hufner).

One should keep in mind that to detect a surface core-level peak, or surface state, using a photon with energy around 50 eV would be better because the inelastic mean free path of photo-electron will be smallest (according to universal curve), therefore the outgoing electrons are mostly coming from surface atoms and bulk contribution will be less pronounced (like Fig.8.28 of Hufner).

It is interesting to note depending on the surface adsorbate, surface core-level shift can move toward higher or lower binding energies. Fig.3.8 shows this effect. Using a simple charge transfer picture, one can see that due higher electronegativity of O, W gives away its valence electron to O, hence W becomes W^{3+}, therefore surface atoms will lose electron which makes it harder to lose more electron, thus the binding energy of electrons coming from surface W atoms will be higher. While for the case of Alkali metals, there is no or very little charge transfer, as a result the surface core-level remains almost unaltered.

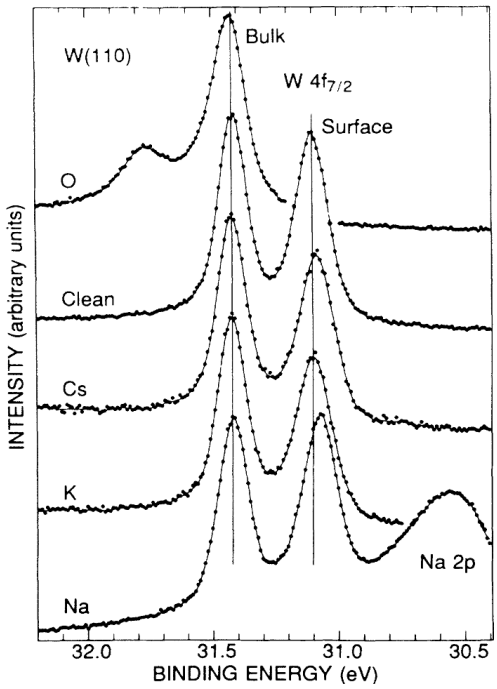

Figure 3.8: The change in surface core-level is presented. For clean W(110) surface, the surface core-level shift is toward lower binding energies. Depositing half a monolayer of O brings the surface core-level to higher binding energy, while depositing one monolayer of Cs, K or Na keeps the surface core-level shift on the lower binding energy [6].

Chapter 4
Polar surfaces and interfaces

4.1 Introduction

Surface of materials are of interest of several fields of research. Catalysis, metallurgy and corrosion, electronics and magnetic recording are couple of famous examples. The wide application of surface active materials along with unexpected emergent properties at the surface, represents the importance of surface physics. With the advent of sophisticated thin film growth technique and heterostructure fabrication, understanding of surface and interface has become more important than before.

The structure, electronic properties, stoichiometry as well as directionalitiy of a surface defines its properties. In this chapter, an interesting class of surface and interfaces will be studied. These surface and interfaces possess net charges at their outmost layer or junction, respectively. Presence of unbalanced charge will cause divergence of free energy, therefore the unbalanced charges need to be compensated. There are several mechanism for minimizing free energy in this class of surfaces which will discussed in the following.

4.2 Polar surfaces

Every single crystal is interfaced with vacuum through its surface. The surface is defined by the truncation direction of the bulk single crystal. Depending on truncation of bulk single crystal, cleaving direction, different surfaces with different stoichiometry, structure and electronic properties are created and exposed to vacuum. Since the symmetry is broken at the surface, or interface of material with vacuum, often new physical properties appear at the surface. This new broken symmetry state might bring the surface to a new ground state which is different than bulk. In this sense, comparing to bulk, the surface has a different Hamiltonian. Therefore, the ground state of surface

lies where the surface energy is minimum which is the most stable state of the surface. Surface energy can be defined by the work needed to build an area of a particular surface. Another way to define it is to relate it to the work required to cut a crystal and creating two surfaces. This way, the unit surface energy is half of the cohesion energy, the energy spent to cut the bonds and cleave the bulk crystal to create two surfaces. In real world, cutting bonds will lead to dangling bond creation which immediately react with the medium surrounding them to lower their energy. This is called passivation or adsorption will stabilizes the surface. Now it is clear that the stability of the surface is determined by surface energy, E_s which can be defined as [19],

$$\begin{aligned} E_s = &(Cohesive\,energy\,of\,finite\,crystal) - \\ &(Number\,of\,atoms) \times (Cohesive\,energy\,per\,atom\,in\,infinte\,crystal) \end{aligned} \tag{4.1}$$

which is the excess energy associated with the surface. It is known that presence of electric dipole moment in the unit cell, perpendicular to the surface leads to divergence of the surface energy.

Surfaces are the created by abrupt truncation of bulk that can be thought of stacking of planes perpendicular to surface. According to Tasker [19], based on charge distribution, surfaces can be categorized in three groups, stacking of neutral planes, stacking of charged planes with no dipole moment perpendicular to the surface and stacking of charged planes with dipole moment perpendicular to the surface. Fig.4.1 shows these three surface types.

- Type I: Net charge on each plane is zero. Example is NaCl (001). There is no potential or electric field produced as anion and cation sublattice will cancel eachother (Fig.4.1a).

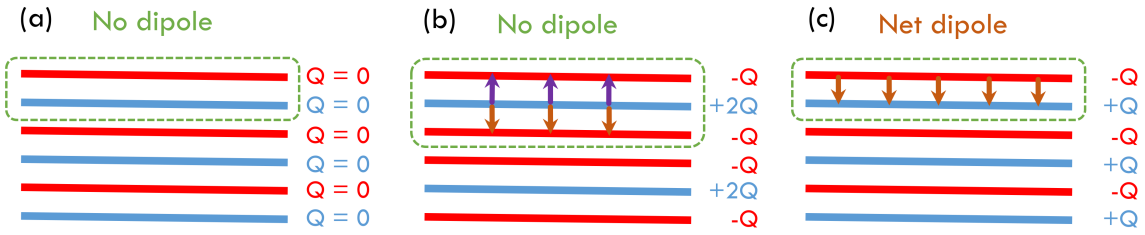

Figure 4.1: Surface with different charge distribution. a) Type I, The net charge on the surface is zero. b) Type II, the net charge on the surface is non-zero but the dipole moment in the unit cell is zero. c) Type III, the net charge on the surface is non-zero and the unit cell has a net moment.

- Type II: Each plane has a net charge while the repeating unit does not have a dipole moment perpendicular to the surface (Fig.4.1b).

- Type III: Alternative stacking of charged planes that produce a dipole moment perpendicular to the surface (Fig.4.1c).

In Type III surface, the two plane unit creates a long range (infinitely) potential that its magnitude is,

$$\mathrm{V} = 2\pi\sigma a \tag{4.2}$$

where σ is the surface charge density and a is inter-planar distance. It is important to notice that this potential increases with distance and does not get canceled. In general stacking of charged planes can be depicted as in Fig.4.2. The presence of dipole moments leads to divergence of Madelung sum. In other work, Madelung energy does not decay with distance and consequently the Madelung sum cannot be truncated and must include contribution from every plane out to the surface and this is the root of the problem. The potential at any ion site never reaches a constant bulk value.

4.3 Polar surfaces in transition metal oxides

The above discussion about polar surfaces work very well for ionic crystal. In the case of transition metal oxide, the bonds are not completely ionic. For example, $SrTiO_3$,

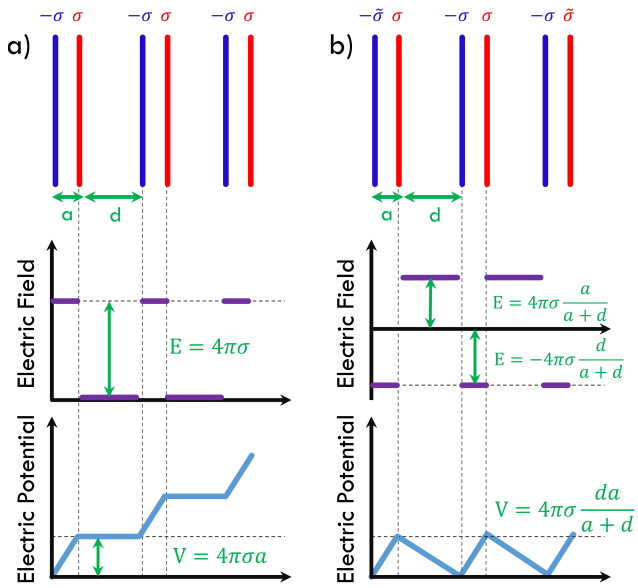

Figure 4.2: Type III surface. a) Stacking of charged layers creates dipole moments that diverge the potential energy. b) Charge re-arrangement at the surface cancels the dipole moment and the energy will not diverge.

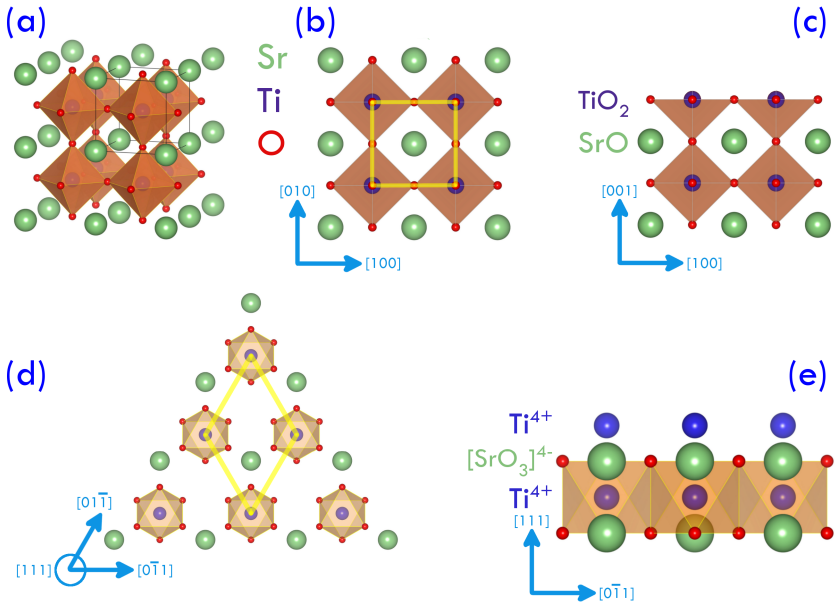

Figure 4.3: a)$SrTiO_3$ with perovskite structure. b) The TiO_2 terminated $SrTiO_3$ (001) is shown. The surface unit cell is highlighted in yellow. c) Stacking sequence of $SrTiO_3$ (001). Nominal charge of each layer is zero. d) The Ti terminated $SrTiO_3$ (111) is shown and the unit cell is highlighted in yellow. The symmetry if this surface is C_{3v}. e) The stacking sequence of $SrTiO_3$ (111) is shown. Each layer bears some uncompensated charge.

an insulator/semi-conductor[1] transition metal oxide with perovskite structure, due to partial covalency of Ti and O bond, it is not accurate to use the nominal ionic charges. The consequence of the mix character bonds is that even the surfaces that are non-polar by definition, can be polar and hence active. $SrTiO_3$ (001) is an example, where the nominal charges are Sr^{2+}, Ti^{4+} and O^{2-}. The termination can be SrO or TiO_2. Usually, the TiO_2 terminated surface is of more interest, due to its catalytic properties and wide use of it as a substrate. In this case, the surface is composed of Ti^{4+} and O_2^{2-}. Counting the nominal charges shows that the surface has to be neutral, but on the other hand, looking at the covalent character of the bonds, the surface is weakly polar.

4.3.1 Surface of $SrTiO_3$ (001)

The $SrTiO_3$ (001) surface is weakly polar and the free energy of intact surface should diverge. Therefore a natural question would be, what is the mechanism to minimize the surface energy. To further understand the structure of surface of $SrTiO_3$ (001), we have used Low energy electron diffraction (LEED). The $SrTiO_3$ (001) was prepared by Acetone, alcohol cleaning followed by DI-water and HF etching. After etching the sample was annealed at 920 °C in oxygen for 3 hours. After sample preparation, the surface morphology and structure of the sample was investigated. Fig.4.4a shows the scanning tunneling microscope image of processed sample. The surface is atomically flat and shows step-terrace morphology. The step height is 3.9 Å which is the lattice constant of cubic $SrTiO_3$. Fig.4.4b,c shows the LEED image of $SrTiO_3$ (001). The surface has a four fold symmetry. The background of the LEED image is not considerable which means the surface is well-ordered. The above data shows that the processing method effectively created an atomically flat well-ordered surface.

To gain more information about the detail of surface structure, the LEED I(V) data were collected. In this method the intensity of each LEED spot as a function of

[1]The 3-3.2 eV gap of $SrTiO_3$ puts it on the borderline of semi-conductors and insulators.

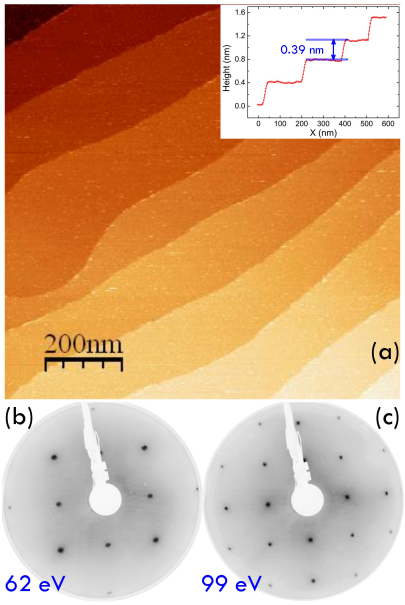

Figure 4.4: a) The STM image of $SrTiO_3$ (001). The step and terraces are seen. The inset shows that the steps are one unit cell high. The average size of flat terraces is about 175 nm. b ,c) The LEED image of $SrTiO_3$ (001) at 62 eV and 99 eV. The images were taken at room temperature.

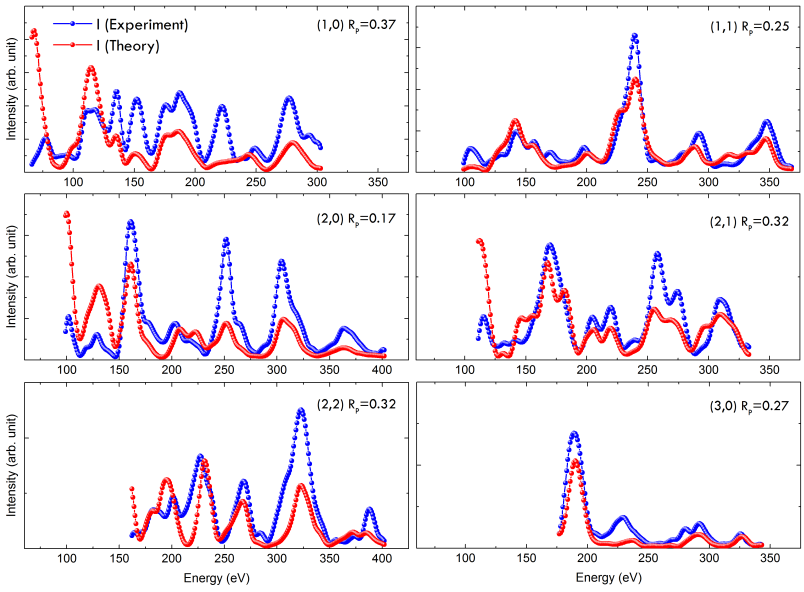

Figure 4.5: The LEED I(V) data of $SrTiO_3$ (001) surface. The experimental spectra and theoretical modeling is shown. The overall Pendry R-factor (R_p) is 0.28 which is considered reliable.

electron beam energy is recorded. In order to reduce the background noise and thermal broadening, the LEED I(V)data were collected at 90 K. Using symmetrized automated tensor LEED program (SATLEED), this surface was modeled and studied. Fig.4.5 shows the I(V) characteristics of the this surface, experimentally and theoretically. Each LEED spot was averaged by its symmetrically equivalent counterpart. In total six averaged LEED spot were used for simulation and modeling. The R-factor for each spot is shown. Since the surface was intentionally prepared to be TiO_2 terminated, the SATLEED model was a TiO_2 teminated surface[1]. One unit cell below the surface was allowed to relax. The results of the calculation are shown in Fig.4.6 and compared to theoretical (density functional theory (DFT)) result [7]. The result of this work shows that the Ti atoms at the top layer move inward while in-plane[2] O atoms at the top layer move in the opposite direction, outward. Our result shows that Ti atom displacement is $-0.0632\mathring{A}$ while DFT predicted it to be $-0.088\mathring{A}$ which are close. However, for in-plane O, the displacement is $+0.1022\mathring{A}$ while according to DFT calculation it is $-0.005\mathring{A}$. For the second layer, SrO plane, our result show that Sr atoms move outward, $+0.0213\mathring{A}$ and O top atom slightly moves outward, $+0.0063\mathring{A}$, while DFT displacement for Sr and O top are $+0.139\mathring{A}$ and $+0.022\mathring{A}$, respectively. For the top layer, although the sign of absolute value of displacement does not agree with DFT, but the relative displacement of the atoms create the same dipole moment. For the second layer, the magnitude of displacement in our work does not agree with DFT while the direction of polar vector for the plane quantitatively agrees. Our result as well of DFT result show that the relaxation is within the first two layers and the third layer does show an appreciable displacement of atoms[3].

[1]The SrO termination was modeled as well and since the R-factor was always around 0.85 the data are not reported here. This actually again shows that the sample preparation was effective in preparing the TiO_2 terminated surface.

[2]The oxygen in the plane of Ti is called, in-plane O and the oxygen in the Sr plane is called O top.

[3]The author is aware of another LEED I(V) simulation on the $SrTiO_3$ (001) surface. The work is acknowledged but results are not discussed here due to very large R-factor, 0.53 [20].

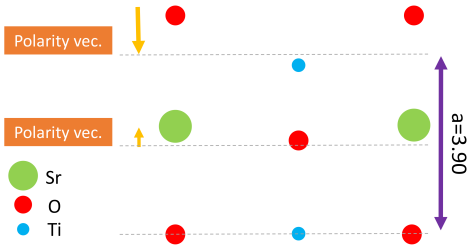

Element	Displacement from the Plane LEED (Å)	Displacement from the Plane DFT (Å)
O in-plane	+0.1022	-0.005
Ti	-0.0632	-0.088
Sr	+0.0213	+0.139
O top	+0.0063	+0.022

Figure 4.6: The structural information from LEED I(V) calculation is shown and compared to density functional theory calculation from Ref. [7]. The surface relaxes in a way to minimize its energy. The first layer shows an inward polar vector while the second layer shows the opposite.

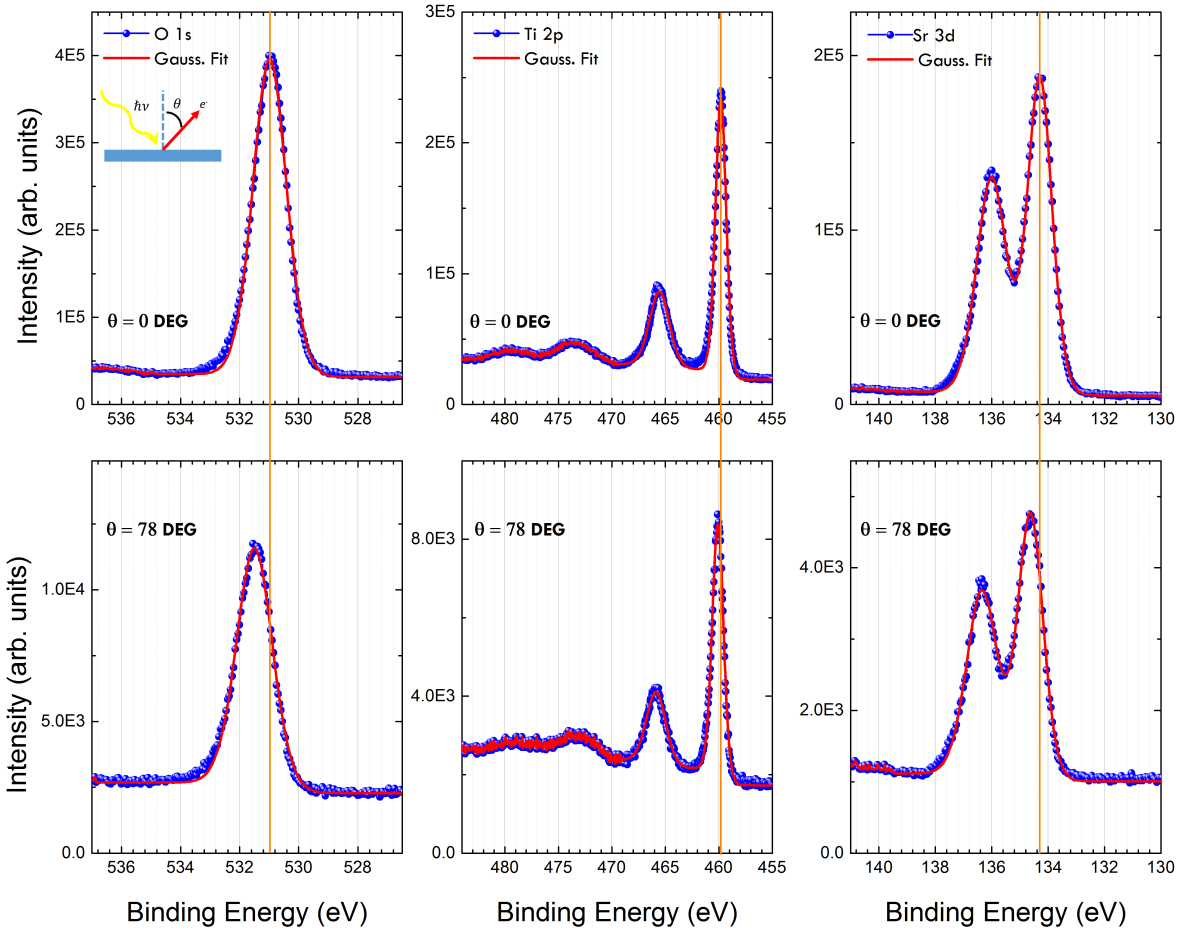

Figure 4.7: The XPS spectra of O 1s, Ti 2p and Sr 3d core levels and their Gaussian fit, at normal angle (top) and $\theta = 78°$ (bottom) are shown. The orange line shows the chemical shift of each core level with respect to normal emission. The schematic of angle dependent XPS is shown.

From the above result, one can see although the nominal charge counting on the surface results in a non-polar surface, the $SrTiO_3$ (001) surface is a polar surface. To minimize the free energy at the surface, the atoms displace to remove the polarity.

In order to understand the chemistry and stoichiometry of the surface, monochromatized X-ray photoemission spectroscopy (XPS) is performed. For this experiment, the samples were prepare ex-situ with the method described earlier and transferred to vacuum chamber. Then they were degassed and immediately transferred to XPS chamber for measurements. Prior to measurement, the electron energy analyzer was calibrated with Au $4f_{7/2}$. Fig.4.7 shows the XPS result. The XPS spectra of O 1s, Ti 2p and Sr 3d for bulk (normal emission) and surface ($\theta = 78^\circ$) are shown. They are in general agreement with previous published data, with minor differences possibly coming from use of non-monochromatized X-ray and different processing methods [21, 22]. It is worthwhile to notice that the processed samples are extremely clean. The fact that there is no shoulder on the O 1s spectra, bulk or surface, shows that the surface is free from any kind of contamination. Each spectra is fitted with a Gaussian-Lorentzian function. The fitting results are summarized in the table 4.1. The O 1s peak is located at 531.0 eV, while the high-angle spectra is shifted by 0.5 eV to higher binding energy. Looking at high angle XPS Ti 2p and Sr 3d, these peaks are shifted by 0.3 eV to higher binding energy, comparing to normal angle. It is seen that 0.3 eV chemical shift is common between all peaks, therefore might be attributed to reducing of core-hole screening. The additional 0.2 eV chemical shift of O 1s at high angle emission can be understood in the light of LEED I(V) structural refinement. LEED shows that the surface O has a strong outward motion while Ti moves inward, which creates an electric dipole. The direction of this dipole is inward which could induce charge transfer from O 2p to Ti 3d and change the initial state of O 1s core level. This observation can explain more insulating behavior of surface comparing to bulk. After normalizing the peak areas by inelastic

Table 4.1: The fitting results of XPS data.

	Peak position (±0.15 eV)		FWHM (eV)		Area	
	$\theta = 0$	$\theta = 78$	$\theta = 0$	$\theta = 78$	$\theta = 0$	$\theta = 78$
O1 s	531.0	531.5	1.34	1.43	5.25E5	1.41E4
Ti $2p_{3/2}$	459.8	460.1	1.18	1.24	4.07E5	1.30E3
Sr $3d_{5/2}$	134.3	134.6	1.03	1.05	3.68E5	7.85E3

mean free path and Scofield cross-sections [23, 24], the area ratio of Ti 2p/Sr 3d for bulk and surface are 1.1 ± 0.2 and 1.7 ± 0.3, respectively. This shows that the processing method was effective in selective removal of Sr from the surface and agrees with our LEED I(V) characterization.

4.3.2 Surface of $SrTiO_3$ (111) as a substrate

In this section the structural, electronic and stoichiometric properties of $SrTiO_3$ (111) will be discussed. The of aim this section is to understand the surface properly and then prepare it in a way that is best for growth of thin films. A special attention will be paid to the behavior of surface at high temperatures. This is crucial since it will help to understand how the substrate surface will behave at the time of growth.

According to Taskers classification [19, 25], the surface of $SrTiO_3$ (111) is Type III which is constructed by the stacking of charged planes in a way that there is a net dipole moment perpendicular to the planes, as shown in Fig.4.3d,e. Ternary (111) perovskite oxide[1] surfaces are classified as type III surfaces which are called polar surfaces. In this type of surface, due to the presence of net dipole moment, the electrostatic surface energy diverges. This is the reason for the instability of type III surfaces which is sometimes referred to as polar catastrophe. In processing, a polar surface is likely to reconstruct itself to minimize its energy by: structural reconstruction, electronic reconfiguration, changes in surface stoichiometry, faceting, as well as adsorbing atoms/molecules from

[1]The general formula is ABO_3.

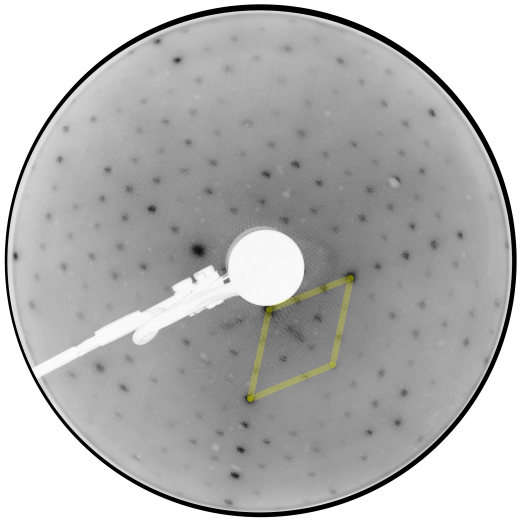

Figure 4.8: 3×3 reconstruction at the surface of $SrTiO_3$ (111) at 103 eV. The unit cell is shown in yellow.

the environment [26, 27]. For oxide film epitaxial growth on such polar surface, a pristine surface without reconstruction is desired in order to reduce the structural and/or chemical complexity at interface.

The (111) direction of SrTiO3 (STO) is formed by stacking Ti^{4+} and $[SrO3]^{4-}$ layers with an inter-planar distance of 2.25 AA, as shown in Fig.4.3d,e. There are two common methods to prepare STO (111). One is by using in-situ cycles of ion-sputtering and annealing. The resultant surface prepared by this method can be free of contamination, but also exhibits sever structural reconstructions with different chemical composition compared to the bulk. Surface reconstruction, including $(n \times n)$ (n=4,5,6) [28–30], $\sqrt{(7)} \times \sqrt{(7)}$R19.1° and $\sqrt{(13)} \times \sqrt{(13)}$R13.9° [31], have been observed depending on the details of processing procedure. We have been able to see some of these reconstructions. For example, as shown in Fig.4.8, after annealing the sample in 1100 °C, a 3×3 reconstruction appears and from charging on the the LEED screen, one can conclude that the reconstructed surface is more insulating than the non-reconstructed surface. These surfaces with these reconstructions are not favorable for oxide epitaxy, yielding an interface with complicated structure and chemical intermixing. The other common method

to prepare STO (111) surface, e.g., a Ti-terminated surface, is through ex-situ selective chemical etching of the SrO_3 layer followed by thermal annealing [32–34]. Although the latter method produces an atomically flat substrate, the epitaxial growth of materials on STO (111) is still complicated, since interface intermixing can occur [35–37]. Surface contamination is also an unresolved/unavoidable issue due to ex-situ sample preparation. The surface can also reconstruct, depending on processing conditions. Therefore, it is important to determine the structure, chemical composition, and electronic evolution of this surface with different processing procedures, at elevated temperatures that are appropriate for film growth. Understanding how the surface evolves at the desired growth conditions allows one to optimize the growth temperature accordingly.

The samples used for this work were Nb-doped SrTiO3 (111). They were cleaned with acetone and ethyl alcohol, then sonicated in deionized (DI)-water with a pH of 5.5 at room temperature for 4 minutes. This was followed by soaking in Buffered HF with the pH of 4.5 for 30 seconds. Finally, samples were annealed at 930 °C for 150 minutes in oxygen. The DI-water etching time and its temperature are important, because etching for too long will cause surface roughness, and high temperature etching will result in faceting after annealing.

The morphology and surface structure of the ex-situ prepared sample was investigated in the UHV chamber using STM and LEED. Fig.4.9 shows the STM image and the line profile, revealing step-terrace morphology with a step height that corresponds to the distance between two Ti layers (2.2 Å, Fig.4.3e). The terrace width depends on the miscut angle, which in our case is 65 Å. The symmetry at the surface is displayed in the LEED pattern shown in Fig.4.9 (c) and (d), displaying a (1×1) symmetry at T = 25 °C and 600 °C, respectively. There is no surface reconstruction observed at higher temperatures (up to 740 °C). At 740 °C it is difficult to record LEED patterns due to glowing of the hot sample. Even in this temperature there is no reconstruc-

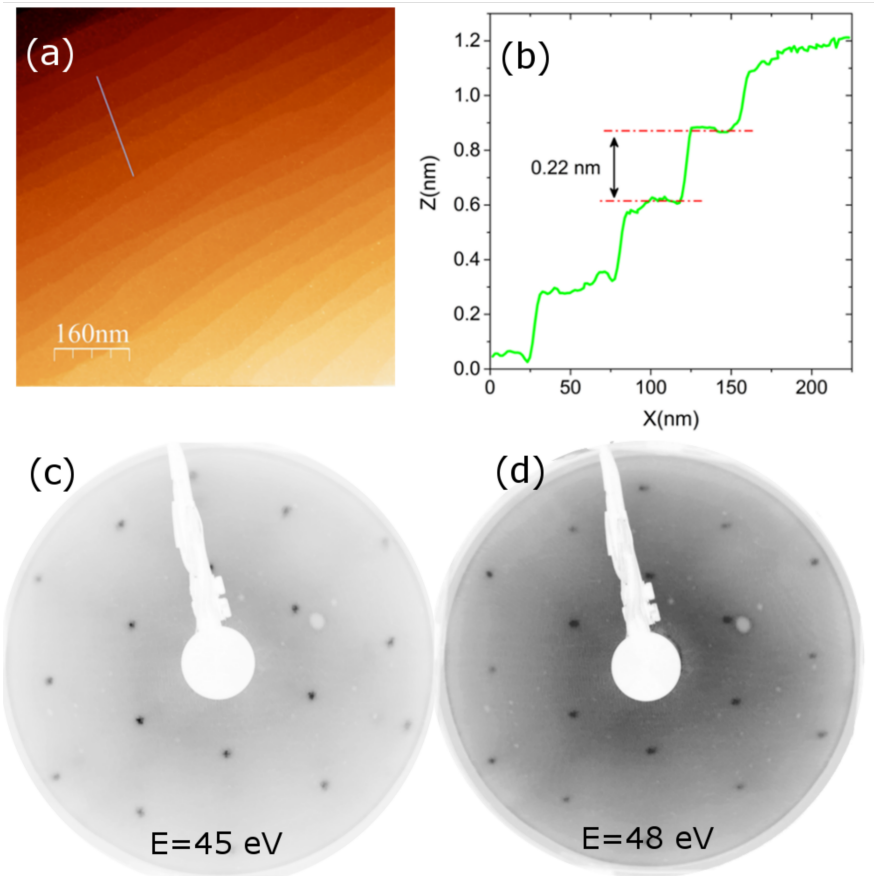

Figure 4.9: (a) STM image of SrTiO3 (111) surface taken at room temperature after preparation and (b) the line profile across the steps marked by the line in (a). (c) and (d) display the LEED p(1×1) pattern of STO (111) taken at room tempearture and 600 , respectively.

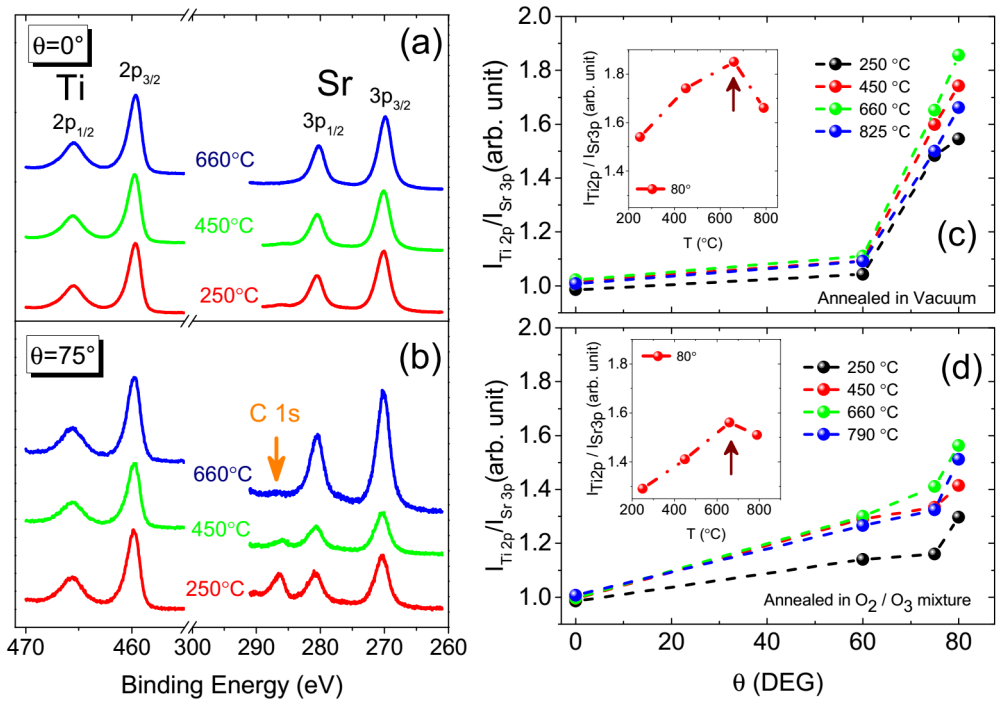

Figure 4.10: ARXPS spectra measured at room temperature for Ti 2p and Sr 3p core levels of SrTiO3 (111) surface with photoelectron emission angle (a) $\theta = 0°$ and (b) $\theta = 75°$ for different annealing temperatures in vacuum. The inset shows the schematic setup of ARXPS. The arrow points to carbon peak that disappears as the temperature increases. The Ti 2p/Sr 3p intensity ratio as a function of emission angle for the surface annealed at different temperatures (c) without and (d) with oxygen/ozone is plotted. The insets show the ratio as a function of temperature at $\theta = 80°$.

tion. This is no surprise since reconstruction in vacuum, all occur above 1000 °C. As previously stated, other studies have reported surface reconstruction on the STO (111) surface [28, 30, 31, 38] after in-situ treatments using various sequences of sputtering and annealing. Also, most of the observed reconstructions appear after annealing at very high temperature. For example, 3×3 and 2×2 reconstructions appear after annealing at 1150 °C and 1280 °C, respectively [39]. It is worth mentioning that even after cooling down the sample to room temperature, the surface still maintains its 1×1 pattern with little higher background.

Chemical composition of the surface as a function of the processing and temperature was determined using ARXPS. Fig.4.10 summarizes the ARXPS results of Sr and Ti

core levels, taken at room temperature, for the surface of SrTiO (111), annealed in-situ in both vacuum and oxygen at different temperatures. Fig.4.10 (a) and 3(b) show the evolution of the Sr 3p and Ti 2p spectra as a function of annealing (in vacuum) temperature for normal emission ($\theta = 0°$) and emission angle $\theta = 75°$, respectively. Since $\theta = 75°$ data is more surface sensitive, they show the presence of C contamination, which goes away with high temperature (650 °C) annealing. Using the Tanuma et al. method [40], we calculated the mean free path of Ti 2p (21.1 Å) and Sr 2p (24.3 Å), which illustrates that the average escape depth of electrons at $\theta = 80°$ is about 3.6 Å, such that only the surface layer is probed at high emission angles.

Using sensitivity factors for Ti and Sr, which depend on the Scofield cross section [24] and mean free path of the photoelectron [40], the relative change of the ratio between Ti and Sr core level intensities as a function of emission angle can be converted into the Ti vs. Sr concentration as a function of depth. Fig.4.10 (c) and (d) display the measured intensity ratio ($I_{Ti\,2p}/I_{Sr\,3p}$) as a function of emission angle, for annealing in vacuum and in oxygen/ozone, respectively. Both procedures of in-situ annealing produce a surface that is Ti rich, but there is more Ti present at the vacuum annealed surface, when compared to the oxygen annealed surface. Inspection of the data reveals that the Ti/Sr surface concentration changes non-monotonically with annealing temperature, peaking at $\sim$ 660 °C. The insets in Fig.4.10 (c) and (d) show the percentage of the surface that is Ti terminated, assuming that in the bulk the ratio is 1. For vacuum annealed samples, the maximum Ti concentration occurs at $\sim$ 660 Å with a value of 90% $\pm$ 10 %, i.e. Ti terminated. But for O2/O3 annealed samples, the Ti-termination percentage has fallen to $\sim$ 80% at the same temperature. The conclusion is that ex-situ chemical etching followed by vacuum annealing successfully removes the SrO_3 layer and creates the best Ti-terminated surface at $T_c \sim 660$ °C. The introduction of oxygen during annealing reduces the degree of Ti at the surface.

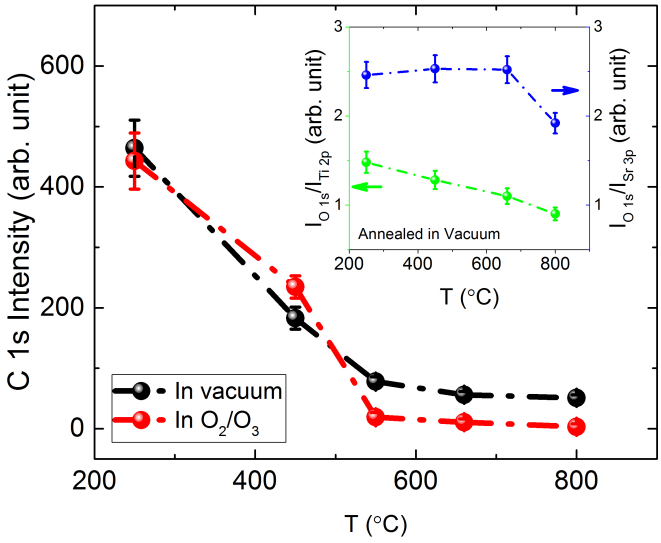

Figure 4.11: The change in carbon intensity as a function of annealing in vacuum and oxygen mixture. The inset shows the change of O_{1s}/Ti_{2p} intensity and O_{1s}/Sr_{3p} intensity annealed in vacuum as a function of temperature. The measurements were performed at room temperature.

Considerable amount of Carbon (C) contamination is present on the surface before the in-situ processing, but disappears at high annealing temperatures. As shown in Fig.4.10(b), an appreciable C peak appears at 286.2 eV in the spectra and gradually diminishes with increasing annealing temperature. C contamination is commonly observed on STO surfaces before sputtering [41], and could stabilize the surface of $SrTiO_3$ (111) and minimize the surface free energy. The C 1s core level signal shown in Fig.4.10(b) is $\sim$ 40% of the O 1s signal. Given that the surface coverage is only $\sim$ 60% Ti (inset Fig.4.10(c)) and that the photoionization cross sections are nearly identical, there is a large fraction of a monolayer of C on the surface. The form of this carbon layer can be Ti carbide, graphite, or C bonded to O. The binding energy (286.2 eV) of C 1s [Fig.4.10(b)] is appreciably higher than the values reported for C-Ti (281.6 eV) or for C-C bond (284.8 eV), but exactly the one for CO-Ti bond [42–44]. This indicates that C in the form of CO bonds to surface Ti.

Fig.4.11 shows the C1s intensity as a function of temperature for both vacuum and

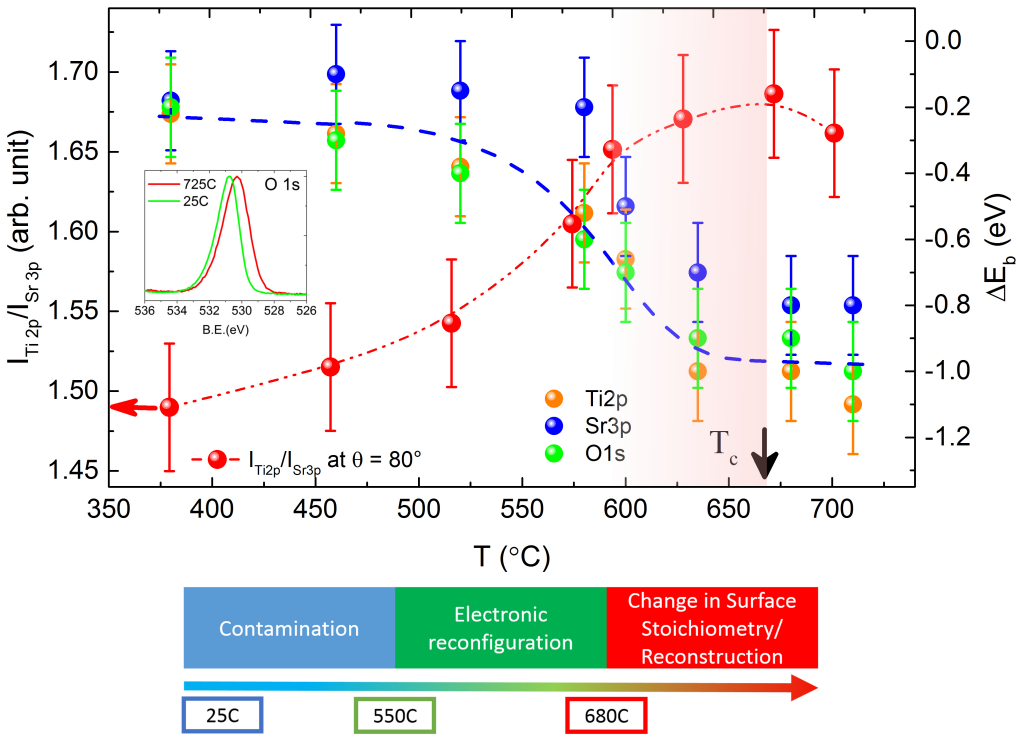

Figure 4.12: (*top*) The temperature-dependence of the binding energy (ΔE_b) for core levels of Ti 2p, Sr 3p and O 1s and the relative intensity ratio of Ti 2p and Sr 3p determined from ARXPS spectra for $SrTiO_3$ (111) surface. The data was taken at photoelectron emission anlge $\theta = 80^{c}$irc and elevated sample temperature. The inset shows the binding energy shift of O 1s to lower binding energy at 25 °C and 725 °C due to final state effect. (*bottom*) The schematic order of different mechanisms to minimize the free energy of polar surface as a function of temperature.

O_2/O_3 annealing. C leaves the surface as annealing temperature increases. As shown in the inset of Fig.4.11, the ratio of O 1s to Ti 2p decreases (Ti at surface increases) with increasing temperature, but the ratio of O 1s to Sr 3p remains constant, which means that the carbon leaves while bonded to an oxygen atom. Above 660 °C, the surface is already free from C, the Sr starts to segregate to the surface and the surface starts to lose oxygen, therefore the ratio of O 1s to Sr 3p drops. At high temperature (above $\sim$ 600 °C) the ratio of O 1s to Sr 3p remains constant because, as the C layer is removed, the underlying SrO_3 layer is more exposed.

In order to mimic the surface conditions for thin film growth, we carried out ARXPS

measurements with the sample held at elevated temperatures. The intensity ratio ($I_{Ti_{2p}}/I_{Sr_{3p}}$), measured at elevated temperature (Fig.4.12) displays the same general behavior seen in Fig.4.10(c), the $I_{Ti_{2p}}/I_{Sr_{3p}}$ ratio increases up to $\sim$ 660 °C. The binding energies of the Ti 2p, Sr 3p and O 1s core levels also show a temperature dependent shift that looks similar to the intensity ratio. The shift DeltaE_b is basically constant up to $\sim$ 500 °C and then drops by about 1 eV. This shift is not a chemical shift and therefore must be a final state effect. It has been observed using ARPES[1] [45, 46] that upon annealing, occupancy at the Fermi surface appears and the surface becomes metallic. It is speculated that the creation of oxygen vacancies upon annealing generates carriers to populate the surface state and form a Fermi surface [47]. Semi-empirical Hartree-Fock calculations by Pojani et al. [48, 49] support this ARPES observation. It is important to note that the drop in the binding energy coincides with the sudden increase of Ti concentration on the surface, thus indicating a correlation of surface metallicity and Ti concentration. During the ARXPS measurements, even at elevated temperatures, no sign of Nb was observed. This could be due to the very small Nb concentration of (only $\sim$ 0.1%).

Interestingly, the onset of the rising ratio between Ti 2p and Sr 3p, the drop in ΔE_b and the disappearance in the carbon core level concur around the same temperature. Therefore, it is clear that the $SrTiO_3$ (111) polar surface takes advantage of contamination as a passivation mechanism, electronic reconfiguration as a screening mechanism, and surface intermixing as the surface reconstruction mechanism, all to minimize the surface energy and avoid polar catastrophe. The mechanisms to avoid polar catastrophe and minimize surface energy are summarized in Fig.4.12. First, contamination is a mechanism to avoid polar catastrophe at surface temperatures below 550 °C. Then, electronic reconfiguration plays the major role in minimizing the surface energy, at the

[1] Angle-resolved photoemission spectroscopy

temperature range of 550-660 °C. Finally, as surface temperature go beyond 660 °C, structural reconstruction, including changes in surface stoichiometry starts to recover the charge neutrality of the surface. Therefore we propose the best temperature window for the thin film growth is between 600 °C and 660 °C, in which the surface is free from contamination and is maximally Ti-terminated.

4.4 Polar Interfaces

4.4.1 Introduction

Transition metal oxide heterostructures exhibit variety of remarkable interfacial properties due to the lattice mismatch, orbital character, charge transfer, polar mismatch, or broken symmetry [50]. For example, the interface of $LaAlO_3/SrTiO_3$ (001) has shown that a 2-dimensional electron gas (2DEG), coexists with superconductivity and ferromagnetism [51–53]. These unusual interfacial phenomena have ignited tremendous effort aimed at engineering or controlling interface properties [50, 54]. An important aspect of the search for and control of interfacial properties is the orientation of the substrate [55–57]. A prototype example is the $LaNiO_3/LaMnO_3$ superlattice in highly polar [111] direction, exhibiting an unusual coupling at the interface, which displays exchange bias between ferromagnetic $LaMnO_3$ and paramagnetic $LaNiO_3$ [58, 59]. It has been predicted [60], though yet to be verified [61], that superlattices of $LaNiO_3/LaAlO_3$ (111) and $LaNiO_3/SrTiO_3$ (111) are host to topological interface states that show transition to Mott state. The ability to create the sharp interface in these systems opens up the possibility of controlling parameters such as interfacial correlations and coupling as well as tuning of crystal field using strain and interface directionality to manipulate intriguing properties [62–64].

4.4.2 The case of $LaNiO_3/SrTiO_3$ (111)

Fig.4.13 illustrates the dramatic differences of $LaNiO_3/SrTiO_3$ interfaces depending upon the orientation of the STO substrate. In bulk, $LaNiO_3$ is a paramagnetic metal

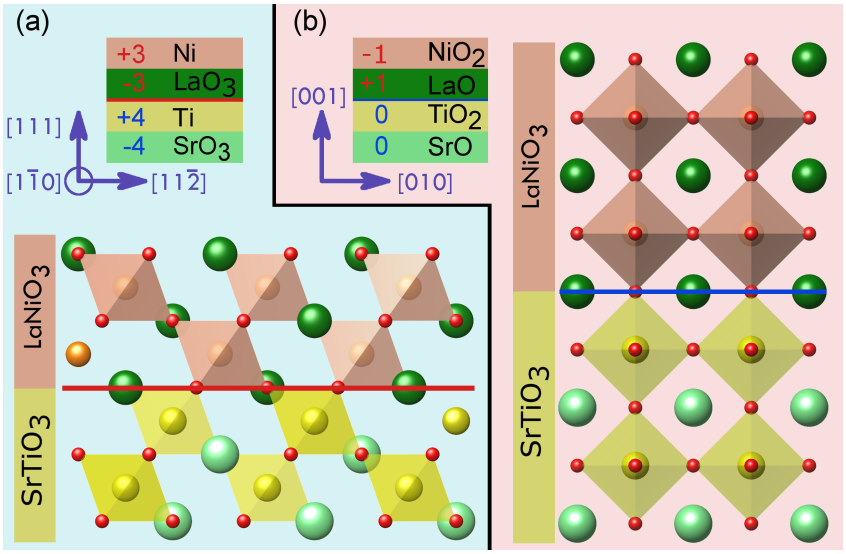

Figure 4.13: Stacking sequence of $LaNiO_3/SrTiO_3$ in (a) [111] and in (b) [001] direction. The structure of $LaNiO_3/SrTiO_3$ in [111] and [001] direction is shown, respectively. It is easily seen that packing factor of [111] direction is considerably larger than [001] direction.

[65], where the nominal oxidation state of Ni is +3, with a low spin $3d^7$ electronic configuration. As shown in Fig.4.13(a) in the [111] direction, the stacking of Ni^{3+} and $(LaO_3)^{3-}$ have in-plane uncompensated charge of 3+ and 3-, which makes [111] direction highly polar. The $SrTiO_3$ (111) substrate is formed by stacking of Ti^{4+} and $(SrO_3)^{4-}$, which exhibits sequential repetition of in-plane net charge of 4+ and 4-, making $SrTiO_3$ even more polar than $LaNiO_3$. The charge imbalance at the interface, between Ti^{4+} and $(LaO_3)^{3-}$ creates a discontinuity in the electric potential, hence a polar discontinuity, which results in divergence of the interface free energy. In [001] direction, as shown in Fig.4.13(b), the substrate does not have uncompensated charge, therefore it is not polar[1]. The (001) interface is considered as weakly polar due to the uncompensated charge on Nickelate side. The interplanar spacing for (111) is about 1.7 times smaller than for [001] direction making the interface region more susceptible to intermixing.

To avoid the divergence of energy at the interface, the interface either severely

[1]Based on nominal charges, this surface is not polar, but as our results showed earlier, it is weakly polar.

intermixes or the thin film grows in another phase, which in the case of $LaNiO_3$ is $La_2Ni_2O_5$ [36]. There have been several attempts to address the polar discontinuity issue [35, 36, 66–69], but producing a single-phase thin film with sharp interface still remains a challenge. In most cases, the first few layers grow in different, unwanted phases to prevent the divergence of surface free energy, usually referred to as polar catastrophe. There are four possible avenues to avoid polar catastrophe: adsorption (contamination), electronic reconstruction, geometrical reconstruction and stoichiometric reconfiguration [27]. Among these, only electronic reconstruction can preserve the phase and structure of thin film at the interface, since the other three will cause interface roughening. A microscopic understanding of the interface dynamics during initial stages of growth is crucial. We show that with a proper processing procedure it is possible to avoid polar catastrophe and obtain a single phase thin film with uniform structure. We show that with a proper processing procedure for substrate and thin film, it is possible to avoid polar catastrophe and obtain a single phase thin film with uniform structure.

High quality thin films of $LaNiO_3/SrTiO_3$ (111) are grown using UHV pulsed laser deposition. The growth was monitored by high pressure reflection high energy electron diffraction (RHEED). The substrate was prepared using a special method described above. Laser pulses of 180 mJ at repetition rate of 10 Hz were focused on stoichiometric $LaNiO_3$ target. During the growth, the substrate was at 625 °C and the 6% oxygen/ozone mixture with partial pressure of 10 mTorr. The thickness of the thin films was determined by RHEED oscillations, shown in Fig.(a). The streak like RHEED pattern in the end of growth shows a two dimensional (2D) thin film growth (inset Fig.4.14(a)). Clear RHEED oscillations are a direct indication of crystalline thin film growth, but they do not provide information about the phase or structure of thin film in the growth direction, especially near the buried interface. The samples grown for in situ measurements such as, angle-resolved X-ray photoemission spectroscopy (ARXPS), low

energy electron diffraction (LEED) and RHEED, were grown on 0.1% Nb-doped SrTiO3 (111) to achieve conductivity. The samples used for ex-situ high resolution transmission electron microscopy (STEM) measurement were grown on both doped and non-doped SrTiO3 (111).

Fig.4.14(b) displays high-angle annular dark field (HAADF) STEM image of our $LaNiO_3/SrTiO_3$ (111) interface taken along $[1\bar{1}0]$ direction, showing a sharp interface and extremely well ordered epitaxial film. The thin film is fully strained and no obvious interface roughening is observed. The substrate is Ti terminated and the thin film growth begins with the LaO_3 layer. Fig.4.14(c) shows the elemental electron energy loss spectroscopy (EELS) mapping, providing the chemical composition of the interface. The line profiles of EELS mapping indicate that the interface intermixing is limited to the two unit cells, particularly at transition metal ion site (B-site). The intermixture between Ti and Ni based on the variation of Ti EELS intensity is about 50% and 20% in the first and second unit cell, respectively. Fig.4.16(a) shows the EELS spectra of Ti $L_{2,3}$ edges across the $LaNiO_3/SrTiO_3$ (111) interface that was used to determine the Ti valence. It should be noticed that the L_3 and L_2 edges shift towards to lower energy at the interface and in the $LaNiO_3$ layers. The shift of Ti L-edge has been used to determine the oxidation state using two reference materials $SrTiO_3$ (Ti^{4+}) to $LaTiO_3$(Ti^{3+}) [70, 71]. Notice that there is ∼1.2 eV shift between the two L edges in the two reference materials. The energy shift of L_3 and L_2 e_g peaks are plotted in Fig. S1 (b), the oxidation state of Ti can be estimated by assuming a linear relationship between the Ti valence state and the energy shift of Ti L edge [70, 72]. Notice that the shift is only ∼0.2 eV, small compared to the ∼ 1.2 eV shift between Ti^{4+} and Ti^{3+}. The multiplet structure seen on the L_3 and L_2 edges for Ti^{4+} spectra disappears or broadens in the Ti^{3+} spectra due to changes in the t_{2g} state [73]. Our analysis from Ti EELS spectra shows there is a slight variation of chemical valence of Ti ions diffusing in the

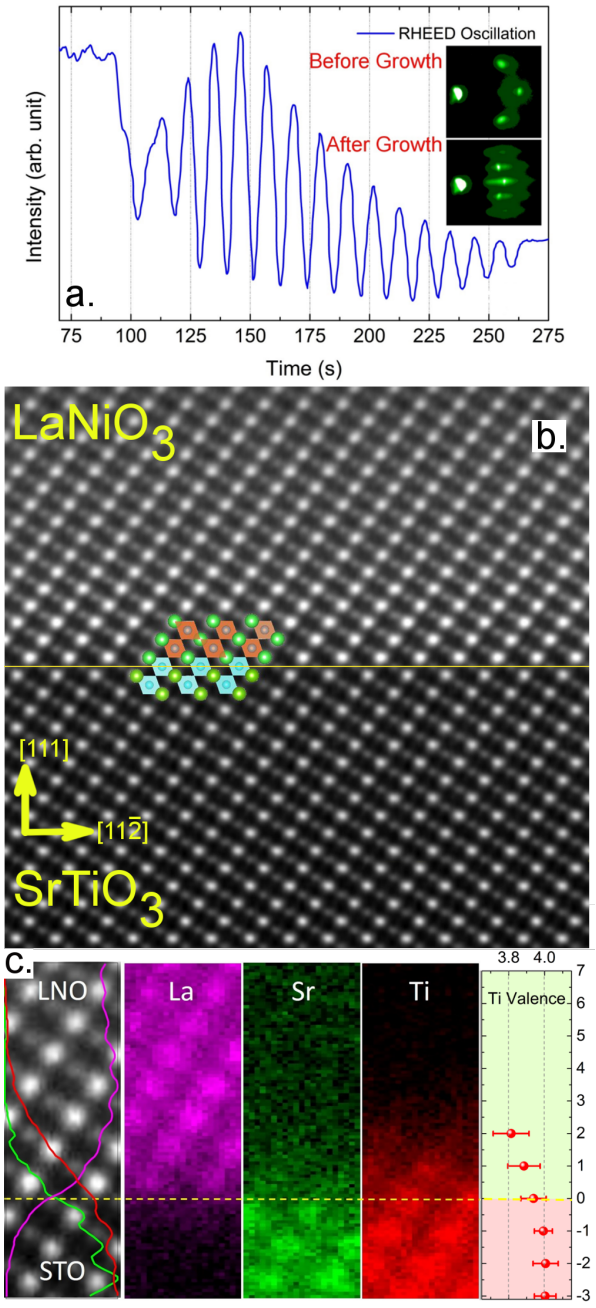

Figure 4.14: RHEED oscillations for $LaNiO_3/SrTiO_3$ (111) is presented for 15 u.c. The inset shows the RHEED pattern before and after growth. The streak-like pattern after growth is an indication of 2D growth mode. b) HAADF-STEM image of $LaNiO_3/SrTiO_3$ (111) along $[1\bar{1}0]$ direction. The interface is marked by the yellow line and the ball model mapped on the image shows the schematic of $LaNiO_3/SrTiO_3$ (111). c) The EELS elemental mapping and line profiles for Ti, Sr and La. The change in the formal valence of Ti is shown across the interface.

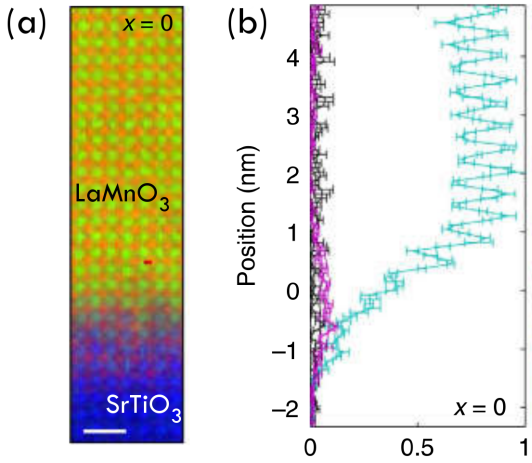

Figure 4.15: a) EELS map of $LaMnO_3/SrTiO_3(001)$. Ti is blue, Mn is green and La is red. b) The concentration of Mn^{2+}, Mn^{3+} and $Mn^{3.5+}$ is magenta, cyan and black. The figure is reproduced from [8].

$LaNiO_3$ film. The valence state of Ti reduces from +4 in $SrTiO_3$ to $\sim$+3.8 in the first and second unit cell of the film. Although the inter-diffusion Ti into $LaNiO_3$ is not large, the Ti plays an important role in compensating structural and polar mismatch at the interface. The role of Ti here is twofold. First the larger Ti ionic radius can alleviate the tensile stress at the interface. Second, the partially occupied d-orbital of Ti at $LaNiO_3$ side will help screen the uncompensated charges at the interface. The two-unit cell inter-diffusion in [111] direction is about 0.44 nm which translates to about 1.2 LaNiO3 unit cell in [001] direction. Considering atomic packing factor in [111] direction, this means that the $LaNiO_3$ (111) thin film has a sharp interface.

The Ni EELS spectra was not possible to recorded because the cross section of Ni 2p core level is very low and requires an intense electron beam, also, the presence of large La 3d core level near Ni 2p core level further smears out the Ni 2p signal. Increasing the beam intensity damages the sample. We have investigated the Ni oxidation state using ARXPS in the following.

In order to understand the evolution of the surface structure of thin films, the surface of 3 and 5 unit cell (uc) $LaNiO_3$ (111) was studied using LEED, performed in-situ

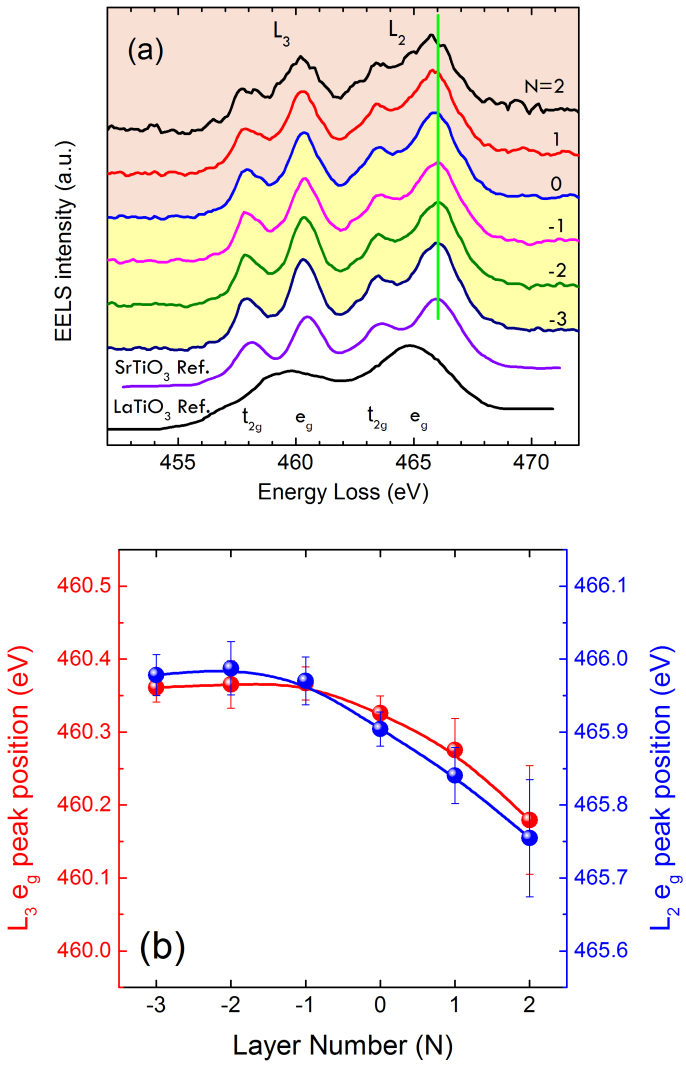

Figure 4.16: Oxidation state of Ti ions for the $LaNiO_3/SrTiO_3$ film. (a) Background subtracted EELS spectra of Ti L edges across the $LaNiO_3/SrTiO_3$ interface layer. The terminated Ti layer was set as N=0. (b) The energy position of Ti L_3 (red) and L_2 (blue) e_g peaks.

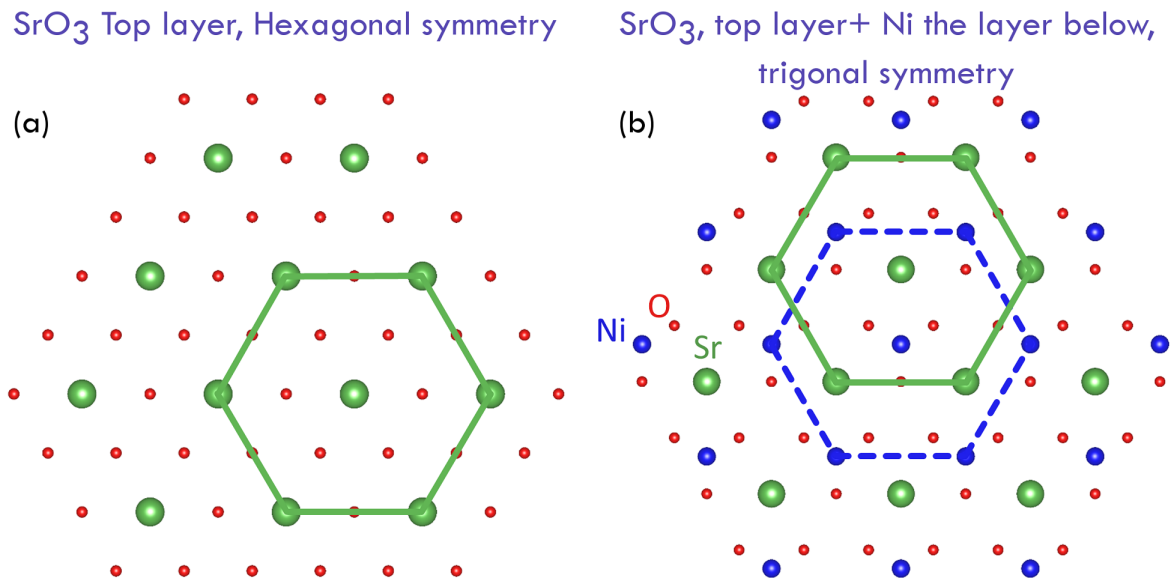

Figure 4.17: Surface of $LaNiO_3$ (111). (a) The top layer, SrO_3, has hexagonal symmetry, but the unit cell with the second layer included, has trigonal symmetry (b), resulting in a three-fold LEED pattern, without multi-domain structure.

immediately after growth. Figures 4.18(a) and (b) show the LEED patterns for these two thin films. The sharp LEED spots confirm that the surface is well ordered. Both images exhibit three-fold symmetry, following the symmetry of the substrate and the symmetry expected for the epitaxial film. As shown in Fig.4.17, the SrO_3 top layer has hexagonal symmetry (six-fold). Considering the the second layer, Ni, the symmetry reduces to three-fold which is what is seen in the LEED pattern.

The desired phase is $LaNiO_3$, but a previous study observed $La_2Ni_2O_5$ [36] phase near the interface as an intermediate phase during the growth. The difference between $LaNiO_3$ and $La_2Ni_2O_5$ is the ordered oxygen vacancy rows, as shown in Fig.4.18(c) and (d). The $La_2Ni_2O_5$ surface should result in a 2×1 reconstruction. The expected LEED patterns for each phase are shown in the insets of Fig. 4.18(c) and (d). If the $La_2Ni_2O_5$ phase were present, the fractional spots would have been present at the positions of the red circles in Fig. 4.18(a) and (b). The absence of fractional spots means that the film has the symmetry of bulk, i.e. not $La_2Ni_2O_5$. This observation indicates that polarity

compensation does not drive the thin film into a new phase with reconstructed surface for our growth conditions.

Ordered rows of oxygen vacancy distinguish $La_2Ni_2O_5$ from $LaNiO_3$. Since the Oxygen is a light element, we performed annular bright field (ABF) STEM imaging, which is sensitive to light elements. Figure 4.19(a) is the ABF-STEM image of the $LaNiO_3/SrTiO_3$ interface for a 16uc $LaNiO_3$ thin film. The Fast Fourier transform (FFT) of the ABF STEM image of the $LaNiO_3$ film is shown in Fig. 4.19(b). This diffraction pattern can be compared to what would be expected for the two different phases, $La_2Ni_2O_5$ or $LaNiO_3$. Fig. 4.19(c) and (d) are marble models of the two different structures projected along $1\bar{1}0$]. The insets in the Fig. 4.19(c) and (d) show simulated electron diffraction pattern of the ideal structure. Presence of ordered rows of Oxygen vacancies for the $La_2Ni_2O_5$ structure (Fig. 4.19(d)) results in the presence of fractional order spots. The red circles in Fig. 4.19 indicate the position where the fractional order spots should appear, but the spots are missing. The advantage of this method is that one can take Fourier transform of different areas of the thin film to see if there are patches of $La_2Ni_2O_5$ co-existing with $LaNiO_3$ phase, which was never observed.

We utilized XPS to study the oxidation states of Ni for four film thicknesses (5, 7, 9 and 16 uc). Figure 4.20 a-d displays the data for the Ni 3p core level spectra at normal emission for different thicknesses. Normal emission was chosen to maximize the depth sensitivity of XPS. The spectra were fitted to four Gaussian-Lorentzian peaks, which represent two oxidation states of Ni (3+ and 2+) and two spin-orbit components of each oxidation state (1/2 and 3/2) [23]. To minimize the number of free parameters used in the fitting and increase the reliability of results, the branching ratio (1:2), spin-orbit splitting energy (2 eV) [74], and FWHM of the peaks were held constant. Fig. 4.20(e) illustrates that with increasing thickness, the ratio of Ni^{3+}/Ni^{2+} peak intensity increases (blue curve). Using this ratio, we can calculate the nominal amount of oxygen vacancies

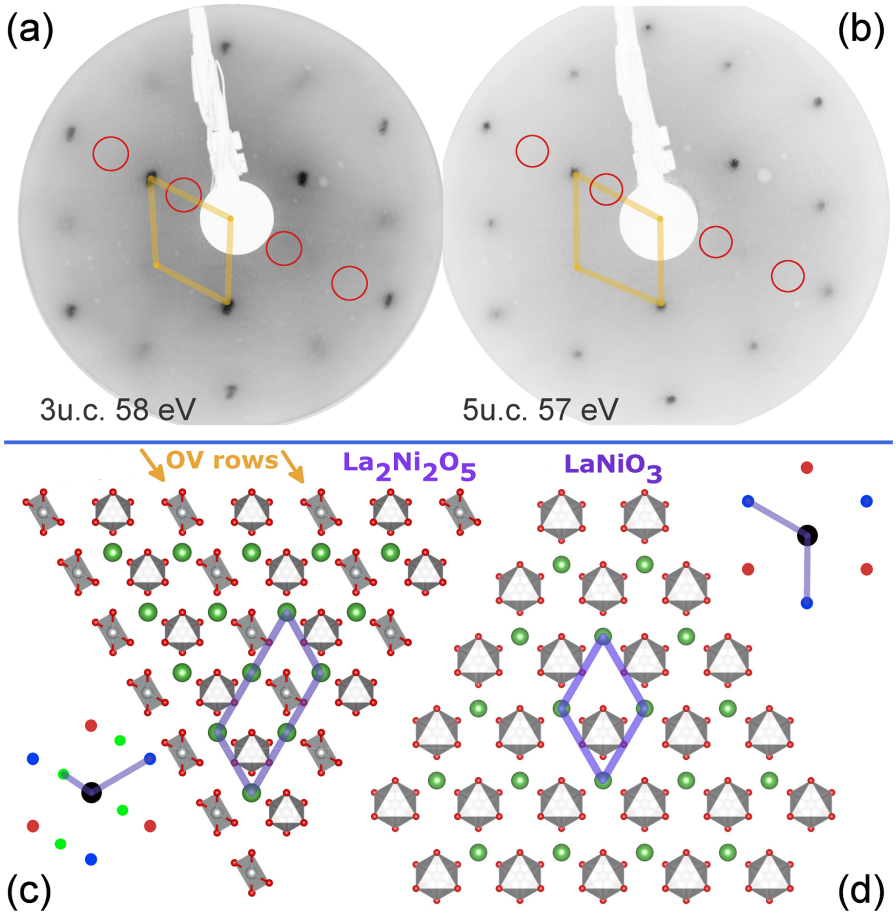

Figure 4.18: a-b) LEED pattern of 3 and 5 uc $LaNiO_3$ (111) thin films. Red circles show the position of fractional spots which would be associated with a $La_2Ni_2O_5$ surface. c) Surface of $La_2Ni_2O_5$ (111). The rows of Oxygen vacancies are shown with yellow arrow. The simulated LEED pattern for this surface is shown. d) Surface of $LaNiO_3$ (111). The simulated LEED patterns are shown next to each structure. For simulated LEED patterns, green spots are fractional. Red and blue spots are integer, each color accounting for a domain.

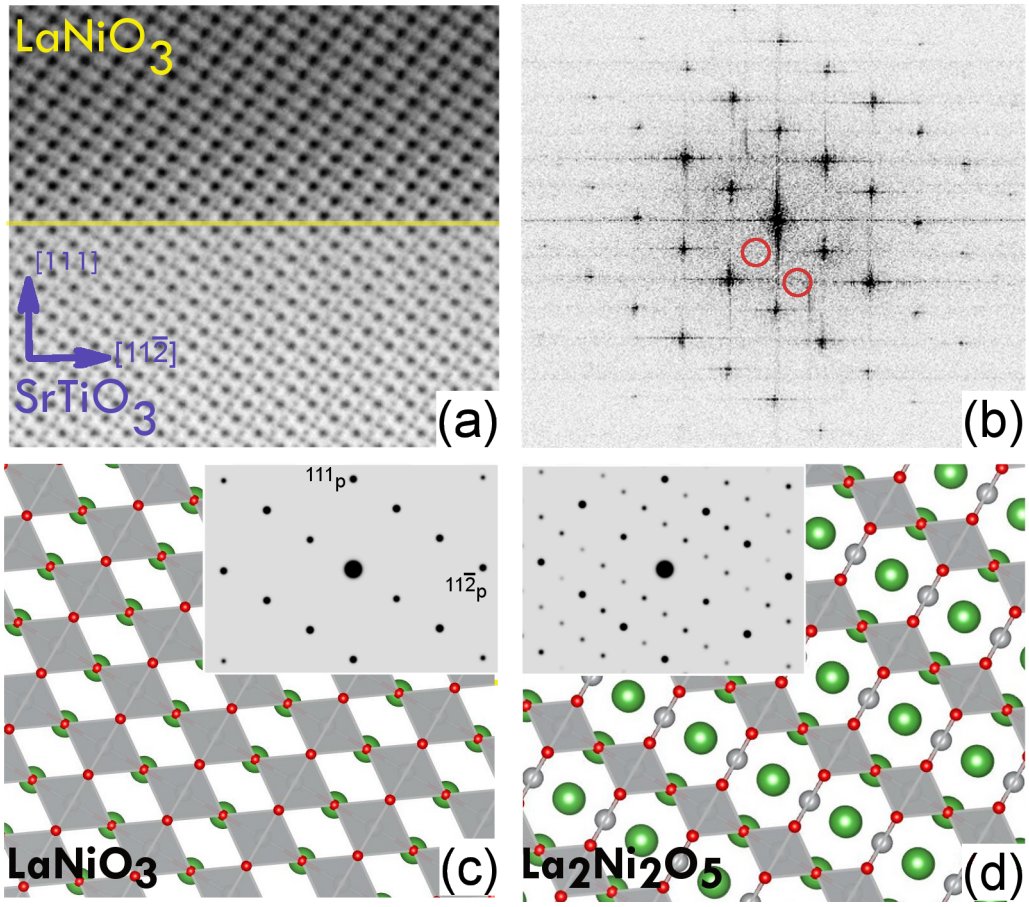

Figure 4.19: a) ABF-STEM image of 16 uc $LaNiO_3/SrTiO_3$ (111) along $[1\bar{1}0]$ direction. The interface is marked by the yellow line. b) Fast Fourier Transform (FFT) of the ABF-STEM image. Red circles indicate the position of fractional spots for $La_2Ni_2O_5$ phase. Absence of fractional spots in the FFT image indicates no ordered Oxygen vacancy. c-d) Schematic of $LaNiO_3$ and $La_2Ni_2O_5$ projected along $[1\bar{1}0]$. The simulated electron diffraction patterns are shown in the inset, respectively. The Fourier transform of $La_2Ni_2O_5$ shows fractional spots which are absent in $LaNiO_3$.

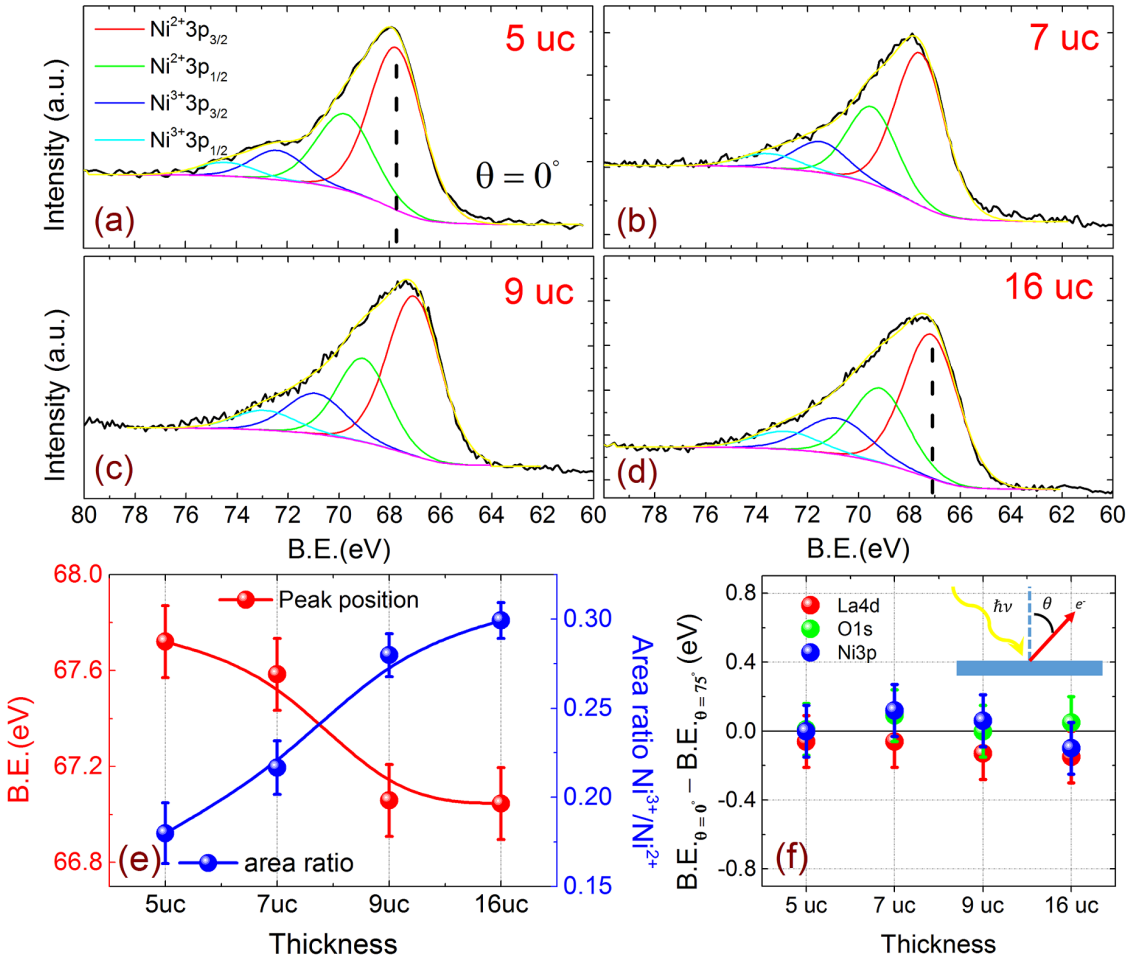

Figure 4.20: a-d) XPS spectra of Ni 3p for different thicknesses at normal emission. e) (Left) Change in binding energy of Ni 3p core level as a function of thickness and (Right) Change in area ratio of Ni^{3+}/Ni^{2+} for Ni 3p core level. f) The difference in binding energy of La 4d, O 1s and Ni 3p in normal emission and $\theta = 75°$. The inset shows the schematic angle dependent XPS.

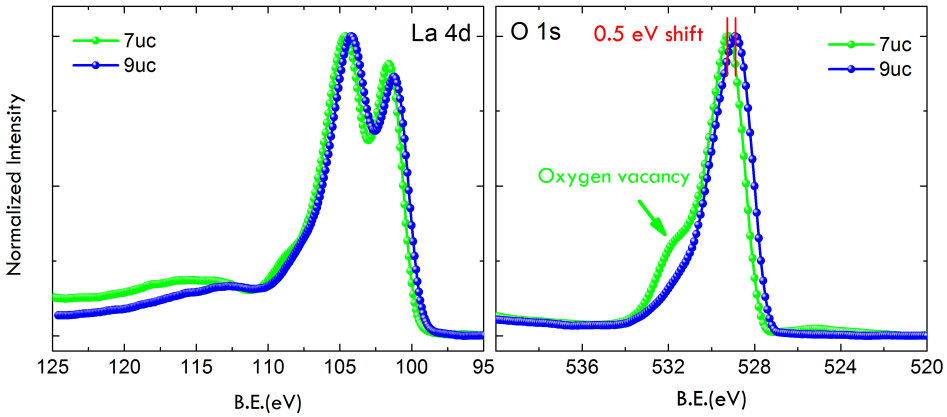

Figure 4.21: The XPS spectra of La 4d and O1s at normal emission. The shift is seen upon going from 7 uc to 9uc which is due to final state effect that means the core hole screening increases.

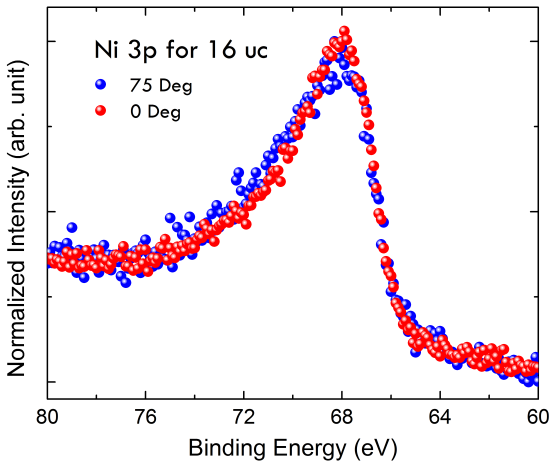

Figure 4.22: XPS spectra of Ni 3p at normal angle and $\theta = 75°$. The line shape of two spectra are the same and there is no apparent shift in the binding energy.

by fixing the stoichiometry according to formula $LaNiO_x$. The resulting x equals are 2.55, 2.61, 2.63 and 2.65 for 5, 7, 9 and 16 uc thick films, respectively. The calculated oxygen content of thin films based on our XPS results approaches the oxygen content of $La_2Ni_2O_5$ (x = 2.5) with decreasing film thickness, but there is no indication of the existence of $La_2Ni_2O_5$ phase in the HAADF-STEM results. The binding energy of the Ni 3p core level, shown in Fig. 4.20(e) appears to exhibit a sudden shift to lower energy for films thicker than 7 uc. The same behavior was observed in the O 1s and La 4d core levels (Fig.4.21). This means the core hole screening increases for thicknesses above 7 uc. The enhanced core hole screening is an indication of enhanced metallicity [75]. This is consistent with the fact that with increasing the thickness, the amount of oxygen vacancies decrease which restores the metallicity of $LaNiO_3$, and agrees with the previous work where it was shown that with increasing thickness the metallicity of the thin film increases [36].

In order to resolve the puzzle of the thickness-dependent oxygen content vs. no structural change, it is important to know the distribution of the oxygen vacancies. Are they uniform throughout the thin film or are they concentrated near the interface? We have performed large angle XPS to enhance the surface sensitivity. Fig. 4.20(f) shows that there is no measurable difference between binding energy of O 1s, Ni 3p and La 4d core levels at normal emission compared to $\theta = 75^\circ$ emission angle. If the chemical environment of O, Ni and La in the film differed from the region near the surface, then the initial state effect would cause a core level shift for these elements. The line shape of Ni 3p spectra for normal emission and $\theta = 75^\circ$ are identical (Fig.4.22). This result is consistent with elemental EELS analysis from STEM where no appreciable change was observed in the line shape and energy of EELS spectra of O K-edge.

4.5 Summary

In this chapter, the effect of polarity, weak and strong, on the surface of $SrTiO_3$ in [001] and [111], as well as interface of $LaNiO_3/SrTiO_3$ (111) studied. In the case of $SrTiO_3$ (001), our data show that although the nominal charges at the TiO_2 termination is zero, meaning the surface does not bear any net charge, the surface is weakly polar. Our LEED I-V data shows rumpling of atoms at and near the surface. The surface of $SrTiO_3$ (111) which is strongly polar was studied. We presented the data that shows the surface behavior as a function of temperature. We specifically studied the surface to understand its behavior at the growth condition. The result of this part showed a narrow temperature range that gives optimal surface condition for the thin film growth. In the third portion of this chapter, we took advantage our findings about $SrTiO_3$ (111) surface to grow $LaNiO_3$ (111) thin films. We successfully created a single-phase thin film with atomically sharp interface. Our work showed that it is possible to control interface polarity and maintain a well-ordered structure at the interface.

Chapter 5
Magnetic orders and interactions

There different types of interaction responsible for magnetic property of a material. Some are weak, like diamagnetism and paramagnetism (PM) and some are strong like Anti-Ferromagnetism (AFM) and Ferromagnetism (FM). They can be weak such as diamagnetism and paramagnetism or strong like exchange interactions.

5.1 Magnetic orders

There are different types of magnetic phases. In this section they are briefly mentioned and in the rest of the chapter their property will be explained in greater details.

5.1.1 Diamagnetism

The orbital motion of electrons creates tiny atomic current loops, which produce magnetic fields. When an external magnetic field is applied to a material, these current loops will tend to align in such a way as to oppose the applied field. This may be viewed as an atomic version of Lenz's law: induced magnetic fields tend to oppose the change which created them. Materials in which this effect is the only magnetic response are called diamagnetic. All materials are inherently diamagnetic, but if the atoms have some net magnetic moment as in paramagnetic materials, or if there is long-range ordering of atomic magnetic moments as in ferromagnetic materials, these stronger effects are always dominant. Diamagnetism is the residual magnetic behavior when materials are neither paramagnetic nor ferromagnetic.

Any conductor will show a strong diamagnetic effect in the presence of changing magnetic fields because circulating currents will be generated in the conductor to oppose the magnetic field changes. A superconductor will be a perfect diamagnet since there is no resistance to the forming of the current loops.

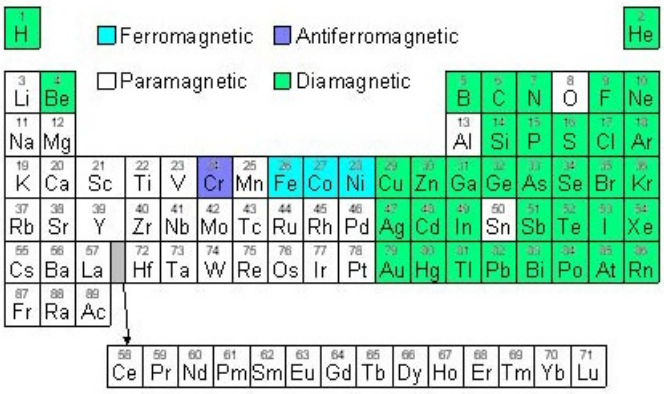

Figure 5.1: Periodic table of magnetic properties of atoms.

Recalling classical electrodynamics, the diamagnetic susceptibility is much larger if the magnetic field is applied perpendicular to the layers than if it is applied in the parallel direction. One example is graphite which has a layered structure [76]. The susceptibility of diamagnets is negative (hall mark of superconductors).

5.1.2 Paramagnetism

Some materials exhibit a magnetization which is proportional to the applied magnetic field in which the material is placed. These materials are said to be paramagnetic and follow Curie's law[1]. All atoms have inherent sources of magnetism because electron spin contributes a magnetic moment and electron orbits act as current loops which produce a magnetic field. In most materials the magnetic moments of the electrons cancel, but in materials which are classified as paramagnetic, the cancelation is incomplete.In another word, they have unpaired electrons. This means atoms with full shell do not have paramagnetism, like noble gases. While atoms with incomplete shells show paramagnetism, like Na, Mg and Al.

The magnetic moment on an atom is associated with its total angular momentum **J** which is a sum of the orbital angular momentum **L** and the spin angular momentum **S**,

[1]Pierre Curie (1859-1906).

$$\mathbf{J} = \mathbf{L} + \mathbf{S} \tag{5.1}$$

There is a special case where $\mathbf{J} = 0$. In this case one would expect that there is no paramagnetism and the system is diamagnetic, which is correct only to first order perturbation theory. Second order perturbation theory which considers the excited states where $\mathbf{J} \neq 0$, therefore there is a positive contribution to the susceptibility that surpasses the negative contribution (coming from diamagnetism) which results in a net positive susceptibility and hence a paramagnet. This is called **van Vleck**[1] paramagnetism which is, like diamagnetism, both small and temperature independent.

5.1.3 Ferromagnetism

Ferromagnetic materials exhibit a long-range ordering phenomenon at the atomic level which causes the unpaired electron spins to line up parallel with each other in a region called a domain as shown in Fig5.2 and Fig5.3. Within the domain, the magnetic field is intense, but in a bulk sample the material will usually be unmagnetized because the many domains will themselves be randomly oriented with respect to one another. Ferromagnetism manifests itself in the fact that a small externally imposed magnetic field, say from a solenoid, can cause the magnetic domains to line up with each other and the material is said to be magnetized. The driving magnetic field will then be increased by a large factor which is usually expressed as a relative permeability for the material. There are many practical applications of ferromagnetic materials, such as the electromagnet.

The long range order which creates magnetic domains in ferromagnetic materials arises from a quantum mechanical interaction at the atomic level. This interaction is remarkable in that it locks the magnetic moments of neighboring atoms into a rigid

[1] John H. van Vleck (1899-1980). 1977 Nobel prize for his contribution to the understanding of the behavior of electrons in magnetic solids. He shared his prize with P. W. Anderson and N. F. Mott.

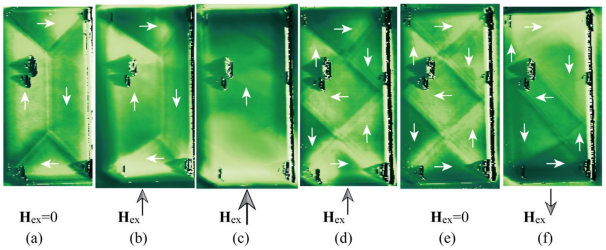

Figure 5.2: MFM images as a function of applied field for the $5\mu m \times 10\mu m$ region of single crystal Fe film. The arrows on the images represent the magnetization vector directions of the domains. The arrows below the images refer to the directions of the applied magnetic field. (a) initial domain structure before applying any field; (b) the applied filed was 600G. (c) at the maximum of the applied field 2000G. (d) at the moment when the applied field reduced to 200G from the maximum. (e) when the applied field reduced to zero; (f) at the moment when the applied field increased 1000G from zero at an opposite direction [9].

parallel order over a large number of atoms in spite of the thermal agitation which tends to randomize any atomic-level order. Sizes of domains range from a 0.1 mm to a few mm. When an external magnetic field is applied, the domains already aligned in the direction of this field grow at the expense of their neighbors. If all the spins were aligned in a piece of iron, the field would be about 2.1 Tesla. A magnetic field of about 1 T can be produced in annealed iron with an external field of about 0.0002 T, a multiplication of the external field by a factor of 5000! For a given ferromagnetic material the long range order abruptly disappears at a certain temperature which is called the Curie temperature for the material. The Curie temperature of iron is about 1043 K. The Curie temperature gives an idea of the amount of energy takes to break up the long-range ordering in the material. At 1043 K the thermal energy is about 0.09 eV compared to about 0.025 eV at room temperature.

5.1.4 Anti-Ferromagnetism

In materials that exhibit antiferromagnetism as shown in Fig.5.3, the magnetic moments, usually related to the spins of electrons, align in a regular pattern with neighboring spins (on different sublattices) pointing in opposite directions. This is, like

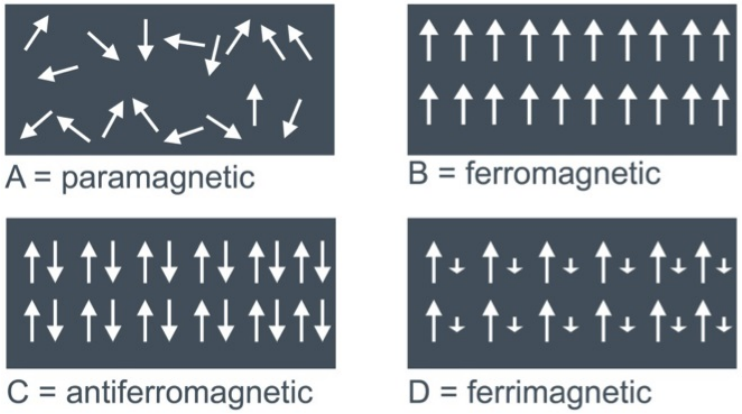

Figure 5.3: The moment ordering in different magnetic phases are shown.

ferromagnetism and ferrimagnetism, a manifestation of ordered magnetism. Generally, antiferromagnetic order may exist at sufficiently low temperatures, vanishing at and above a certain temperature, the Néel temperature[1]. Above the Neel temperature, the material is typically paramagnetic. AFMs can be thought of two inter penetrated FM sublattices. The order is due to exchange interaction.

When no external field is applied, the antiferromagnetic structure corresponds to a vanishing total magnetization. In an external magnetic field, a kind of ferrimagnetic[2] behavior may be displayed in the antiferromagnetic phase, with the absolute value of one of the sublattice magnetizations differing from that of the other sublattice, resulting in a nonzero net magnetization. Although the net magnetization should be zero at a temperature of absolute zero, the effect of spin canting often causes a small net magnetization to develop, as seen for example in hematite (Fe_2O_3).

One of the complications of AFMs is that there is a large number ways of arranging an equal number of up and down spins on a lattice. The different arrangements of spins depend on the kind of crystal lattice on which the spins are sitting. Fig.5.4 shows the different types of AFM in cubic lattices. For example in cubic perovskite, G-type

[1]Louis Eugene Felix Neel (1904-2000). 1970 Nobel Prize in physics for pioneering studies of the magnetic properties of solids. Clifford Shull in 1949 confirmed the AFM order using Neutron scattering and won the 1994 Nobel prize in Physics.

[2]Spin up and down have different sizes.

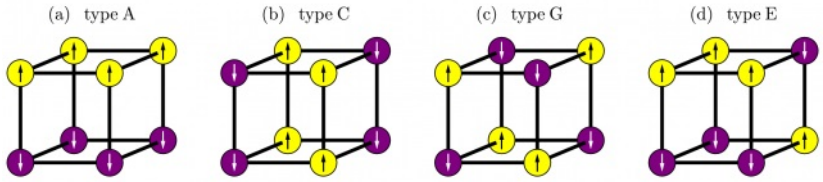

Figure 5.4: Different types of AFM order on cubic lattice are shown.

AFM is very common since superexchange interactions through oxygen ligands will force all neighboring spins to be anti parallel, $LaFeO_3$ and $SrMnO_3$ are two examples. Interestingly, this is not the case all perovskites, for example $LaMnO_3$ shows A-type order which is due to Jahn-Teller distortion of octahedra. This will be discussed more later.

5.1.5 Ferrimagnetism

For AFMs the spin size of spin up and spin down sublattices are equal. But if the two sublattices differ in size then the magnetization of them will not be equal and the net magnetization will not cancel out, as it is shown in Fig.5.3. The material will then have a net magnetization. This phenomenon is known as Ferrimagnetism. Since the molecular field of each sublattice is different, the spontaneous magnetization of the sublattices will in general be different and may have different temperature dependence. Therefore the net magnetization can have a complicated temperature dependence. Therefore at low temperature one sublattice will dominate and at higher temperature the other. This means that the net magnetization can change sign as a function of temperature. The magnetization reversal temperature is called compensation temperature. Therefore the magnetic susceptibility of ferrimagnets does not follow Curie law.

Ferrites are a family of ferrimagnets. Thier chemical formula is $M\dot{F}e_2O_3$ where M is a divalent transition metal. The crystal structure is the spinel structure which contains two types of lattice sites, octahera (B-sites, here Fe) and tetrahedra (A-sites, here M). In invers spinels M cations sit at half of B sites while Fe^{3+} cations occupy the other half

of the B sites and all the A sites. In inverse spinels, the moments of the Fe^{3+} cations on the A and B sites are antiparallel so the total moment of the sample is due to the M^{2+}.

Most of Ferrimagnets are insulators which makes them practical for applications.

5.1.6 Spin glass

Spin glass is defined as a random magnetic system[1] with mixed interaction characterized by a random, cooperative, freezing of spins at a well defined temperature T_f (freezing temperature). Below freezing temperature a metastable frozen state appears without the usual magnetic long rang ordering. The absence of long range ordering and randomness in spin orientation is the reason for the term "glass".

Spin glass systems are frustrated. This is means it is not possible to satisfy all the interactions in the system to find the ground state. Therefore in the spin glass there is no unique ground state, but there is variety of similar low energy states (too many close local minima in Free energy and no global minima). The system therefore cannot achieve a state that entirely satisfies its microscopic constraints, but does possess a multiplicity of equally unsatisfied states. As a result the frustrated system shows metastability, hysteresis effects (dependence on the sample's magnetic or thermal history), and time-dependent relaxation towards equilibrium.

One famous example of frustration in glassy systems is geometric frustration. In two dimension, Heisenberg spins[2] on a triangular Kagomé lattice. Fig.5.5a shows the frustration in a simple triangular lattice with AFM nearest neighbor interaction. The spin on the third corner cannot satisfy the AFM interaction with both of its neighbors, hence it is frustrated. Fig.5.5b-c show two degenerate spin configuration on a Kagomé lattice. Therefore again the system cannot find a unique ground state. The three di-

[1]There are several types of randomness that can create a spin glass, like, site-randomness in diluted magnetic semiconductors, bond-randomness where the moment interaction (exchange) with nearest neighbor changes, amorphous magnets with random anisotropy (there is locally varing 'easy axis' for the manentization).

[2]Heisenberg spins can point to any direction while Ising spin only point up and down.

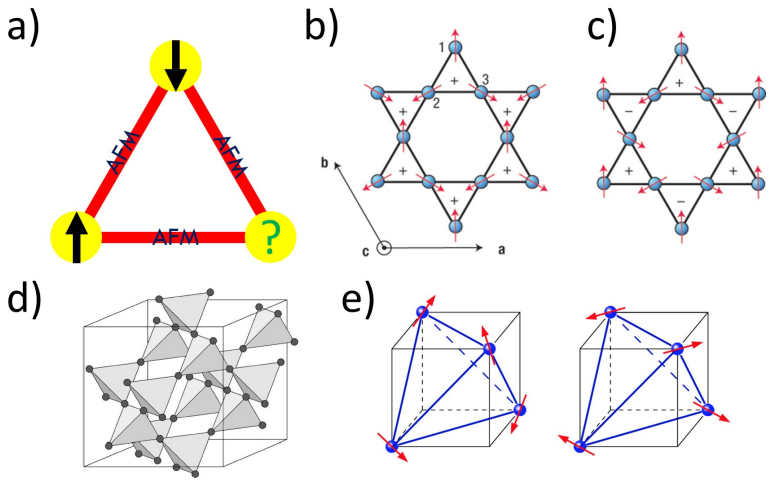

Figure 5.5: a) Ising spins on a triangular lattice with AFM order. The third spin is frustrated. b-c) Heisenberg spin on a Kagomé lattice. The two configuration are degenerate, hence the system does not have a unique ground state. d) pyrochlore structure and corner sharing tetrahedra are shown. e) Spins are frustrated on the corner of tetrahedra.

mensional example of frustrated system is pyrochlore structure (Fig.5.5) where magnetic ions occupy a lattice of corner sharing tetrahedra. These systems are believed not to order but to display a classical ground state with macroscopic degeneracy, sometimes described as cooperative paramagnetism in which only short-range correlations between spins are found for all temperatures. Some of these systems are also believed to possess a dispersionless spin-wave branch, known as a zero mode, which strongly affects the low temperature thermodynamic behaviour and leads to the persistence of spin fluctuations down to zero temperature.

5.1.7 Superparamagnetism

In ferromagnents there are a lot of large domains present where they interact. Now if a material is made of very small non-interacting domains (which are sometimes called particles[1]), then it is called Superparamagnet. Why not super Ferromagnet? because there is no hysteresis in superparamagnets. Why not just paramagnets? because the

[1]These particles are consist of several individual moment that are interacting ferromagnetically.

response to external magnetic field (susceptibility) is very large, hence super. At high temperatures the moments on the particles are able to fluctuate rapidly and as the temperature goes down the fluctuation slow down. At very low temperature, the system appears to be static. The temperature at which the system becomes static is called blocking temperature T_B.

Superparamagnets have some similarities with spin glasses but are quite different in a number of respects: the interactions between the magnetic particles are not important in a superparamagnet, whereas they are vital in a spin glass; also, the spin glass shows a cooperative phase transition while the superparamagnet shows a gradual blocking of the superparamagnetic particles.

5.2 Magnetic interaction

In this section various type of magnetic interaction will be discussed which can be important in allowing the magnetic moment go under different types of order. The occurrence of magnetic ordering in crystals implies some coupling mechanism between localized or delocalized magnetic moments. Among microscopic models of coupling between the localized moments, I focus on the Heisenberg model which is related to exchange interaction between two electrons on neighboring lattice sites. The exchange interaction is purely due to the electrostatic coupling of two electrons which naively may seem odd to create magnetic ordering. Intuitively, the first interaction that comes to mind for spin ordering is dipolar interaction of two local moments (spins). Therefore I briefly go over dipolar interaction and then I will focus on exchange interaction.

5.2.1 Dipolar interaction

When two magnetic dipoles μ_1 and μ_2 are separated by $\mathbf{r}$, their energy is:

$$E = \frac{\mu_0}{4\pi r^3}\left[\mu_{\mathbf{1}} \cdot \mu_{\mathbf{2}} - \frac{3}{r^2}(\mu_{\mathbf{1}} \cdot \mathbf{r})(\mu_{\mathbf{2}} \cdot \mathbf{r})\right] \tag{5.2}$$

With some approximation one can estimate the energy of this interactions. Atomic

magnetic moments have the magnitude of Bohr[1] magneton, which is $\mu_1 \approx \mu_2 \approx g\mu_B \approx {}^{e\hbar}/_{mc}$. Therefore the size of energy is about;

$$E \approx \frac{(g\mu_B)^2}{r^3} \approx \frac{1}{137^2}\left(\frac{a_0}{r}\right) \quad \text{Ry} \tag{5.3}$$

In a magnetic solid the interatomic distance is about 2Å so the energy of dipolar interaction is about 0.1 meV which is very small comparing to room temperature energy and corresponds to 1 Kelvin. This is very small energy scale, comparing with energy scale of interaction responsible for ferromagnetism in Cobalt with $\mathrm{T_C} = 1394K$ one can see that magnetic dipole interaction cannot be responsible for long range magnetic order in solids.

5.2.2 Hund's rules

Before moving to interaction between electron on two different sites in a solid, it is important to understand how the moments on a single atom will align. The alignment should be in a way to minimize the energy. The combination of angular momentum quantum number which are found to minimize the energy can be estimated using Hund's rules[2]. These three empirical rules are listed here in descending order of energetic importance, meaning one should attempt to satisfy the first rule and make the way up;

1. Maximize **S**, which is the total spin. This way the Coulomb[3] energy is minimized, since Pauli[4] exclusion principle prevents electrons to stay in the same place, therefore reducing electrostatic Coulomb energy.

2. Maximize **L**, which is the orbital angular momentum. This also reduces the electro-

[1]Niels Henrik Bohr 1885-1962. 1922 Nobel prize in physics for "his services in the investigation of the structure of atoms and of the radiation emanating from them".

[2]Friedrich Hermann Hund 1896-1997.

[3]Charles-Augustin de Coulomb 1736-1806.

[4]Wolfgnag Ernst Pauli 1900-1958. 1945 Nobel prize in physics for his "decisive contribution through his discovery of a new law of Nature, the exclusion principle or Pauli principle". Albert Einstein nominated him for Nobel prize.

static Coulomb energy. Electrons orbiting in the same direction tend to encounter eachother less hence the repulsive Coulomb energy will be less.

3. The third rule concerns **J**, total angular momentum, that depends on whether the shell is less or more than full. For less than half full, $J = |L - S|$ and for more than half full $J = |L + S|$. This rule tries to minimize spin-orbit energy. Third rule does not always work. Transition metals are examples of such circumstances. In transition metal the crystal field splitting overshadows the effect of spin orbit interaction. However for rare earth ions the Hund's rule works very good.

Hund's rules lead to a predictin of the ground state but tell us nothing about the exited states or how close they are to the ground state. They therefore allow us to estimate the magnetic moment of an ion assuming that only the ground state is populated.

5.2.3 Exchange interaction

Exchange interaction is the reason behind long range ordering of magnetic materials. The physics behind exchange interaction is rather simple and directly relates to Pauli's exclusion principle which is a manifestation of the antisymmetrization postulate for Fermions. Electrons with the same quantum number cannot be at the same place.

Exchange interaction between two electrons

The concept of exchange was originally derived from the interpretation of emission spectra of atoms with two unpaired electrons such as neutral helium, called He I. One of the classic works on the interpretation of the He spectrum was written by Heisenberg[1] in 1926.

Consider a simple model with just two electron at $\mathbf{r}_1$ and $\mathbf{r}_2$ sitting at two different orbitals, $\psi_a(\mathbf{r}_1)$ and $\psi_b(\mathbf{r}_2)$. The wave function of the electron system then is $\psi_a(\mathbf{r}_1)\psi_b(\mathbf{r}_2)$.

[1]Werner Heisenberg 1901-1976. 1932 Nobel prize for "the creation of quantum mechanics". He is considered one the most successful scientist in terms of mentoring his students. Bloch, Teller, Peierls, Winterberg, Fano and Majorana are among his students.

This product does not satisfy symmetrization postulate, because this wave function does not change sign under commutation of two electrons. Therefore using Slater's[1] determinant we can make the total wave function anti-symmetrized. The total wave function has two parts: spacial and spin and one of them should be anti-symmetric to atain a total anti-symmetric wave function. Singlet state (S = 0) the spin part χ_S is anti-symmetric therefore the orbital part should be symmetric. For the triplet state (S = 1) the spin part χ_T is symmetric therefore the orbital part should be anti-symmetric.

$$\begin{aligned}\Psi_S &= \frac{1}{\sqrt{2}}\left[\psi_a(\mathbf{r}_1)\psi_b(\mathbf{r}_2) + \psi_a(\mathbf{r}_2)\psi_b(\mathbf{r}_1)\right]\chi_S \\ \Psi_T &= \frac{1}{\sqrt{2}}\left[\psi_a(\mathbf{r}_1)\psi_b(\mathbf{r}_2) - \psi_a(\mathbf{r}_2)\psi_b(\mathbf{r}_1)\right]\chi_T\end{aligned} \tag{5.4}$$

Assuming the Himltonian has only kinetic energy and Coulomb electrostatic terms, then the eigen values of singlet and triplet states are;

$$\begin{aligned}E_S &= \int \Psi_S^* \mathbf{H} \Psi_S d\mathbf{r}_1 d\mathbf{r}_2 \\ E_T &= \int \Psi_T^* \mathbf{H} \Psi_T d\mathbf{r}_1 d\mathbf{r}_2\end{aligned} \tag{5.5}$$

Solving the above integral, one can find the difference between two eigen values is,

$$E_S - E_T = 2\int \psi_a^*(\mathbf{r}_1)\psi_b^*(\mathbf{r}_2)\mathbf{H}\psi_a(\mathbf{r}_2)\psi_b(\mathbf{r}_1)d\mathbf{r}_1 d\mathbf{r}_2 \tag{5.6}$$

Eq.5.6 shows how the difference between singlet and triplet states can be parametrized using $\mathbf{S}_1 \cdot \mathbf{S}_2$. For a singlet state $\mathbf{S}_1 \cdot \mathbf{S}_2 = -3/4$ and for a triplet state $\mathbf{S}_1 \cdot \mathbf{S}_2 = 1/4$. Hence the Hamiltonian can be written in the form of an effective Hamiltonian,

$$\mathbf{H} = \frac{1}{4}(E_S + E_T) - (E_S - E_T)\mathbf{S}_1 \cdot \mathbf{S}_2 \tag{5.7}$$

The first term is constant and the second term depends on the spin. Therefore the

[1]John Clark Slater 1900-1976.

Exchange constant or *Exchange integral*, $\mathbf{J}$ can be defined as,

$$\mathbf{J} = \frac{E_S - E_T}{2} = \int \psi_a^*(\mathbf{r}_1)\psi_b^*(\mathbf{r}_2)\mathbf{H}\psi_a(\mathbf{r}_2)\psi_b(\mathbf{r}_1)d\mathbf{r}_1 d\mathbf{r}_2 \tag{5.8}$$

and hence the spin-dependent term in the effective Hamiltonian can be written,

$$\mathbf{H}^{spin} = -2\mathbf{J}\mathbf{S}_1 \cdot \mathbf{S}_2 \tag{5.9}$$

If $\mathbf{J} > 0$ then $E_S > E_T$ and the triplet state is favored (Ferromagnetism). If $\mathbf{J} < 0$ then $E_S < E_T$ and singlet state (S=0) is favored (Anti-Ferromagnetism). This is the Hamiltonian of the Heisenberg model. One can extend Eq.5.9 to a lattice with i and j sites,

$$\mathbf{H}^{spin} = -\sum_{ij} \mathbf{J}_{ij}\mathbf{S}_i \cdot \mathbf{S}_j \tag{5.10}$$

where $\mathbf{J}_{ij}$ is the exchange constant between the i^{th} and j^{th} spins. As is seen, exchange constant is nothing but an integral. The calculation of the exchange integral can be complicated in general, but I here mention some general features. First, if the two electrons are on the same atom, the exchange integral is usually positive. This stabilizes the triplet state and ensures an anti-symmetric spatial state which minimizes the Coulomb repulsion between the two electrons by keeping them apart. This is consistent with Hund's first rule.

When the two electrons are on neighboring atoms, the situation is very different. Any joint state will be a combination of a state centered on one atom and a state centered on the other. It is worth remembering that the energy of a particle in a one-dimensional box of length L is proportional to L^{-2}; this is a kinetic energy and hence demonstrate that there is a large kinetic energy associated with being squeezed into a small box. The electrons therefore can save kinetic energy by forming bonds because this allows

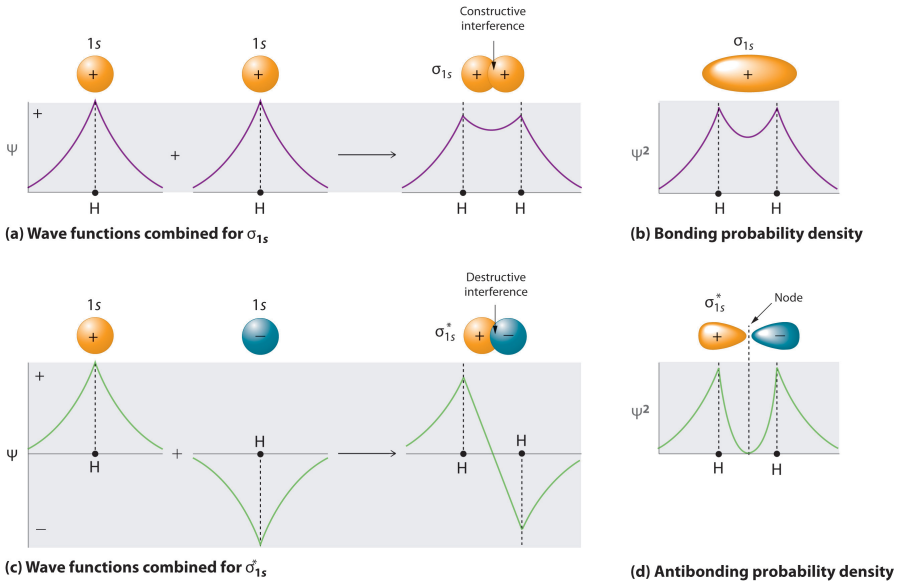

Figure 5.6: a) Wave functions for two Hydrogen atoms form a bond. Since the wave function is spatially symmetric, the spin part should anti-symmetric and singlet. b) Bonding probability, the electrons are distributed between two atoms. c) Anti-bonding which forms an anti-symmetric wave function, therefore triplet state is favored. d) Anti-bonding probability density.

them to wander around both atoms rather than just one, i.e. they spread more. The correct states to consider are now not atomic orbital but molecular orbitals. These can be *boding* (spatially symmetric) or *antibonding* (spatially asymmetric). In the later, the orbital has a greater curvature and hence a larger kinetic energy. This favors singlet states and the exchange integral is therefore likely to be negative. Fig.5.6 illustrates the above points.

It is important to remember that the Hamiltonian did not contain any spin dependent term. The spin dependence was purely from the anti-symmetrized wave function. This section can be summarized as follows.

- The exchange interaction is due to Coulomb interaction and symmetrization postulates.

- If J is positive, the spins are aligned parallel.

- If J is negative, the spins are aligned anti-parallel.

Eq.5.10 represents Heisenberg model which accounts for the exchange interaction by explicitly couplings pairs of spins or atomic moments.

- The coupling energy constant J_{ij} is positive for ferromagnetic coupling, and negative for antiferromagnetic coupling.
- The coupling of individual spins, located on the same atom, is called *intra-atomic* exchange.
- The coupling of atomic moments (sums of spins) on different atoms is called *inter-atomic* exchange.

5.2.4 Direct Exchange

If the electrons on neighboring sites interact via exchange interaction, it is called direct exchange. The reason that is called direct is that there is no intermediate atom between two electrons. Usually direct exchange does not play an important rule in magnetic properties of materials, since there is no sufficient orbital overlap between neighboring sites. In rare earths the 4f electrons are very localized and do not extend to neighboring site and yet they show strong magnetic properties[1]. Therefore, direct exchange cannot be responsible for the strong magnetic properties. The same happens in transition metal oxides. It means there should another type exchange interaction present, *indierect exchange*.

5.2.5 Indirect exchange

It is easy to imagine that exchange can also proceed if the wavefunction on one magnetic atom overlaps with an intermediary wavefunction which in turn overlaps with

[1]Rare earth magnetic field can exceed one tesla. Example is $Nd_2Fe_{14}B$ with magnetic field of 1.4 T.

a wavefunction on another magnetic atom. This situation is referred to as indirect exchange and it comes in three prominent forms, *superexchange*, *double exchange*, and *RKKY exchange*. The first two types are particularly important in transition metal oxides.

Superexchange

The first type of indirect exchange is called superexchange, owing to the fact that it extends the normally very short-range exchange interaction to a longer range. The idea that exchange can indeed proceed by means of an intermediate nonmagnetic atom was first pointed out by Kramers[1] in 1934 [77] and the theory was more formally developed by Anderson[2] in 1950 [78]. The superexchange is of importance in ionic solids such as the transition metal oxides and fluorides, where the bonding orbitals are formed by the 3d electrons in the magnetic transition metal atoms and the 2p valence electrons in the diamagnetic oxygen or fluorine atoms.

To understand the origin and spin coupling we assume that the metal atoms are magnetic and hence have at least one unpaired electron and that the oxygen atoms have a tendency to attract two electrons (to attain the filled shell structure of Ne). In the simplest such case there are four electrons involved in the bonding between the oxygen and the metal atoms. The bonding involves symmetry adapted metal 3d and oxygen 2p orbitals as shown in Fig.5.7 for bonding along the x direction of a coordinate system. The bonding orbitals are pictured by means of the 2p and 3d orbital charge densities, where light (minus) and dark (plus) colors indicate the sign of the wavefunctions. Bonding requires overlap of wavefunctions of the same sign.

One can locate and orient the four spin polarized electrons in different ways on the three atoms. The kinetic exchange energy will be minimized if we distribute the four

[1]Hendrik Anthony Kramers 1894-1952.

[2]Philip Warren Anderson 1923. 1977 Nobel prize in physics "for their fundamental theoretical investigations of the electronic structure of magnetic and disordered systems". He was John van Vleck's student and shared his Nobel prize with him.

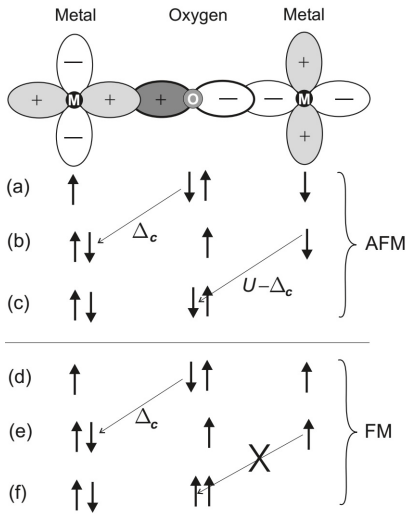

Figure 5.7: Illustration of the superexchange interaction in a magnetic oxide. The metal atoms are assumed to have a single unpaired electron and there are a total of four electrons involved in bonding. The bonding involves symmetry adapted metal 3d and oxygen 2p orbitals. (a) shows the spin configurations for an antiferromagnetic (AFM) ground state while (b) shows for a ferromagnetic (FM) ground state. For the AFM ground state the excited state (c) is the lowest energy excited state. For the FM ground state (d) no comparable low energy excited state (f) exists because it is forbidden by the Pauli principle and spin flips are not allowed. Δ_c is charge transfer energy and U is on-site Coulomb energy.

electrons across the whole system with adjacent electrons being antiparallel. The superexchange interaction therefore leads to antiferromagnetic coupling of the metal atoms with the oxygen atom remaining nonmagnetic. The size of the superexchange depends on the magnitude of the magnetic moments on the metal atoms, the metaloxygen (MO) orbital overlap and the MOM bond angle.

Becasue superexchange involves the oxygen atom orbitals as well as the metal atom, it is a second order process and is derived form second order perturbation theory. A general consequence of second order perturbation is that the energy involved is approximately given by the square of the matrix element of the transition divided by the energy cost of making the excited state. Here the transition matrix element is controlled by a parameter called the hopping integral, which is proportional to the energy width of the conduction band (bandwidth in Hubbard model) in a simple tight binding approach. The energy cost of making an exited state is given by the Coulomb energy U (Hubbard U). Thus, as in Hubbard model, $J \sim {}^{-t^2}/_{U}$. Therefore the stronger the overlap, the more negative exchange constant which will result in a strong AFM order.

Double Exchange

In oxides with mixed valence it is possible to have a ferromagnetic exchange interaction. On example is $La_{1-x}Sr_xMnO_3$ which has perovskite structure. At $x = 0$, the manganese oxidation state is 3+ and at $x = 1$ it is 4+. Therefore at some intermediate x doping, some of Mn atoms are +3 and some are +4, hence mixed valence. The end members of this compound are antiferromagnets via superexchange interaction. At $x = 0$, $LaMnO_3$ contains only Mn^{3+} ions and Mn^{3+} is a Jahn-Teller ion. $LaMnO_3$ has A-type AFM ordering. However when doped above $x = 0.175$, the Jahn-Teller distortion vanishes and the system becomes FM with a Curie temperature around room temperature.

The FM alignment is due to double exchange mechanism which can be understood

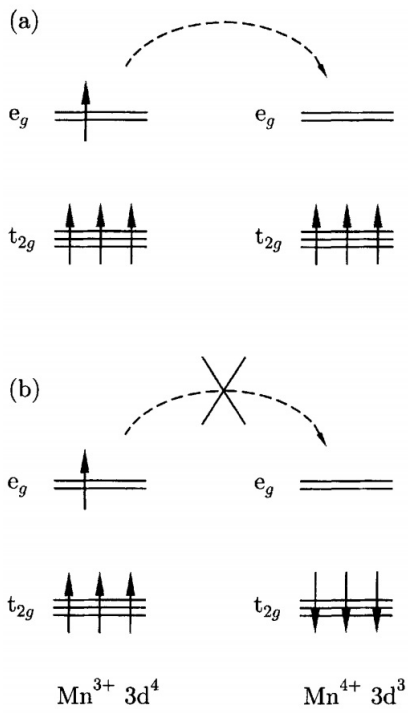

Figure 5.8: Double exchange process. The two magnetic atoms have different valences. The electron in e_g orbital of first atom hopes to the adjacent empty e_g orbital. Due to Hund's rule, the spin of hoping electron should be the same as other electron on the second atom.

with by Fig.5.8. The e_g electron on a Mn^{3+} ion can hop to a neighboring site only if there is a vacancy there of the same spin. If the neighbor is a Mn^{4+} which has no electrons in its e_g shell this should present no problem. However, there is a strong single center (Hund's first rule) exchange interaction between the e_g electron and the three electrons in the t_{2g} level which wants to keep them all aligned. Thus it is not energetically favorable for an e_g electron to hop to a neighboring ion in which the t_{2g} spins will be antiparallel to the e_g electron. FM alignment of neighboring ions is therefore required to maintain the high spin arrangement on both the donating and receiving ion. Since the ability to hop gives a kinetic energy saving, allowing hopping process shown in Fig.5.8a reduces the overall energy. Also, this hopping will make the material metallic. Double exchange, in essence, is ferromagnetic superexchange in an extended system.

RKKY interaction

In metals the exchange interaction between magnetic ions can be mediated by the conduction electrons. A localized magnetic moment spin-polarizes the conduction electrons and this polarization in turn couples to a neighboring localized magnetic moment

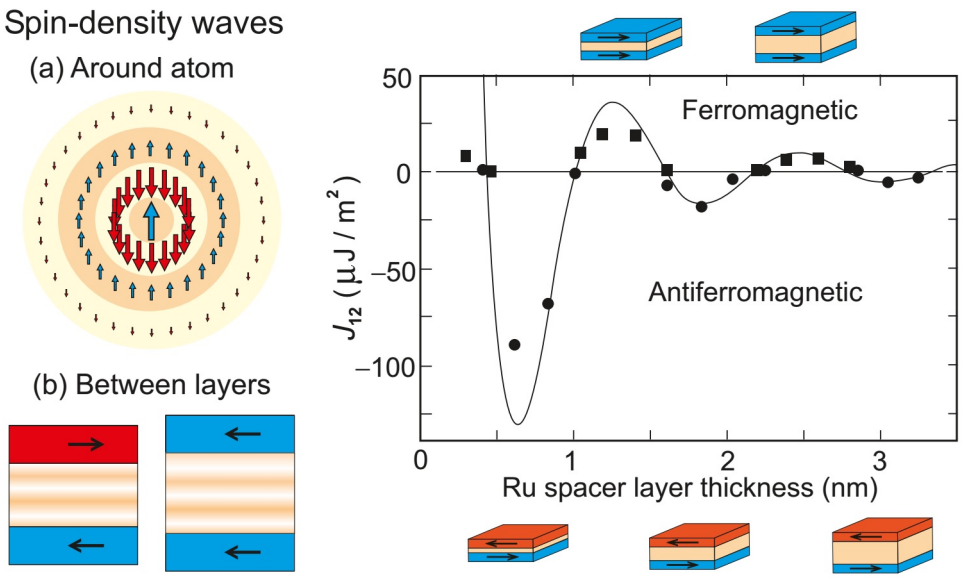

Figure 5.9: (a) Spin polarization of the conduction electrons around a localized magnetic impurity, showing the characteristic RKKY oscillations. (b) Spin polarization of electrons between two magnetic layers. The relative magnetization alignment in the two layers depends of the distance between the layers, and is caused by induced spin polarization in the nonmagnetic spacer layer, the sign of which is distance-dependent. Right: Interlayer exchange coupling strength J_{12} between two ferromagnetic $Ni_{80}Co_{20}$ layers across a Ru spacer layer of variable thickness [10]. The experiment utilized a specially engineered multilayer structure.

a distance r away. This exchange interaction is indirect because it does not involve direct coupling between magnetic moments. It is know as RKKY interaction or itinerant interaction. It is named RKKY after surname of people who discovered it, Ruderman, Kittel, Kasuya and Yosida [79–81]. The coupling takes the form of an r-dependent exchange interaction, at large r $J_{RKKY}(r)$ is,

$$J_{RKKY}(r) \propto \frac{cos(2k_F r)}{r^3} \tag{5.11}$$

where k_F is Fermi wave vector. The interaction is long range and is oscillatory depending on the distance of two magnetic atom. Therefore depending on separation of two atoms, the coupling can be FM or AFM.

The RKKY oscillatory effect is an example of a general phenomenon arising from

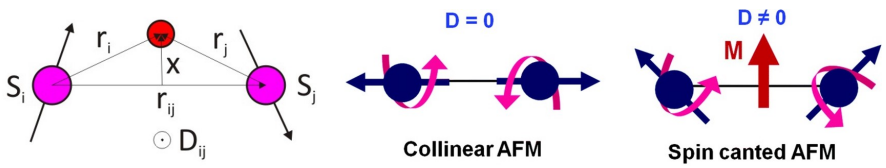

Figure 5.10: DM interaction between two local moments.

the wave nature of the quasi free conduction electrons. When such free electrons are scattered by an atom, they will rearrange themselves in order to minimize the disturbance. This process is called screening. Screening can exist for either spin or charge scattering and results in oscillations of the charge or spin density around the scattering center. The oscillations in the charge density around a point-charge impurity were first derived in 1958 by Friedel[1] and hence go by the name Friedel oscillations [82].

Perhaps the most significant application of the RKKY theory has been to the theory of giant magnetoresistance (GMR). GMR was discovered when the coupling between thin layers of magnetic materials separated by a non-magnetic spacer material was found to oscillate between ferromagnetic and antiferromagnetic as a function of the distance between the layers, as shown in Fig.5.9. This ferromagnetic/antiferromagnetic oscillation is one prediction of the RKKY theory.

5.2.6 Anisotropic exchange interation

It is also possible for the spin-orbit interaction to play role in a similar manner to that of the oxygen atom in superexchange. In this case the excited state is not connected with oxygen but is produced by the spin-orbit interaction in one the magnetic ions. There is then an exchange interaction between the excited state of one ion and the ground state of the other ion. This is known as anisotropic exchange interaction or Dzyaloshinsky-Moriya interaction [83]. When acting between two spins $\mathbf{S}_i$ and $\mathbf{S}_j$ it leads to a term in the Hamiltonian, $\hat{H}$ equal to,

[1] Jacques Friedel, 1921-2014.

$$\hat{H} = \mathbf{D}_{ij} \cdot \mathbf{S}_i \times \mathbf{S}_j \tag{5.12}$$

where $\mathbf{D}_{ij} \propto \mathbf{r}_i \times \mathbf{r}_j = \mathbf{r}_{ij} \times \mathbf{x}$. $\mathbf{D}_{ij}$ vanishes in crystals with inversion symmetry with respect to center between two magnetic ions. The form of interaction is such that it tries to force the $\mathbf{S}_i$ and $\mathbf{S}_j$ to be at right angles in a plane perpendicular to the vector $\mathbf{D}_{ij}$ in such an orientation as to ensure that the energy is negative. In effect, it will cant the spin. It usually occurs in AFMs and then results in small FM component of the moments which is perpendicular to the spin-axis of the AFM. This effect is known as *weak FM.*

5.3 Magnetic Anisotropy

Exchange interaction which is responsible for long range FM order, is isotropic in nature. Therefore, if one fill the lattice sites with local moments, in the absence of bonding, crystal field and dipole-dipole interaction, there is no preferred orientation. Introduction of any directional term in the Hamiltonian will create some type of anisotropy. The magnetic anisotropy, regardless of its source[1], is defined as the amount of energy required to rotate the magnetization from hard to easy axis. Without magnetic anisotropy thin films cannot develop a long range magnetic order since the demagnetization field will destroy it. Different types of anisotropy are listed below,

- **Magneto-crystalline Anisotropy**

  The magnetic anisotropy is the energy that it takes to rotate the magnetization from the easy direction into the hard direction, assuming a bulk sample where magnetostatic effects are absent. It is given by the anisotropy of the spinorbit energy,

[1]Can be spin-orbit interaction, directional bonding, crystal field, dipole-dipole interaction and etc ....

$$\Delta E_{SO} = \langle H_{SO} \rangle_{hard} - \langle H_{SO} \rangle_{easy} \tag{5.13}$$

so that it costs energy to rotate the magnetization into the hard direction. The atomic structure and boding in the material strongly affect the magneto-crystalline anisotropy.

- **Shape Anisotropy**

  The dipole-dipole interaction for magnetic moments is the reason behind this aniotropy. Looking at dipole-dipole interaction energy,

$$E_{dipole-dipole} = \frac{-1}{2\pi\mu_0} \sum_{i \neq j} \frac{1}{r_{ij}^3} \left[\mathbf{m}_i \cdot \mathbf{m}_j - 3 \frac{(\mathbf{r}_{ij} \cdot \mathbf{m}_i)(\mathbf{r}_{ij} \cdot \mathbf{m}_j)}{r_{ij}^2} \right] \tag{5.14}$$

  where $\mathbf{m}_i$ and $\mathbf{m}_j$ are the dipole moments and $\mathbf{r}_{ij}$ is the vector that connects them. It is seen that the energy is minimized when both dipoles are parallel to $\mathbf{r}_{ij}$ and in the same direction. For a thin film, the inter-nuclear axis is mostly in-plane, therefore shape anisotropy will cause the easy axis to lie in plane. Fig.5.11 shows that the ground state is when the moments are aligned in the same direction parallel to inter-atomic axis.. One example is LSMO.

- **Exchange Anisotropy**

  Exchange anisotropy is consequence of coupling of two magnetic moment via Coulomb interaction. It can have two form, uniaxial and unidirectional. In a FM, in the absence of external field, the magnetization is in the direction of easy axis and has two energetically equivalent state. Therefore it is called uniaxial exchange anisotropy. While in FM/AFM system, depending on exchange coupling at the interface, there is only direction that minimizes the energy, hence it is called unidirectional exchange anisotropy, or for short "exchange anisotropy".

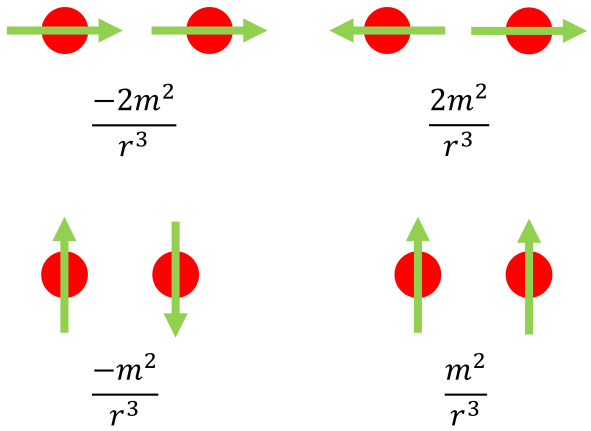

Figure 5.11: The energy from dipole-dipole interaction for each configuration is shown. Minimum energy is when two magnetic moments align in the same diretion parallel to inter-atomic axis.

Chapter 6
Broken symmetry at the interface of $La_{0.67}Sr_{0.33}MnO_3$

6.1 Introduction: Physical properties of $La_{1-x}Sr_xMnO_{3-\delta}$

The transition metal oxides $LaMnO_3$ and $SrMnO_3$ are the parent compounds of $La_{1-x}Sr_xMnO_3$ and both have perovskite structure. By A-site doping, $La_{1-x}Sr_xMnO_{3-\delta}$ shows rich phase diagram with very interesting physical properties Fig.6.1 shows the phase diagram of $La_{1-x}Sr_xMnO_{3-\delta}$. At very low doping the compound is Jahn-Teller active and the structure is distorted orthorhombic O′. Increasing doping above 0.08 the system becomes orbital-ordered insulating FM with orthorhombic structure, O″. From 0.17 to 0.48, the material is a Half-metallic FM with Curie Temperature well above room temperature. The structure in this doping level is rhombohedral. This is the doping level of interest in this work.

The major source of complexity in this material is the atomic structure of Mn and crystal field of oxygen octahedra. Mn can have various oxidation states, the most seen are: Mn^{2+}, Mn^{3+} and Mn^{4+}. In $LaMnO_3$ and $SrMnO_3$, the oxidation state of Mn is 3+ and 4+, respectively. In $La_{1-x}Sr_xMnO_{3-\delta}$, oxidation state of Mn changes from 3+ to 4+ as a function of doping. To understand what are the consequences of the in oxidation state of Mn, one have to first look at the valence structure of Mn.

Atomic Mn has 25 electrons, with electronic configuration of [Ar] $3d^5\,4s^2$. Mn^{4+} has 3 electrons in its d-orbital and Mn^{3+} has 4 electrons. In atomic level, in the absence of spin-orbit interaction and crystal field, all of these electrons are degenerate, occupying a 5-fold degenerate d-orbital. Introduction of Mn into octahedral symmetry in perovskite structure splits the d-orbital into two levels, which one of them is 3-fold

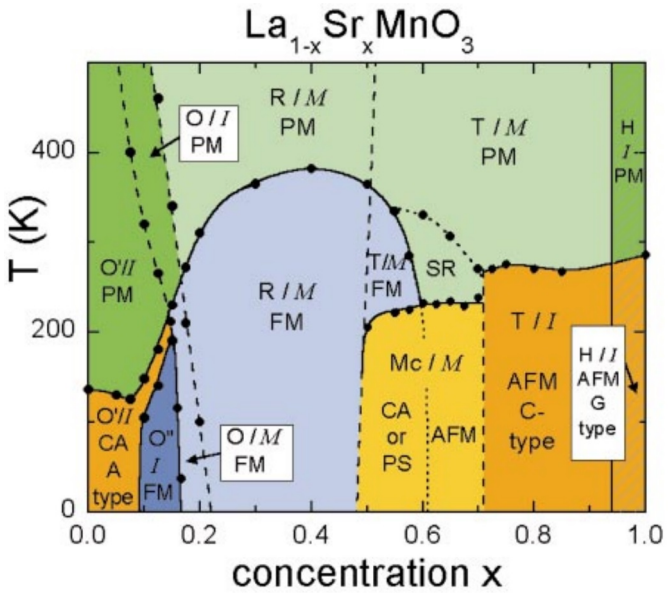

Figure 6.1: Phase diagram of $La_{1-x}Sr_xMnO_{3-\delta}$. x determines the doping level of Sr [11].

degenerate (t_{2g}) and the other is 2-fold degenerate (e_g). Fig.6.2 shows the crystal field splitting of d-orbitals. Depending on how the d-orbitals are filled, the physical properties of material changes. We can see here that there is an intimate correlation between electrons, orbitals, lattice (through crystal field) and spin (Hund's rule and Coulomb interaction). As shown in Fig.6.3, electron filling of Mn d-orbital governs the properties of the compound.

In the following, first the parent compounds will be introduced and then the electronic and magnetic properties of $La_{0.67}Sr_{0.33}MnO_3$ will be discussed.

Table 6.1: The structural and magnetic properties of $LaMnO_3$ [1]. $R\overline{3}c$ appears only above room temperature.

$LaMnO_3$	Structure				Magnetic	
	Symm.	a (Å)	b (Å)	c (Å)	State	T_N, T_C (K)
I	Pnma	5.73	7.70	5.53	AFM (G-type)	140
II	Pnma	5.49	7.78	5.53	FM	140
III	$P112_1/a$	5.46	7.76	5.52	FM	140
IV	$R\overline{3}c$	5.52	13.32			

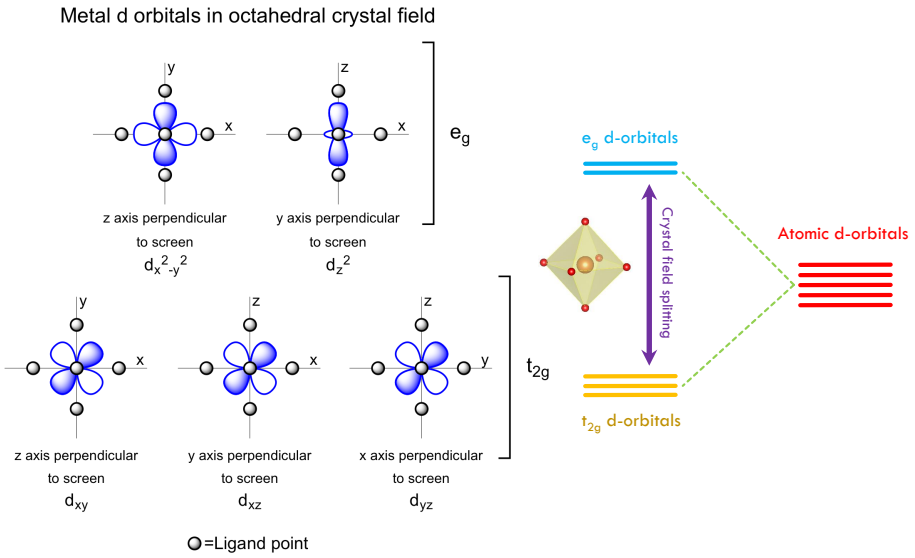

Figure 6.2: Atomic d-orbitals in the presence of crystal field (ligand field) split to two levels, t_{2g} and e_g. d_{xy}, d_{xz} and d_{yz} orbitals belong to t_{2g}. The $d_{x^2-y^2}$ and d_{z^2} orbital belong to e_g.

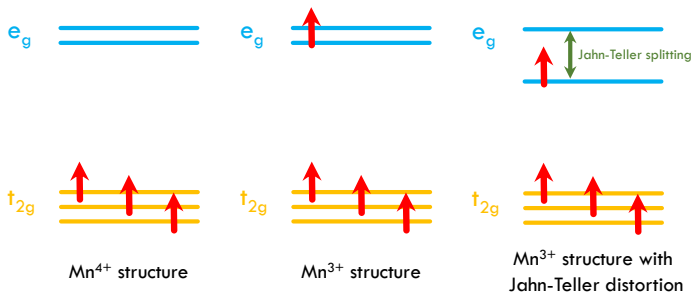

Figure 6.3: a) The electron-filling of Mn in 4+ state is shown which is the case for $SrMnO_3$. b) Mn^{3+} in the absence and c) in the the presence of Jahn-Teller distortion which happens in $LaMnO_3$.

6.1.1 $LaMnO_3$

In bulk, the depending on temperature, $LaMnO_3$ is Jahn-Teller active insulating material that shows four types of magnetic and structural orders which are summarized in table. The table is re-created from Ref. [1]. It shows that stoichiometric $LaMnO_3$ is an AFM with orthorhombic structure. Fig.6.3(b-c) shows the electron filling of d-orbital. Above $T_{JT} = 750K$ [84], Jahn-Teller temperature, the system is a PM metal with FM interactoin. Huang et. al [1] found that annealing in oxygen introduces small amounts of additional oxygen in the system where this additional oxygen appears to be accommodated by introducing La and Mn vacancies in the structure. This has the effect of changing magnetic structure from AFM to FM, with increasing defect, extra oxygen and La, Mn vacancies, the structure changes from orthorhomnic to monoclinic-rhombohedral. Their observation was further confirmed by Töpfer and Goodenough [85]. These evidences show that processing plays a major role in the physical properties of this compound.

6.1.2 $SrMnO_3$

$SrMnO_3$ crystallizes in two forms, cubic and hexagonal. In cubic phase it has perovskite structure ($Pm\overline{3}m$), the octahedra are corner shared while in the hexagonal phase, there are every other corner shared and face-sharing [86]. Fig.6.4 shows the two structures. The hexagonal $SrMnO_3$ is antiferromagnetic with Néel temperature of 278 K [87] or 350 K [88]. The discrepancy in Néel temperature is attributed to the short range interactions between Mn^{4+} ions in the face-sharing octahedras above 278 K [87]. Different amount of oxygen vacancy is put forward as another reason for different Néel temperature [89].

$SrMnO_3$ is cubic at high temperature and can be quenched and stabilized at low temperatures. Cubic $SrMnO_3$ is a G-type AFM with Néel temperature ranging from

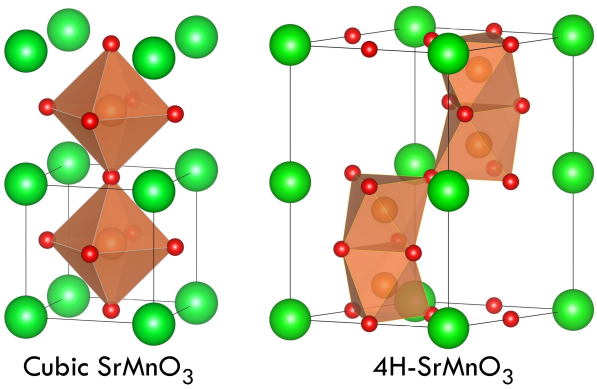

Figure 6.4: The cubic and hexagonal of $SrMnO_3$.

233 to 260 K [90–92].

Both phases of $SrMnO_3$ are insulators. The nature of gap is not clear as some experiments suggest that to a large extent, it is a charge transfer gap [93, 94] while others indicate that the O 2p and 3d orbitals are heavily hybridized therefore the gap is a mixture of Mott and charge transfer [95, 96].

Interestingly enough, again processing plays an important role in the physical properties of $SrMnO_3$.

6.2 Physical properties of $La_{0.67}Sr_{0.33}MnO_3$

The discovery of colossal magnetoresistance in the perovskite manganites has started great interest to investigate and understand this phenomena, mainly due its potential application in magnetic sensors and data storage devices [97,98]. Among the perovskite manganite family, $La_{0.67}Sr_{0.33}MnO_3$ is a half-metal with 100% spin polarization along with highest Curie temperature. These properties makes $La_{0.67}Sr_{0.33}MnO_3$ an ideal material for device applications, such as, magnetic tunnel junction [99–102], Schottky devices [103–105] and magnetoelectric devices [106, 107]. Due to the spin polarization of $La_{0.67}Sr_{0.33}MnO_3$, it has been used to study other materials like spin injection in cuprates superconductors [108, 109].

The physical properties of $La_{0.67}Sr_{0.33}MnO_3$ thin film strongly depend on composition

and strain. Considerable amount of effort has been focused on what is the best condition to create a $La_{0.67}Sr_{0.33}MnO_3$ thin film where its physical properties are at optimal level. For example, what is the thinnest film which shows metalicity and magnetism at the same time or what is the optimal Curie temperature for this system [110,111]. Deviating from the optimal growth condition often results in degradation of physical properties, i.e. the suppression of magnetism and poor conductivity at ultra thin films.

There has been numerous efforts to optimize the growth of $La_{0.67}Sr_{0.33}MnO_3$, a good summarizing work can be find here [110]. In this chapter, first the standard measurements of physical properties are presented for $La_{0.67}Sr_{0.33}MnO_3$ which are well-known and will be used as measure of the quality the samples. Then the focus will be around the magnetic property of this exotic material which has not received enough attention. Later in this chapter it is shown that it is possible to control the processing (thermodynamic) condition to obtain new functionality in $La_{0.67}Sr_{0.33}MnO_3$.

6.2.1 Growth and characterization of $La_{0.67}Sr_{0.33}MnO_3$

Through this thesis all the thin films are grown on $SrTiO_3$[1]. In order to obtain a high quality epitaxial $La_{0.67}Sr_{0.33}MnO_3$, the first step is the prepare an atomically flat substrate which is free of any contamination. The latter requires *in-situ* treatment. The *ex-situ* processing was introduced earlier in section 4.3.1. In addition to the *ex-situ* treatment, prior to introduction of oxygen in the chamber, the sample was annealed in a vacuum better than 2×10^{-8} Torr . This step is important, as it was discussed in the section 4.3.1, this surface is weakly polar and prone to absorbing contamination. Careful *in-situ* annealing at a temperature lower (around 550 °C) than growth temperature ensures a clean termination on the substrate. after annealing the substrate in vacuum, the oxygen was introduced into the chamber. A previous study in our group shows that

[1]Unless otherwise is stated.

80 mTorr of ozone/oxygen mixture (6%) is enough to minimize the oxygen vacancies and result in good conductivity. With this amount of oxygen pressure, the thinnest dead layer was obtained [111]. Therefore, the oxygenated $La_{0.67}Sr_{0.33}MnO_3$ thin films were grown in this pressure. Using a pulse laser and a stoichiometric $La_{0.67}Sr_{0.33}MnO_3$ target, the ablated $La_{0.67}Sr_{0.33}MnO_3$ particles were deposited on the substrate. The pulses with 190 mJ energy and repetition rate of 10 Hz where shot at the target. Using a lens, the focus of laser pulses was adjusted to ensure uniformity of ablation on target on one hand and intensity of ablated plasma to ensure adequate supersaturation, on the other hand. The growth temperature was set to 640-660 °C. The real time growth was monitored using RHEED and the desired thickness was obtained by counting the number of RHEED oscillations. After growth, the samples were cooled down in growth pressure in 45 min. Figure 6.5 shows the RHEED pattern and oscillation for 20 uc $La_{0.67}Sr_{0.33}MnO_3$ thin film. The oscillation confirms that growth is in layer-by-layer mode and the streak like pattern is an indication of smooth surface[1]. The initial drop in the intensity of RHEED spot is due to the difference in reflectivity of $SrTiO_3$ and $La_{0.67}Sr_{0.33}MnO_3$. Reflectivity strongly depends on density.

6.2.2 Structure

In bulk, $La_{0.67}Sr_{0.33}MnO_3$ has rhombodedral structure, $R\overline{3}c$ (No. 167) which is shown in Fig.6.6. The lattice constant is 5.471 Å and the $\alpha_r = 60.43°$ [112]. The octahedras in this structure are rotated out-of-phase and equally along all psuedo-cubic axis where in Glazer's notation is $a^-a^-a^-$ [113]. The rhombohedral structure is related to psuedo-cubic structure by,

[1]The streak line pattern is a direct consequence of finite thickness in (001) direction. It is coming from uncertainty principle between real and reciprocal space. Finite in real space, broad (streak) in reciprocal space.

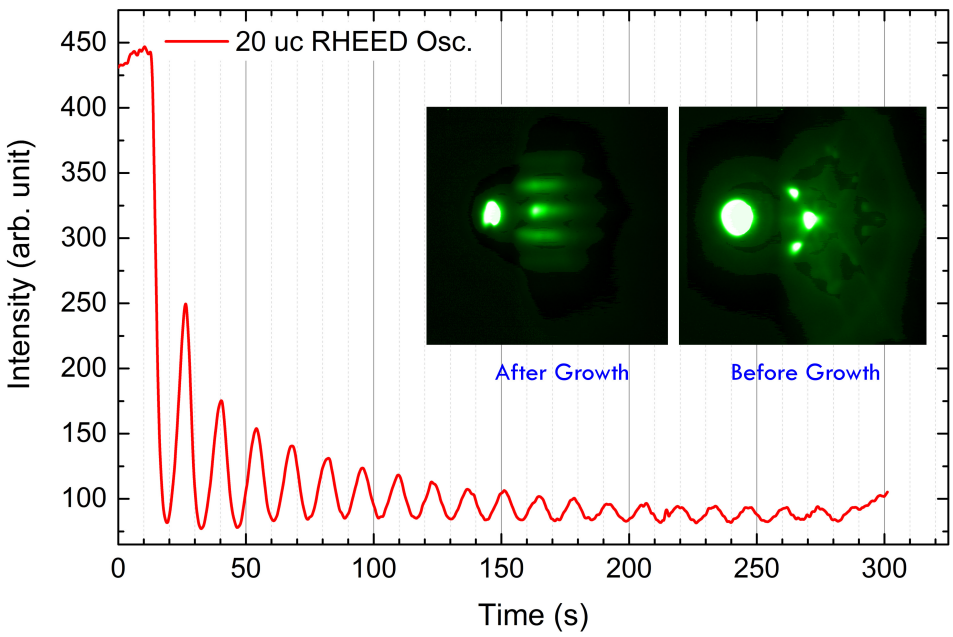

Figure 6.5: RHEED oscillations for $La_{0.67}Sr_{0.33}MnO_3$ grown at 80 mTorr oxygen. The substrate and thin film RHEED patterns are shown in the inset. The Kikuchi lines on the substrate, before growth, shows the flatness of the substrate surface.

$$\begin{aligned} \alpha_{ps} &= cos^{-1}\left(\frac{1-2cos\,\alpha_r}{2cos\,\alpha_r\,-3}\right) \\ a_{ps} &= \frac{\sqrt{2}a_r}{1+cos\,\alpha_{ps}} \end{aligned} \tag{6.1}$$

However, in thin films grown on cubic substrate like $SrTiO_3$, it is more straight forward to use distorted orthorhombic notation. Fig.6.7 show how thin film $La_{0.67}Sr_{0.33}MnO_3$ with orthorhombic structure is related to cubic $SrTiO_3$. The Miller indices for cubic (substrate) are related to orthorhombic Miller indices can be converted using the following relations,

$$h_o = (l-k)_c \qquad k_o = (l+k)_c \qquad l_o = 2\,h_c \tag{6.2}$$

To further understand the structure of the thin film, XRD measurement was per-

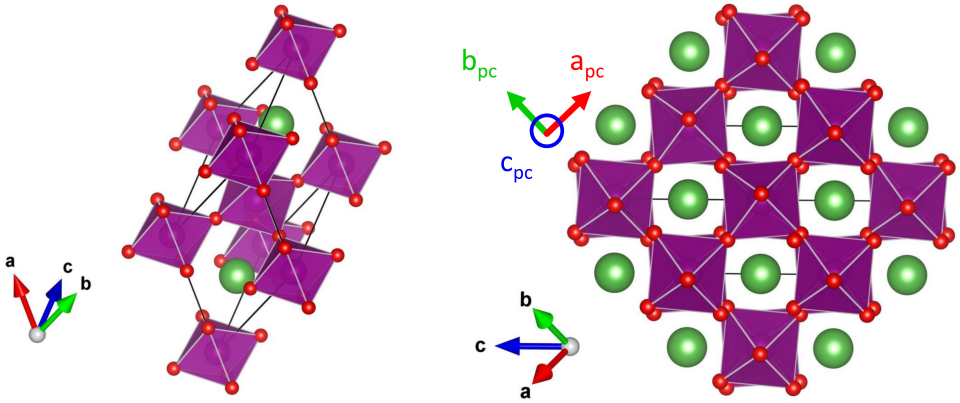

Figure 6.6: $La_{0.67}Sr_{0.33}MnO_3$ structure. *Left* Rhombohedral *Right* Rhombohedral structure projected along $[11\bar{1}]_r$ which shows the psuedo-cubic structure as well. The psuedo-cubic lattice vectors are shown.

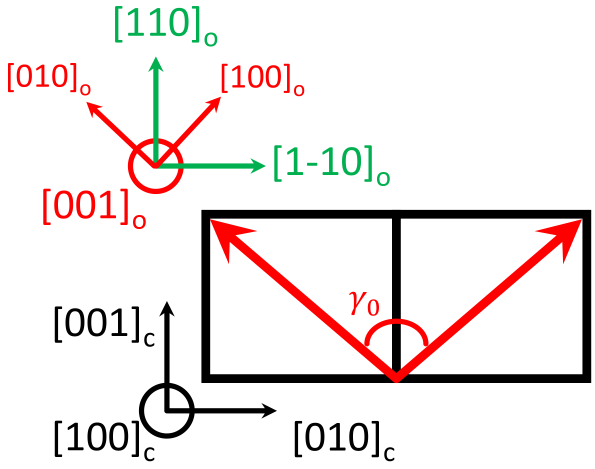

Figure 6.7: The relative coordinate system of substrate (cubic) and layer (orthorhombic) is shown.

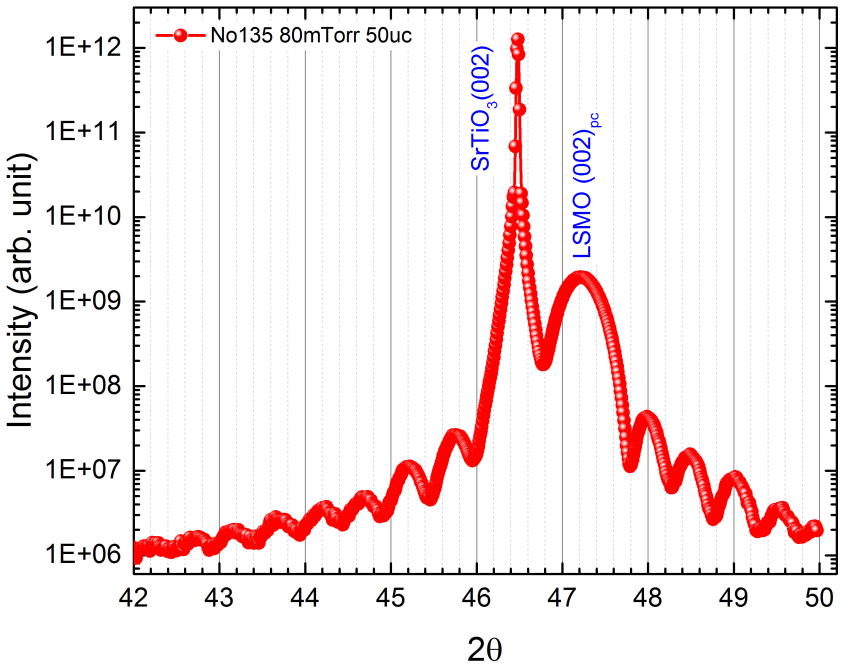

Figure 6.8: XRD of $La_{0.67}Sr_{0.33}MnO_3$ grown in 80 mTorr of oxygen. The Thickness fringes are seen due to high quality of the thin film.

formed. Fig. 6.8 shows the XRD for a 50 uc thick thin film of $La_{0.67}Sr_{0.33}MnO_3$ grown in 80 mTorr of oxygen. The presence thickness fringes (Kiessig fringes) indicates that the film has a smooth surface and interface. The substrate position is at 46.47° and the thin film is at 47.22°. Using the position of thin film peak position and Bragg's law the c-axis lattice constant is 3.846 Å which agrees well with other reports for optimally grown $La_{0.67}Sr_{0.33}MnO_3$ [110]. The spacing of thickness fringes gives the the thickness of the thin film which is 19.1 ± 0.6 nm. The thickness and c-axis lattice constant gives 49.66 uc which agrees well with 50 RHEED oscillations.

Fig.6.9 shows the reciprocal space mapping (RSM) of $La_{0.67}Sr_{0.33}MnO_3$. The results are summarized in table 6.2. To gain more information about the orthorhombicity of the structure, RSM around several asymmetric points were measured. Assuming that $La_{0.67}Sr_{0.33}MnO_3$ is in orthorhombic structure, the relation between Miller indices and

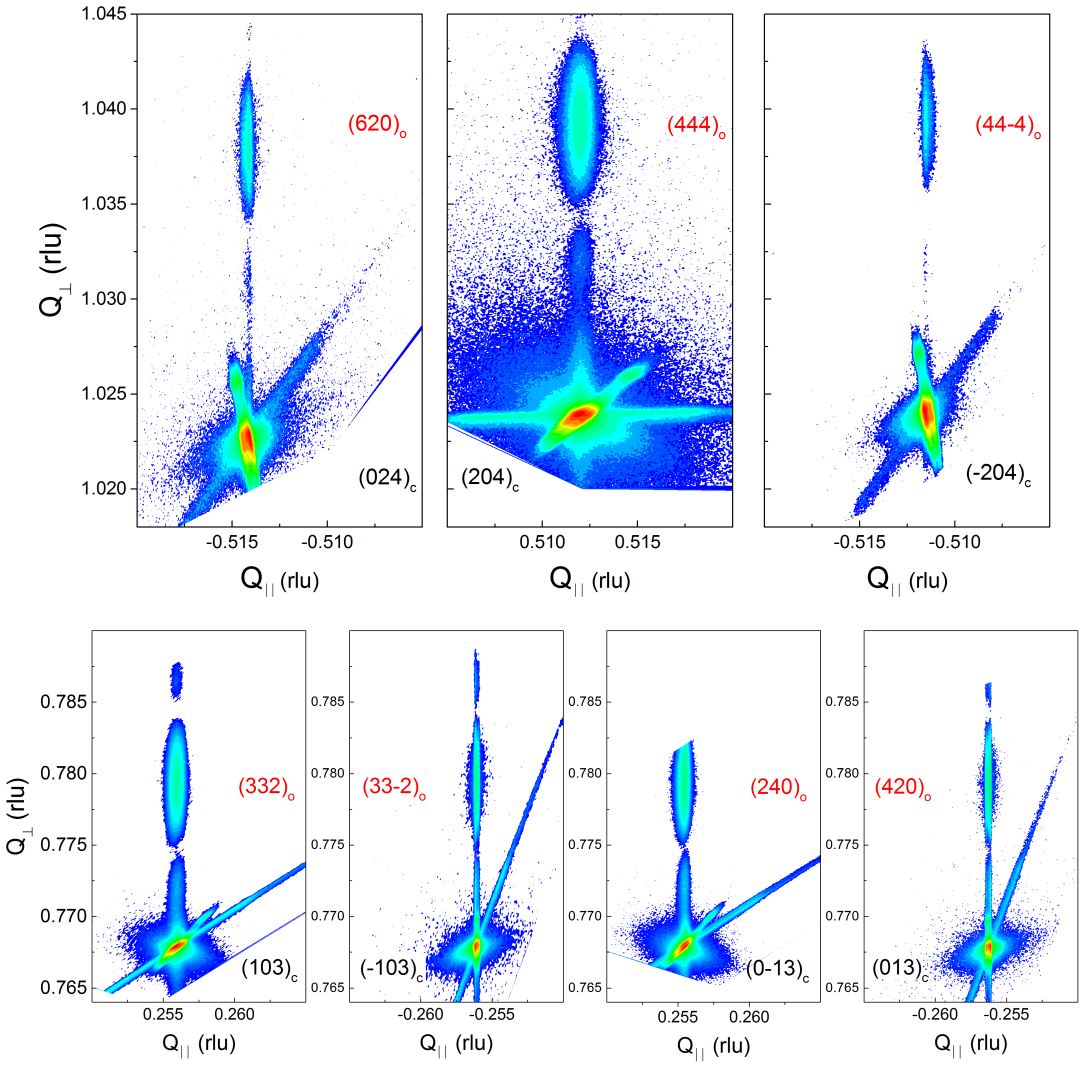

Figure 6.9: RSM of $La_{0.67}Sr_{0.33}MnO_3$ around (620), (444), (44-4), (332), (33-2), (240) and (420) Bragg reflection. The red labels belong to $La_{0.67}Sr_{0.33}MnO_3$ and the black labels indicate $SrTiO_3$ Bragg's reflection. The asymmetry of substrate (streak) Bragg reflection is due to absence of analyzer on detector side.

Table 6.2: Summary of RSM map of $La_{0.67}Sr_{0.33}MnO_3$.

Bragg's peak	ω	2θ	q_x (rlu)	q_y (rlu)	q_z (rlu)	Q	d_{hkl}	
$\bar{1}03$	57.0284	77.1836	-0.2561	0	0.7682	0.8098	1.2349	Sub (cubic)
$33\bar{2}$	57.3944	78.4306	-0.2561	0	0.7798	0.8208	1.2184	Layer (ortho)
103	20.1565	77.1818	0.2561	0	0.7682	0.8097	1.2349	Sub (cubic)
332	21.0165	78.4157	0.2562	0	0.7796	0.8206	1.2186	Layer (ortho)
$0\bar{1}3$	20.2880	77.1720	0	0.2542	0.7687	0.8097	1.2351	Sub (cubic)
240	21.1580	78.4063	0	0.2542	0.7802	0.8205	1.2187	Layer (ortho)
013	57.1590	77.1799	0	-0.2579	0.7676	0.8097	1.2350	Sub (cubic)
420	57.5290	78.4404	0	-0.2579	0.7793	0.8208	1.2182	Layer (ortho)
$\bar{2}04$	88.4546	123.7977	-0.5119	0	1.0243	1.1452	0.8732	Sub (cubic)
$44\bar{4}$	89.4566	126.5025	-0.5119	0	1.0401	1.1593	0.8626	Layer (ortho)
204	35.3198	123.783	0.5123	0	1.0241	1.1451	0.8732	Sub (cubic)
444	36.9698	126.3688	0.5124	0	1.0391	1.1586	0.8631	Layer (ortho)
024	88.5955	123.7541	0	-0.5145	1.0230	1.1451	0.8732	Sub (cubic)
620	89.5705	126.3867	0	-0.5145	1.0384	1.1589	0.8629	Layer (ortho)

lattice parameters is,

$$\frac{1}{d_{hkl}^2} = \frac{h^2}{a_c^2} + \frac{k^2}{b_c^2} + \frac{l^2}{c_c^2} \tag{6.3}$$

were a_c, b_c and c_c are lattice parameters in cubic notation. From $\theta - 2\theta$, $c_c = 3.848$ Å was measured. From data in table6.2 and using the above equation, the in-plane lattice constants are $a_c = 3.897 \pm 0.005$ Å and $b_c = 3.893 \pm 0.005$ Å. The angle γ_o, as shown in Fig.6.7, determines the deviation of the structure from a perfect orthorhombic structure. This angle is related to cubic lattice constants using the below equation,

$$2c_c = \sqrt{a_o^2 + b_o^2 - 2a_o b_o \, cos\gamma_o} \tag{6.4}$$

where $a_o = b_o = \sqrt{a_c^2 + c_c^2}$. This yields to $\gamma_o = 90.72°$. This shows that $a_c = b_c > c_c$ and $\gamma_o > 90°$. In order to fulfill this condition, the rotation of octahedra around cubic c-axis should diminish while rotations around cubic a and b-axis can still be present. In Glazer's notation [113], such a tilt pattern is shown by #18 ($a^+a^-c^0$). The tilt system #16 ($a^+a^+c^0$) satisfies the lattice parameters conditions as well, but comparing to the tilt system of bulk #14 ($a^-a^-a^-$), the ($a^+a^-c^0$) tilt system seems more energetically favorable, as it maintains one out-of-phase tilt. It is important to notice that in #18 tilt system in Glazer's notation, the octahedra has to deform in order to maintain the connectivity of octahedras. This deformation is very small, 0.002 Å, which is not possible to measure using our XRD.

6.2.3 Electrical transport

The electrical resistivity is shown in Fig.6.10(a). It was measured using four probe method. Cold deposited gold/palladium was used as contacts to minimize contact resistance. The 10, 30 and 50 uc $La_{0.67}Sr_{0.33}MnO_3$ thin films show a steady decrease in the resistivity of this thin film with inceasing the thickness. For each thin film, the

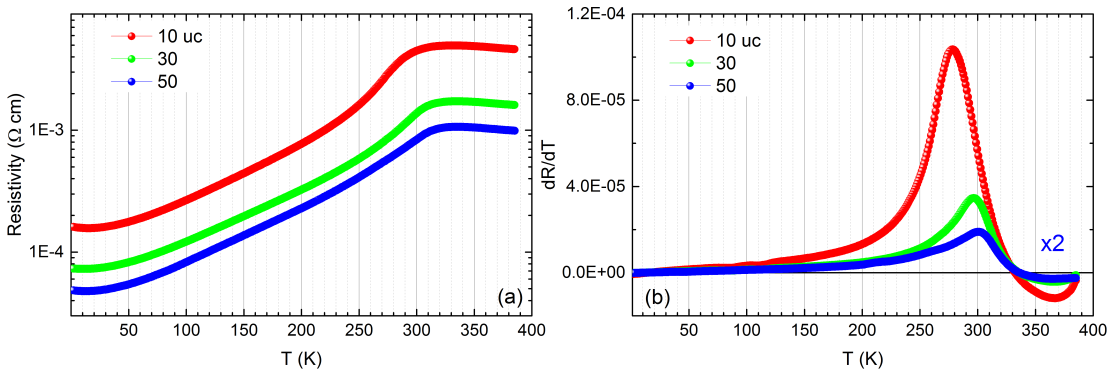

Figure 6.10: a) Electrical resistance of $La_{0.67}Sr_{0.33}MnO_3$ as a function of thickness. b) First derivative of electrical resistance as a function of thickness.

resistivity increases and then decrease which means at first it behaves like an insulator and then it changes to metallic behavior. The insulator-to-metal transition temperature is 332, 337 and 338 K for 10, 30 and 50 uc, which is usually related to Curie temperature which is best seen in the derivative of resistivity with respect to temperature in Fig.6.10(b). The rate of changing the resistivity shows a maximum (inflection point) which can be related to growth of FM phase in $La_{0.67}Sr_{0.33}MnO_3$. The second order nature of FM phase transition which grows non-monotonically with temperature results in the non-monotonic decrease of resistivity in $La_{0.67}Sr_{0.33}MnO_3$. The residual resistivity ratio (RRR), ρ_{300K}/ρ_{2K}, which reflects the quality of thin films, are 2.8, 17.8 and 17.6 for 10, 30 and 50 uc, respectively. RRR can be related impurity induced (defect, vacancies and other types of temperature independent imperfection) resistance. The RRR reported here surpasses a similar work [110] and has the same value comparing to the work recently done in our group [111].

6.2.4 Magnetic properties

$La_{0.67}Sr_{0.33}MnO_3$ is half-metal soft ferromagnet which its high Curie temperature (340 K in thin film, 370 K in bulk) makes it a promising candidate for future device applications. Its magnetic properties has been studied in detail before. For instance refer to Ref. [110] and references therein. In this section the normal magnetic properties

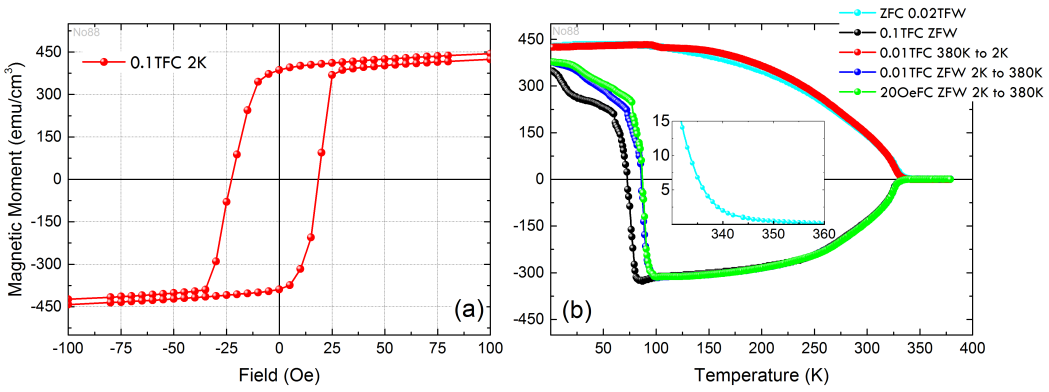

Figure 6.11: a) M-H curve for 50 uc of $La_{0.67}Sr_{0.33}MnO_3$ at 2K. The thin film was field cooled under 0.1T. b) Magnetic moment as a function of temperature for the same thin film under different field cycling. The onset of FM is seen in the inset which is around 340K.

our thin films will be reviewed. A new property that is observed and reported here for the first time will be discussed. It will be shown that the thin films go through a spontaneous magnetic reversal. Additionally, it shows hysteresis reversion as a function of temperature.

Figure 6.11 shows the magnetic properties of 50 uc $La_{0.67}Sr_{0.33}MnO_3$. The M-H curve shows a normal hysteresis. 20 ± 3 Oe is the coercivity which is very small. The Magnetization quickly saturates, as is seen, above 37 Oe the coercivity lines close. It means at 2K, a magnetic field of 37 Oe and above, can completely reverse the direction of magnetic moments. Fig.6.11b shows the change of magnetic moment as a function of temperature. Since the easy axis of $La_{0.67}Sr_{0.33}MnO_3$ is in-plane, the measurements have been performed in the plane of $La_{0.67}Sr_{0.33}MnO_3$. The magnetic field is applied in [100] direction, while the thin film is grown in [001] direction. In Fig.6.11b, ZFC is short for Zero Field Cooled, ZFW is short for Zero Field Warmed. The onset of magnetism is seen in the cyan line, where the sample was ZFC and then 0.02T FW. The inset shows that the Mn moments start to align ferromagnetically around 340K. This curve is the normal M-T curve that one would expect from $La_{0.67}Sr_{0.33}MnO_3$. Upon

changing the field training, the magnetic response of $La_{0.67}Sr_{0.33}MnO_3$ changes as well. The black line shows the 0.1T FC and measured in ZFW mode. It is seen that there is a drop in magnetic moment that starts slowly at low temperature (5K). Around 60K, the direction of magnetic moment reverses. This spontaneous magnetic reversal occurs in various field training. To better understand this peculiar magnetic behavior, different types of field training and cycling were measured. Fig.6.11b show that going from 380K to 2K under 0.01T (just 100 Oe, red curve), the magnetization is positive. In the cool down cycle, M-T shows a typical behavior of a normal FM. At 2K, the magnetic field was turned off, and then the temperature was increased to 380K while measuring the magnetic moment. Red and blue curve show a full cycle of going from 380K to 2K with 0.01T and then coming back to 380K under zero magnetic field. It is seen that the M-T, during cooling and warming is not the same. The green curve shows a similar cycling with difference that the cooling field was 0.002T (20 Oe) instead of 0.01T. Again the same behavior is seen. To check the reproduciblity of this behavior, the experiment was repeated for another 50 uc sample as well as 10 and 30 uc samples. Fig.6.12 shows the magnetic moment vs temperature for 50, 30 and 10 uc samples. All samples show a similar trend. Under the same field training, they all show spontaneous magnetic moment reversal. The onset of magnetic moment reversal is almost the same for all the samples, which is around 50 to 60 K. Except for the 10 uc samples, they all show a kink around 105 K, cubic-tetragonal transition of $SrTiO_3$. The temperature span for 10, 30, 50 (cyan) and 50 (green) samples are 55, 23, 20 and 12 K, respectively. For 10 uc sample, the reversal is less abrupt and is wider in temperature, comparing to thicker samples. The wide reversal temperature for 10 uc samples includes the transition which could be the reason for the absence of the 105 K kink. Cyan and green line show the M-T curve of two 50 uc samples. Although the low temperature behavior of the two samples are qualitatively the same, but at high temperature, the onset of FM shows a

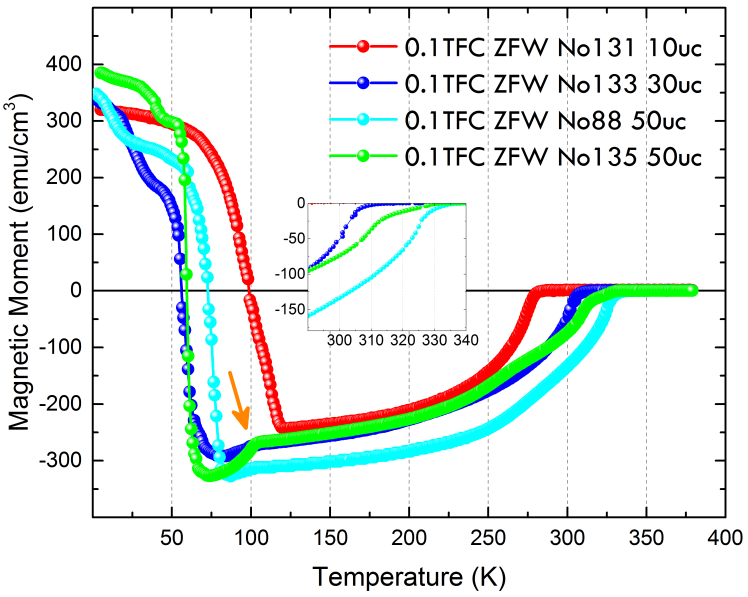

Figure 6.12: M-T graph of $La_{0.67}Sr_{0.33}MnO_3$ as a function of thickness. The arrow show the kink position at $SrTiO_3$ structural phase transition. The inset shows the onset of ferromagnetism.

subtle difference. They slope of M-T curve at the onset of FM is not the same. These data suggest that the steeper the onset of FM, the more gradual the magnetic reversal.

In the figures 6.13b, c and d the hysteresis is shown where before the measurement, the thin film was cooled from 380 K to 2 K in 1000 Oe magnetic field and then under zero field, it was warmed up to the target temperature where hysteresis was measured in $\pm 10k\,Oe$. This would ensure that the hysteresis is measured at the target temperature along the M-T curve (fig.6.13a). Each hysteresis cycle is presented in two half-cycles, empty symbol shows the leftward half and solid symbol shows the rightward half of hysteresis cycle. Fig.6.13b shows the hysteresis curves from 2 K to 75 K which is the normal hysteresis for a soft ferromagnet with coercive field of 20 Oe and agrees well with previous reports [110, 114, 115].

The coercivity decreases with increasing temperature which partly can be due to thermal activation energy. As shown in fig.6.13c and d, further increase in temperature, past the reversal point, another peculiar behavior is observed. The magnetic

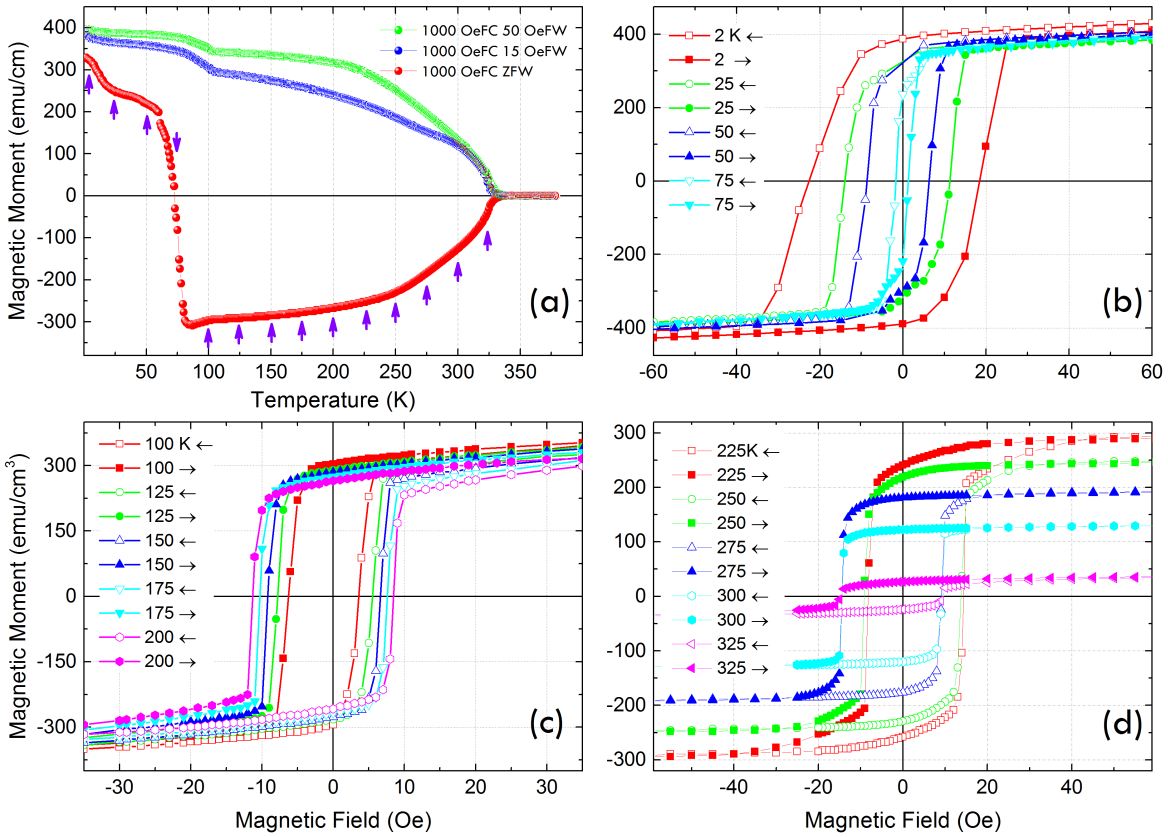

Figure 6.13: Magnetic measurements of 50 uc LSMO/STO (001). a) Magnetic moment as a function of temperature under different training. b-d) The ferromagnetic hysteresis measurement as a function of temperature from +10k Oe to -10k Oe and back, which ensures magnetic saturation of the thin film. The measurements were performed at temperature points indicated by arrows in part (a). Prior to each hysteresis measurement, the thin film was cooled in 1k Oe from 380 K to 2 K, then in zero magnetic field it was warmed up to the target temperature. The arrows in the legend show the direction of magnetic field sweep.

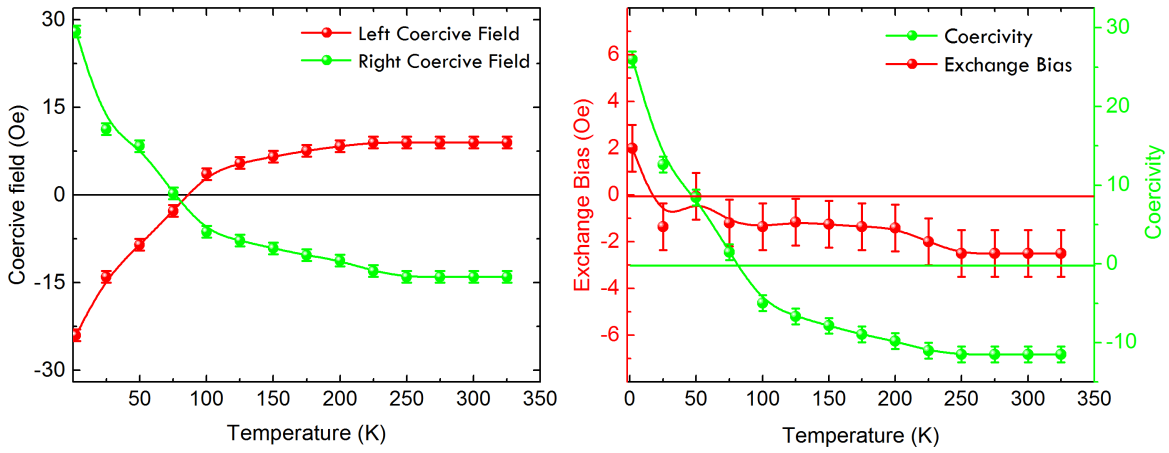

Figure 6.14: Left: The Change in the left and right coercive field as a function of temperature. It shows that both coercive field change symmetrically. Right: The coercivity and exchange bias as function of temperature.

moment reverses to a negative value in the presence of a positive magnetic field, i.e. the hysteresis becomes inverted, hence the coercivity becomes negative. From 100 K to 275 K the negative coercivity increases with increasing temperature and saturates at higher temperatures. Negative coercivity persists up to 325 K which is well above room temperature. We believe that this behavior will persist up to Curie temperature, however the measurement is not performed due to the small ferromagnetic (FM) signal near Curie temperature. The left and right coercive field change symmetrically and a very small exchange bias is observed which changes with temperature. The exchange bias hints toward the presence of AFM coupling the material (fig.6.14).

Figure 6.15 shows the AC magnetic susceptibility (real part) which is measured in 10 Hz. The magnetic susceptibility is a response function where it shows a strong dependence on applied magnetic field. Under zero magnetic field, there are several magnetic features that they vanish under a small magnetic field (50 Oe). The most obvious difference is centered at 60 K which is the same temperature as the onset of spontaneous magnetic reversal. Presence of external field, completely diminishes this feature which explains the absence of spontaneous magnetic reversal under magnetic field. AC

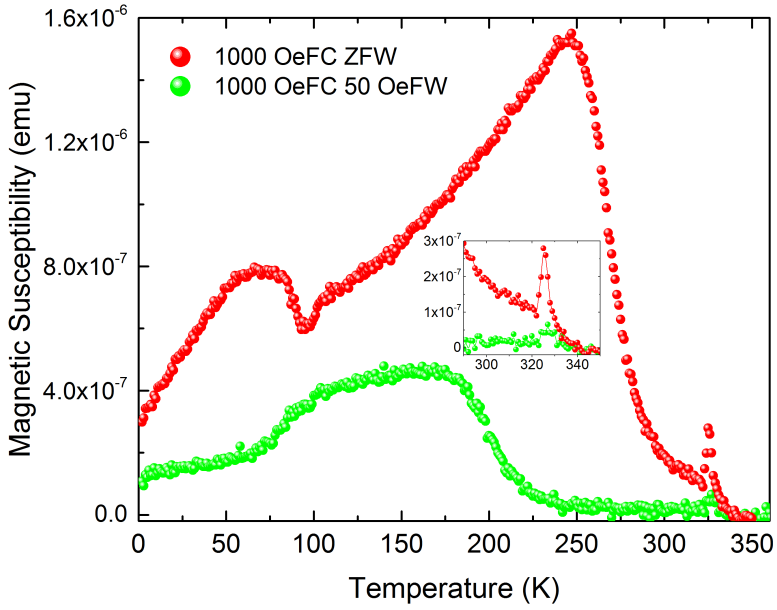

Figure 6.15: AC susceptibility measured in the presence and absence of magnetic field.

magnetic susceptibility shows a reentrant feature that peaks around the reversal temperature (60 K) that points toward the onset of a new magnetic ordering (fig.6.15). The concomitant occurrence of this feature and spontaneous magnetic reversal on one hand, and presence of interfacial AFM coupling on the other hand, validates the assumption of having a new magnetic order near the interface which differs from the rest of the thin film. The magnetic reversal at remanent state was reported before [116], however the reversal temperature was determined, using X-ray magnetic circular dichroism (XMCD), 125 K which is more than double the reversal temperature (60 K) in this work. However, it was shown that by careful engineering of Sr concentration in the first unit cell of LSMO near the interface, it is possible to lower the reversal temperature to 60 K [117].

Fig.6.16 shows the spontaneous magnetic reversal for 50 uc $La_{0.67}Sr_{0.33}MnO_3/SrTiO_3$. The sample was cooled down in 1000 Oe external magnetic field from 380 K to 2 K and then magnetization was measured in the absence of external magnetic field (ZFW). As shown schematically in fig.6.16, at 2 K, all the moments are frozen in the direction of external magnetic field. In the absence of magnetic field, AFM interaction between first

Mn layer with the next Mn layer should result in the reversal of magnetic moments in the rest (away from interface) of the thin film. However, presence of anisotropy creates an energy barrier that impedes this reversal. As seen in the fig.6.16, at very low temperature, all the moments are aligned (step 1), but as the temperature goes up, the thermal fluctuations assist the reversal of magnetic moments and lower the free energy. Around 50 K (step 2) the thermal energy is large enough to cause a progressive reversal of all the magnetic moments (step 4). Then, the system being at lowest energy, the FM part of thin film behaves as a normal Curie FM all the way up to Curie temperature where above that temperature it becomes a PM (step 5).

6.2.5 Microscopic structural and electronic properties

The symmetry mismatch at the interface may lead to Jahn-Teller like distortion of the BO6 octahedra. This type of distortion in $La_{0.67}Sr_{0.33}MnO_3/SrTiO_3$ (110) has previously shown that leads to appearance of high-temperature magnetic insulating phase near the interface [118]. The same type of distortion could be present in the thin films grown in [001] direction. We have studied the microscopic properties of the interface using scanning transmission electron microscopy (TEM). Using high angle annular dark field (HAADF) and annular bright field (ABF) imaging the structure was investigated on atomic level. In order to resolve the octahedra structure, i.e. the tilt pattern, the images were acquired along $[1-10]_c$ where interface is along $[110]_c$. As shown in fig.6.17, this direction was chosen since the atomic arrangement in other directions such as $[100]_c$ or $[110]_c$ do not show the tilt structure [12]. It is noteworthy that the tilt structure observed in $[1-10]$ direction, is a superposition of rotation of octahedra around three pseudo-cubic axes.

The STEM-HAADF and STEM-ABF images of $La_{0.67}Sr_{0.33}MnO_3/SrTiO_3$ (001) is shown in Fig.6.18a and b and the interface is marked by a small red arrow. The thin film structure is well-ordered and coherent. The position of heavier atoms is seen in the

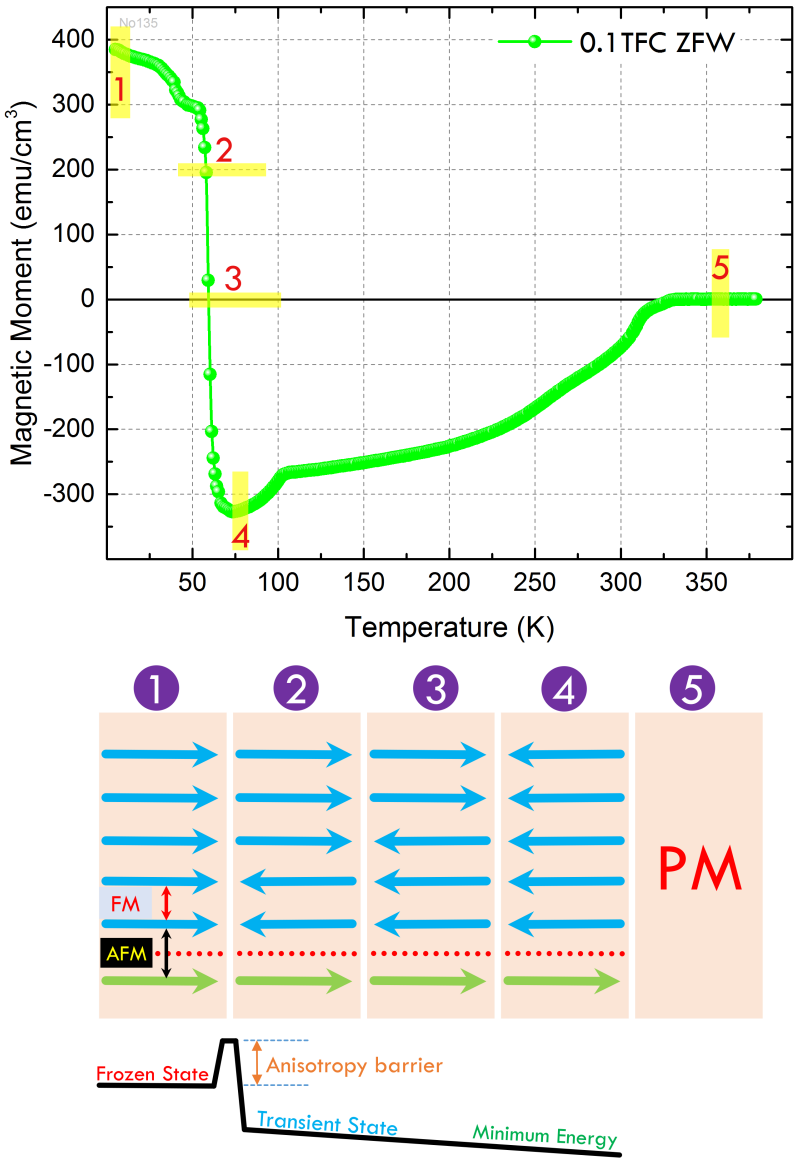

Figure 6.16: The spontaneous magnetic reversal for 50 uc $La_{0.67}Sr_{0.33}MnO_3$. The schematic behavior of magnetic moments (all on $La_{0.67}Sr_{0.33}MnO_3$ side) are shown.

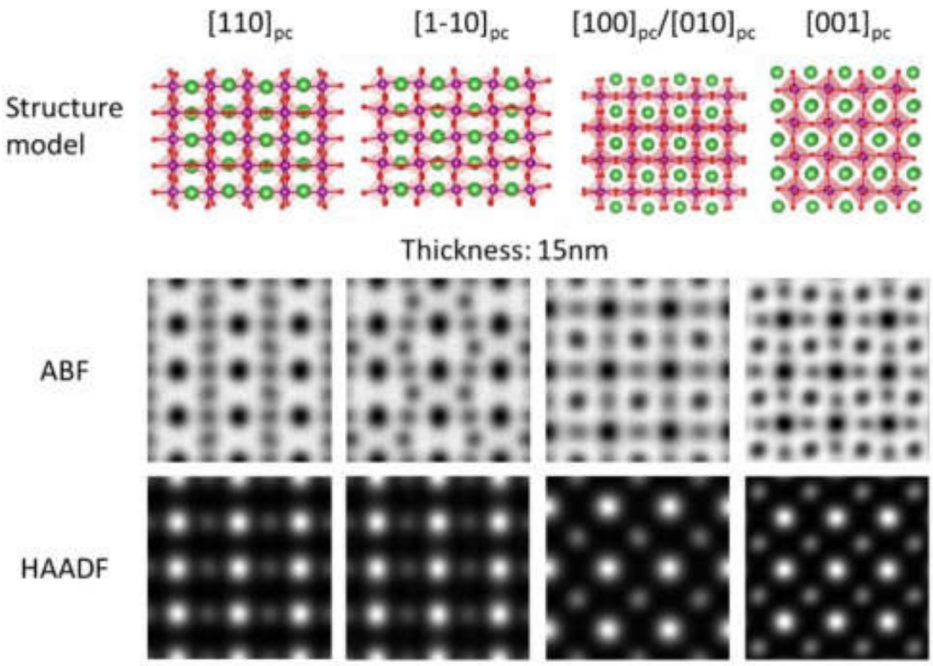

Figure 6.17: The simulation image of HAADF and ABF images in different direction. The figure is taken from Ref. [12] .

HAADF image (fig.6.18a), from which the out-of-plane (OOP) lattice constant is calculated. The OOP lattice constant as a function of distance from interface is plotted in fig.6.18c. The blue and red solid lines show the bulk lattice constant of $La_{0.67}Sr_{0.33}MnO_3$ and $SrTiO_3$, respectively. The $SrTiO_3$ lattice constant preserves its bulk value, while on the other hand $La_{0.67}Sr_{0.33}MnO_3$ shows a peculiar behavior for OOP lattice constant. The first two unit cells near the interface, shaded in yellow, show an unusual elongation, 3.92 ± 0.056 Å and 3.922 ± 0.056 Å, respectively. This is counter-intuitive considering the fact that the thin film is under tensile strain. Similar behavior was observed in other very recent reports [12, 119]. Away from the interface, the OOP lattice constant contracts (relaxes) to a smaller value which on average agrees well with XRD measurement. Fig.6.18b shows the STEM-ABF image of $La_{0.67}Sr_{0.33}MnO_3/SrTiO_3$ (001) where the position of oxygen atoms is resolved. The zig-zag pattern of oxygen atoms is visible where it begins from the interface and continues to the surface. Fig.6.18d presents the

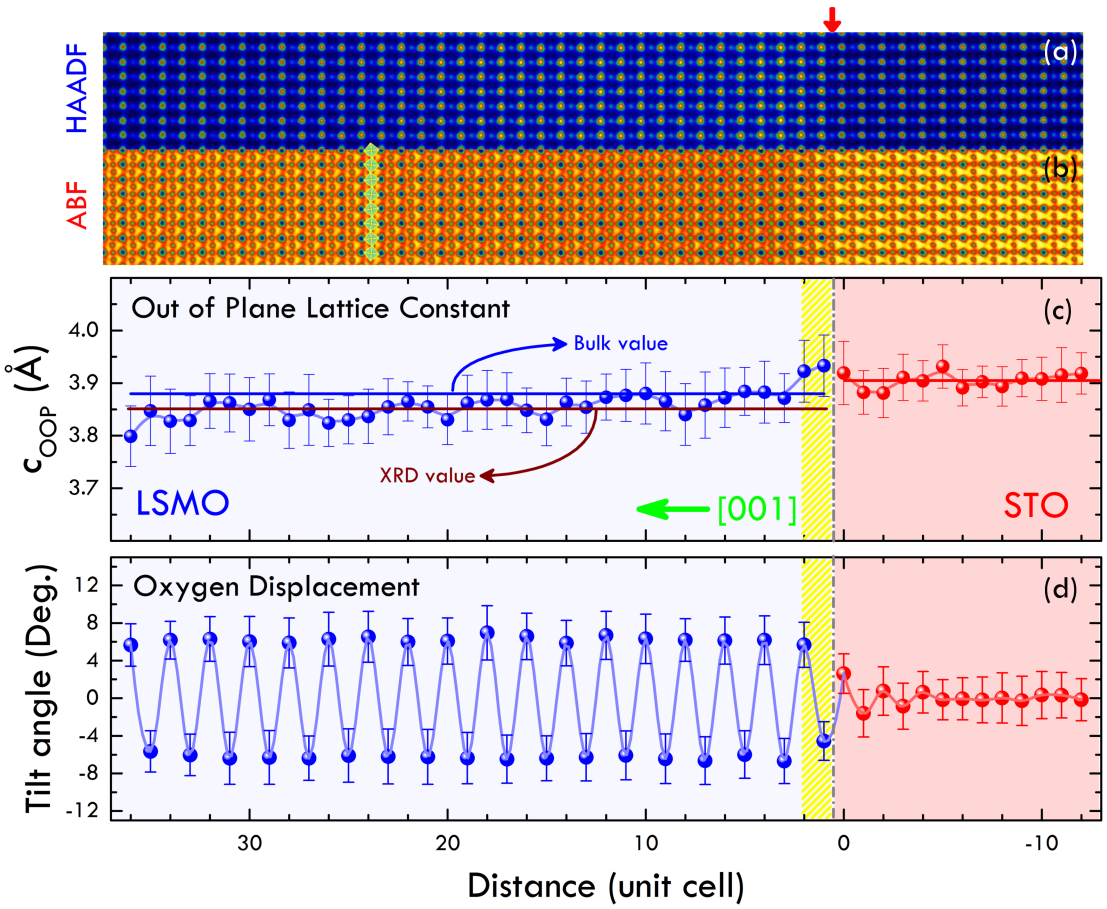

Figure 6.18: a) The STEM-HAADF and b) STEM-ABF image. The interface is marked by the red arrow. c) OOP lattice constant of substrate and thin film. The first two unit cells, highlighted in yellow show and unusual elongation of OOP lattice constant. To compare OOP lattice constant with bulk and measured XRD value two solid lines are drawn. Away from interface, the thin film shows contraction of OOP lattice constant. d) OOT angle as a function of unit cell distance from the interface. The first unit cell shows suppression of OOT. Also, the OOT is induced in $SrTiO_3$ where it diminishes over a distance of four unit cells.

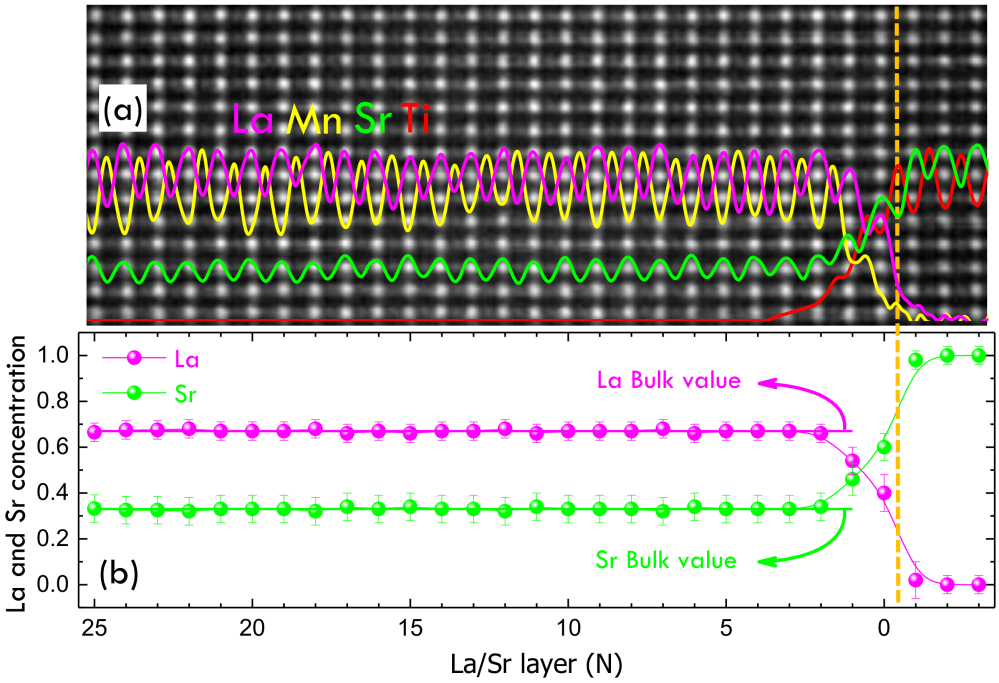

Figure 6.19: The concentration of STEM-EELS for La, Sr, Mn and Ti as a function of distance from interface. About one unit-cell of intermixture is observed. b) The stoichiometry of La and Sr across the interface. One unit-cell from interface, the La and Sr recover their bulk values of 0.67 and 0.33, respectively.

oxygen octahedral tilt (OOT) as function of distance from the interface. The top 4 uc of $SrTiO_3$ show a decaying OOT where $SrTiO_3$ recovers its $a^0a^0a^0$ tilt pattern. In the same way, first two unit cells of $La_{0.67}Sr_{0.33}MnO_3$, shaded in yellow, shows a suppressed OOT of 4.5° and 5.6°, respectively. From the third unit cell, $La_{0.67}Sr_{0.33}MnO_3$ retains its relaxed OOT value, 6.1° which is close to the bulk value 6.8° [120]. The suppression of OOT near the interface as well as elongation of OOP lattice constant show the structural response to the broken symmetry at the interface.

The layer-by-layer stoichiometry of the thin film was measured using electron energy loss spectroscopy (STEM-EELS). Fig.6.19a shows the EELS elemental mapping as a function of distance from the interface and fig.6.19b shows the Sr and La concentration for each layer is calculated from their respective EELS spectra. The interface intermixture is confined within the first unit cell and after second unit cell the thin film recovers the stoichiometric bulk value which is $La_{0.67}Sr_{0.33}MnO_3$. Given the Sr excess in the first La/Sr row at the interface, the Mn oxidation state deviates from bulk value. The ratio of Mn L_2 and L_3 edge show that the oxidation state of Mn near the interface is lower than the rest of the thin film, changing the balance of Mn^{4+}/Mn^{3+} in favor of Mn^{3+}. This observation agrees with the elongation of OOP lattice constant and suppression of tilt near the interface due to larger ionic radii of Mn^{3+} comparing to Mn^{3+}.

6.3 Summary

In summary, we have shown that broken symmetry at the interface can result in emerging of magnetic properties in the manganite thin films. The electronic and structural symmetry mismatch results in lattice and charge modification which changes the exchange interaction near the interface and in effect, an AFM interaction is stabilized near the interface which spontaneously reverses the magnetic moment and creates inverted hysteresis which persists well above room temperature. Our results show that taking advantage of heterstructures with symmetry mismatch can lead to new function-

alities. Engineering the broken symmetry driven interactions at the interface can be an effective pathway toward fabrication of new functional devices, specially magnetic switching devices.

Chapter 7
Manipulating physical properties of $La_{1-x}Sr_xMnO_{3-\delta}$ through processing

7.1 Introduction

In the previous chapter, it was shown that the physical properties of $La_{0.67}Sr_{0.33}MnO_3$ as well as its parent compounds are a strong function of processing procedure during growth where oxygen pressure or stoichiometry plays an important role. In this section, the oxygen pressure is systematically changed while other growth parameters are held the same.

Change in oxygen pressure plays two important roles,

- Change the growth dynamic. The interaction of laser plume with the oxygen atoms will lead to a different instantaneous deposition rate and kinetic energy of atoms/ions reaching the surface of substrate. This will alter supersaturation condition and interlayer mass transport.

- Change in stoichimetry. Presence of Oxygen deficiency will modify the physical properties of material. Presence of vacancies in the initial stages of growth might change the strain relief mechanism.

In the following, the physical properties of thin film grown in different oxygen pressure is studied. We will show that there is a critical oxygen pressure where a new phase near the interface emerges and alters the magnetic properties of $La_{1-x}Sr_xMnO_3$.

7.2 Growth parameters

The thin films of $La_{1-x}Sr_xMnO_{3-\delta}$ from a $La_{0.67}Sr_{0.33}MnO_3$ target are grown using pulsed laser deposition method (PLD) under different oxygen pressures. In this method, high kinetic energy and high instantaneous deposition rate are two important factors.

Both of them are affected by changing oxygen pressure. It has been shown that the physical properties of thin films depend on laser fluence and repetition rate, the general consensus is that the lower repetition rate will lead to a more stoichiometric thin film growth with optimized physical properties. It was shown that the repetition rate of 1 Hz leads to optimized growth condition for $La_{0.67}Sr_{0.33}MnO_3$ [110]. Another usual practice in thin film growth is heating the substrate in the presence of oxygen, i.e., first bringing the oxygen pressure to the desired setpoint and then heating the substrate to target temperature. Here, I will abandon both of these practices to create a condition for growth of metastable phases.

The stoichiometric target is shined with laser pulses with 248 nm wavelength with fluence of 2 J/cm[21]. The repetition rate was set to 10 Hz. The thin films are grown on $SrTiO_3$ substrate. Prior to growth the substrate was brought to 660 °C in vacuum of 1×10^{-8} Torr. The idea is to remove any contamination and increase the Ti^{3+}/Ti^{4+} ratio. It will be shown that can lead to creation of a La^{3+} region near the interface that alters the magnetic properties.

The growth mode is monitored using RHEED and the thickness is controlled by number of RHEED oscillations. Fig.7.1a shows the RHEED oscillations for 50 uc LSMO thin film. The RHEED intensity increases in the first ten unit cells in a transient fashion and after that the intensity of oscillation stabilizes. The enhanced intensity is related to stronger reflection of heavier atoms in the first few unit cells. Transmission electron microscopy shows that the enhanced intensity is indeed due to a La-rich region region near the interface. The fig.7.1a inset shows the RHEED pattern before and after the growth. The streak-like pattern after growth confirms the quasi 2 dimensional growth and smoothness of the surface.

[1]Usually the laser fluence is measured at a position outside growth chamber and the energy per area is estimated by the illuminated area on the target. Author's experience say focus of the laser on the target is important as it determines the shape of the plume. It is seen that it is better if the sample is positioned barely inside the crown of the plume.

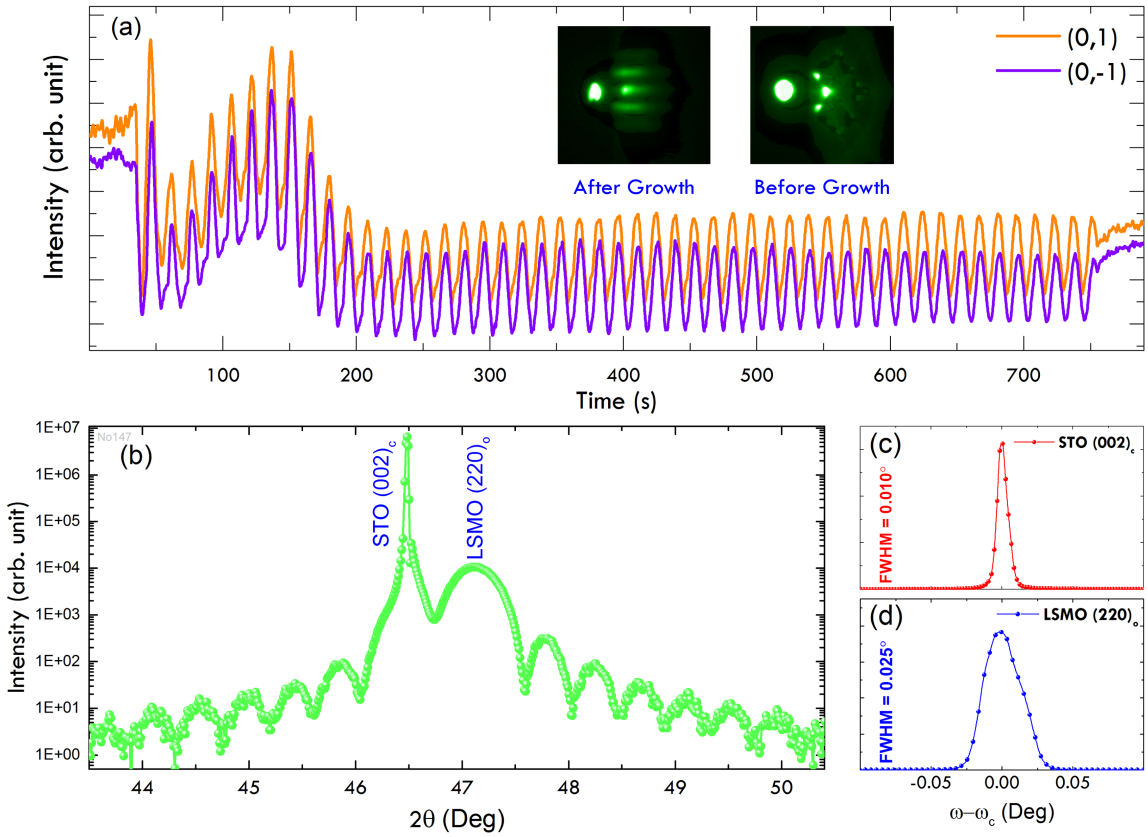

Figure 7.1: a) RHEED oscillation of 50 uc LSMO thin film is shown. Inset shows the RHEED pattern before and after the growth. From 2nd un to 10th uc there is a RHEED intensity enhancement which is due to more reflection from more concentration of heavier atoms. b) $\theta - 2\theta$ coupled XRD measurement around STO $(002)_C$ and LSMO $(220)_O$. c,d) The rocking curve for STO and LSMO with FWHM of 0.010° and 0.025°, respectively.

7.3 Structure: Macroscopic and microscopic

In this section the structure of $La_{1-x}Sr_xMnO_{3-\delta}$, i.e. LSMO grown under non-equilibrium[1], non-optimized[2] condition, is studied. Two methods are used to access the structural information on $La_{1-x}Sr_xMnO_{3-\delta}$, XRD and STEM (HAADF, ABF). First, the XRD data are discussed and then TEM images are presented.

Fig.7.1b shows the $\theta - 2\theta$ XRD scan of $La_{1-x}Sr_xMnO_{3-\delta}$ around $SrTiO_3$ $(002)_C$ and $La_{1-x}Sr_xMnO_{3-\delta}$ $(220)_O$. The presence of Kiessig oscillations show that the surface and interface are smooth. The substrate and layer peak positions are at 46.48° and 47.10° which corresponds to out of plane lattice constant of 3.905 Å and 3.857 Å, respectively. The out of plane lattice constant of thin film is smaller than the substrate which is due to tensile strain. However, it is larger then the optimally grown $La_{0.67}Sr_{0.33}MnO_3$ which its lattice constant was shown to be 3.846 Å. To access crystallinity of the thin film, the rocking curve (ω scan) for substrate and layer is shown in fig.7.1c and d. The substrate and layer FWHM values are 0.010° and 0.025°, respectively. The small value of FWHM show that there are almost no mosaicity, dislocation or other forms of defect present in the thin film and on a macroscopic level it is coherently grown with substrate.

To better see the effect of oxygen pressure on the structure of the thin films, the $\theta - 2\theta$ scan as a function of oxygen pressure is shown in fig.7.2a. All thin films show smooth surface and interface which indicates high growth quality. Fig.7.2b shows the change of out of plane lattice constant as a function of oxygen pressure. It is well-known that lower oxygen pressure, which promotes oxygen vacancies will increase the out of plane lattice constant. This behavior is clearly seen. As the oxygen pressure decrease, the out of plane lattice constant increases. Oxygen pressure below 40 mTorr shows a jump in lattice constant. These samples are grown using the conventional growth

[1]Here non-equilibrium means a condition that can lead to a different structure comparing with the target, $La_{0.67}Sr_{0.33}MnO_3$.

[2]Non-optimized refers to a condition that is not set for achieving optimal physical properties, rather it is set for creating new interactions.

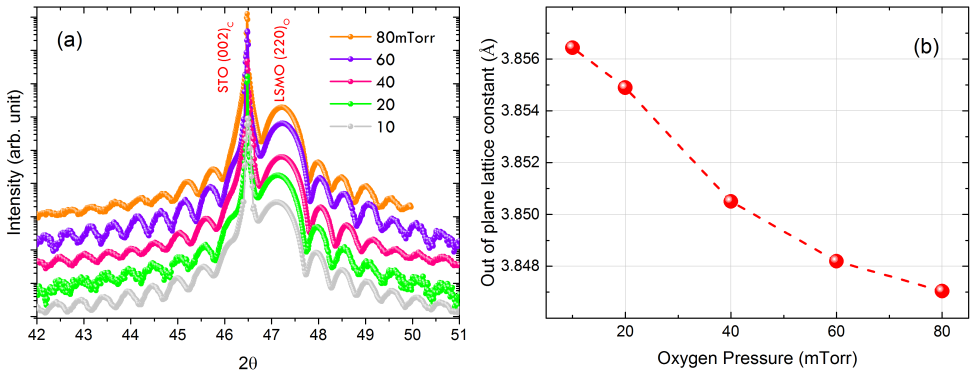

Figure 7.2: a) $\theta - 2\theta$ XRD scan of LSMO thin films as a function of oxygen pressure. b) The out of plane lattice constant as function of oxygen pressure. As expected, the lattice constant increases with decreasing (increasing) oxygen pressure (oxygen vacancy).

condition to just show the effect of oxygen vacancy. Using non-equilibrium conditions, at 40 mTorr, the c-axis will be even larger (3.857 vs 3.850 Å). It will be shown that at 40 mTorr pressure, a new magnetic interaction emerges where changes the functionality of the the monolithic $La_{1-x}Sr_xMnO_{3-\delta}$.

Similar to section 6.2.2, reciprocal lattice mapping of an $La_{1-x}Sr_xMnO_{3-\delta}$ thin film grown in 40 mTorr oxygen pressure is studied. The thin film is fully strained and preserves its four fold in-plane symmetry. The substrate peak is elongated which is due to lack of a crystal analyzer on the detector side. The thin film peaks for $(620)_O$ and $(44-4)_O$ are shifted down comparing to the other two RLMs. Since the whole RLM is shifted, it is due to the limited alignment accuracy of XRD machine. The change in lattice constant due to this effect is way below standard deviation of our measurement. Table7.1 shows the values of interpalnnar distance for different Bragg peaks. The difference between d_{204} and d_{-204} is 0.0004 Å which is one order of magnitude smaller than standard deviation of the measurement[1].

In order to understand the structure on the microscopic level, STEM-HAADF and STEM-ABF images were studied. Fig.7.4a shows the HAADF and ABF images of

[1]In another word, this value is smaller than the step sizes of the measurement. In some references all RLMs are corrected with respect to substrate peak to avoid this issue.

Table 7.1: Summary of RSM of $La_{1-x}Sr_xMnO_3$.

Bragg's peak	ω	2θ	q_x (rlu)	q_y (rlu)	q_z (rlu)	Q(1/Å)	$d_{hkl}(\AA)$	
204	35.3557	123.795	0.5117	0	1.0244	1.1451	0.8732	Sub (cubic)
444	36.8657	12.1986	0.5117	0	1.0385	1.1577	0.8637	Layer (ortho)
$\overline{2}04$	88.4244	123.6909	-0.5121	0	1.0236	1.1446	0.8736	Sub (cubic)
$44\overline{4}$	89.2894	126.9953	-0.5123	0	1.0370	1.1567	0.8645	Layer (ortho)
024	88.4463	123.7020	0	-0.5124	1.0235	1.1446	0.8736	Sub (cubic)
620	89.3863	126.1986	0	-0.5125	1.0383	1.1579	0.8636	Layer (ortho)
$0\overline{2}4$	35.3198	123.7892	0	0.5116	1.0244	1.1451	0.8732	Sub (cubic)
260	36.8332	126.1395	0	0.5116	1.0382	1.1574	0.8640	Layer (ortho)

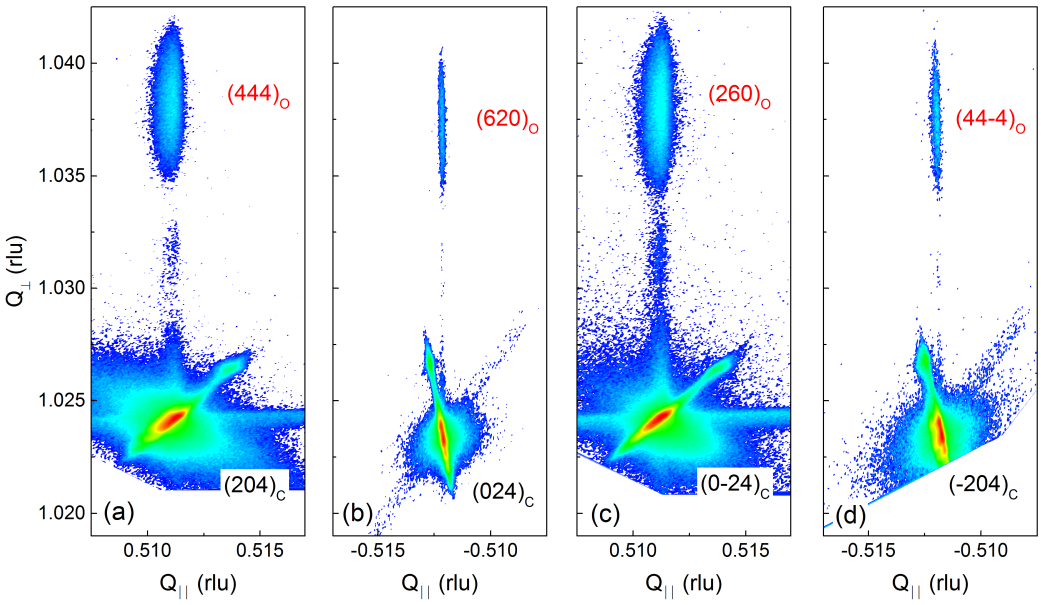

Figure 7.3: Reciprocal lattice mapping.

$La_{1-x}Sr_xMnO_{3-\delta}$ sample which is taken along $[1\bar{1}0]$. The HAADF image is more sensitive to heavy atoms. The contrast of image is directly related to the atomic mass of the element. Thus, La will appear brighter than other elements. The HAADF image shows that the structure is well-ordered and the thin film is coherently grown on the $SrTiO_3$ substrate. The interface does not show any obvious roughening and it is well-defined.

The target in the growth process was stoichiometric $La_{0.67}Sr_{0.33}MnO_3$, however, a self-assembled layer of La-rich LSMO is formed near the interface. This is clearly seen from higher contrast of A-site in HAADF image. By looking at change in the contrast, it is seen that this layer extends from interface to about 7 or 8 uc above interface. Using elemental EELS analysis this point will be discussed further. From HAADF image, the out of plane (OOP) lattice constant is extracted and it is shown in fig.7.4. The first unit cell of thin film shows an elongated OOP lattice constant[1] 3.902 Å and after that it gradually decreases to 3.832 Å and comes back to its bulk value 3.878 Å. The increase in La concentration and decrease in OOP lattice constant are contrary and one cannot

[1]This was seen before in $La_{0.67}Sr_{0.33}MnO_3/SrTiO_3$, although in that case two unit cell elongation was observed.

lead to another. $LaMnO_3$ lattice constant is 3.94 Å [121], therefore more La should lead to elongation of OOP lattice constant. Above the La-rich region, the OOP lattice constant recovers its bulk value. Given that the thin film is under tensile strain, the OOP of the thin film should be less than its bulk value, which again is counter intuitive. The La-rich region constitutes a new layer which is sandwiched between the substrate and the rest of the thin film. Therefore, one can define a new artificial interface which is between La-rich region and the rest of thin film.

Fig.7.4a and c show the ABF image and the extracted tilt pattern, respectively. ABF image is sensitive to light elements which enables resolving of oxygen atoms. As shown in fig.7.4c, the oxygen octahedra tilt (OOT) is shown. The La-rich region shows an enhanced tilt angle which slowly damps as a function of distance. The appearance of OOT justifies the decrease in OOP lattice constant. Shrinking OOP lattice constant will induce more tilt. Another factor responsible for increasing OOP lattice constant is oxygen deficiency as it reduces the oxidation state of Mn which leads to increase in unit cell volume, since the in-plane lattice constant is locked to the substrate, then the OOP lattice constant increases.

7.4 Stoichiometry: $La_{1-x}Sr_xMnO_{3-\delta}$

In the previous section it was shown that there are two main regions in the thin film where the structure is not the same. Here, we study the stoichimetry of the thin film in the two regions. Fig.7.5 shows the electron energy loss spectroscopy (STEM-EELS), mapped on the HAADF image. The oscillation of EELS signal shows that the thin film is well-ordered and coherent. The natural interface is Ti terminated. The Ti intermixture is limited in the first two unit cells. The first and second unit cell have 50% and 15% Ti intermixture. After the first two unit cells, the La concentration exceeds the nominal bulk $La_{0.67}Sr_{0.33}MnO_3$ concentration and around 8th uc it returns to the bulk value. At its peak, La concentration rises to 0.74 ± 0.04 and in an opposite fashion, Sr

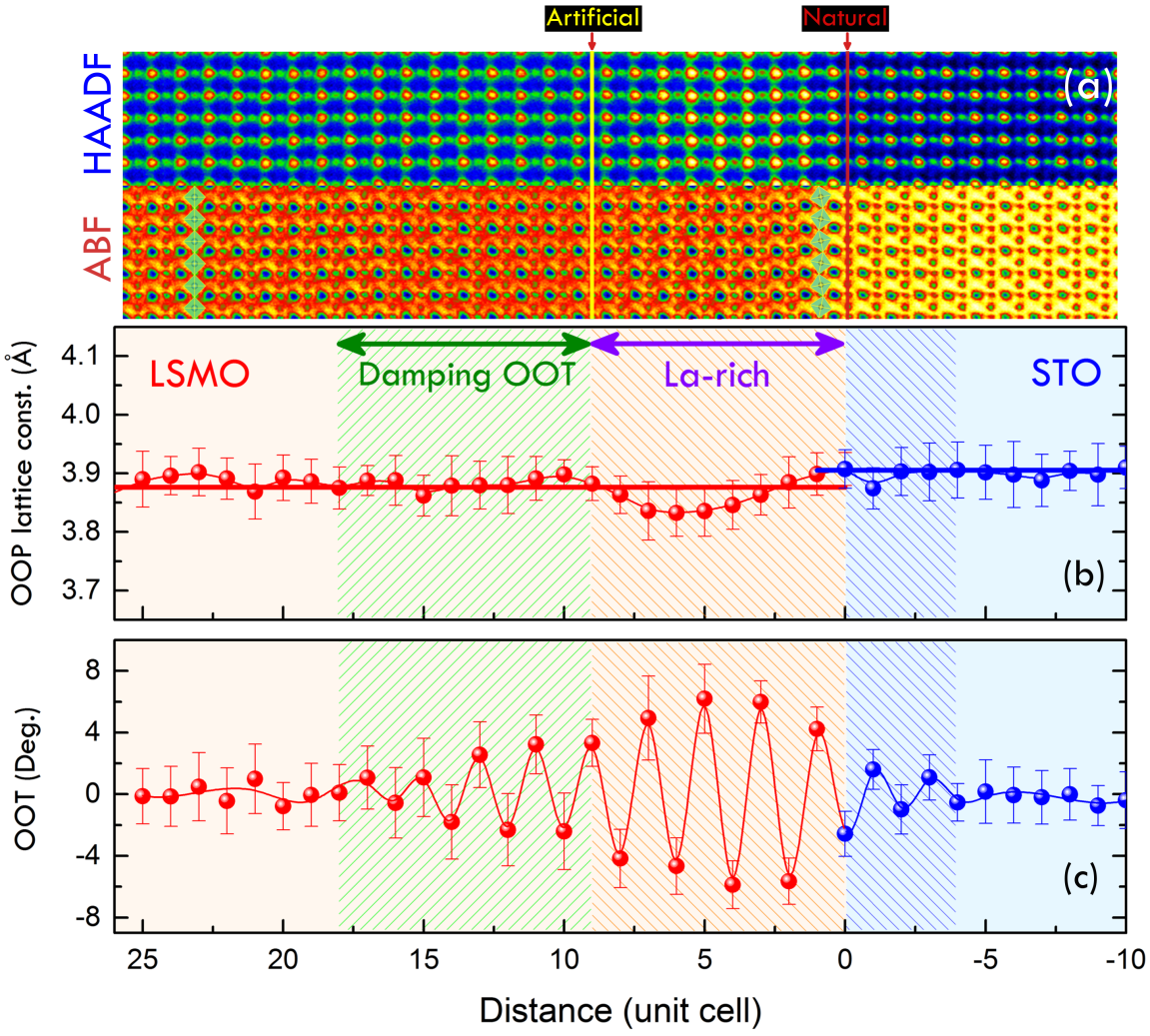

Figure 7.4: a) The HAADF and ABF image of $La_{1-x}Sr_xMnO_{3-\delta}$ is shown. Two interfaces are marked. The natural interface is between LSMO and STO while the artificial interface is between two self-assembled LSMO layers. Between natural and artificial interface there is a region where the thin film is La-rich. It is seen from the higher contrast in HAADF between two interfaces. b)OOP lattice constant across the substrate and thin film is shown. The solid red and blue lines show the bulk OOP of $La_{0.67}Sr_{0.33}MnO_3$ and $SrTiO_3$, respectively. The OOP after natural interface shows a dip where it drops from its bulk value, while it recovers the bulk value above the artificial interface. c) The OOT across the substrate and interface is shown which is derived from ABF image. The

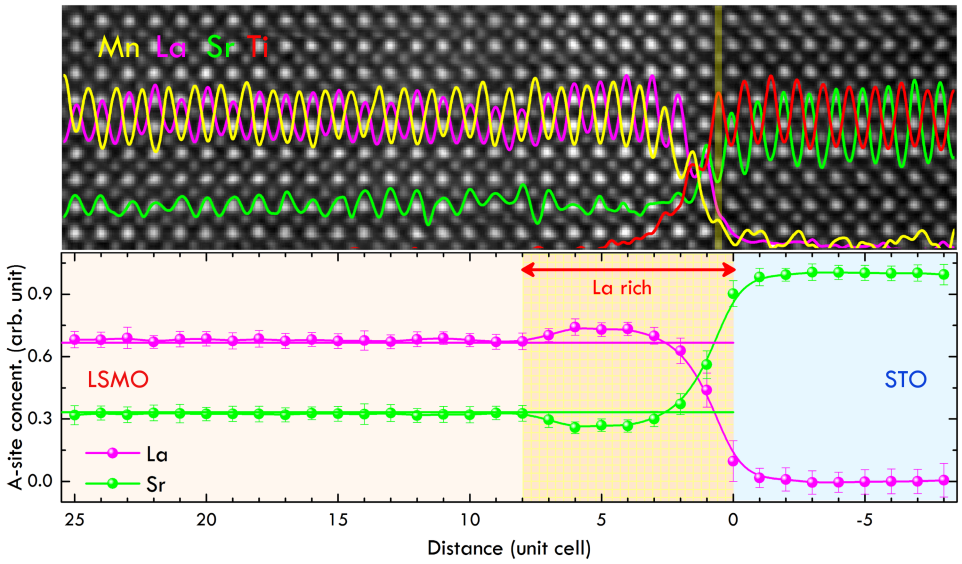

Figure 7.5: a)STEM-EELS elemental mapping. The Ti signal drops to 50% and 15% in the first two unit cells, respectively. b) The A-site concentration as a function of thickness for La and Sr. The La-rich region is marked.

concentration drops to 0.26 ± 0.03. After the artificial interface (La-rich region), the La and Sr concentration slightly deviates from stoichimetric value. Fig.7.6 shows the EELS at core level edges of Ti, Mn, Sr and La where shows the spacial distribution of atoms. The La-rich area is better seen in this figure. It is seen that the thin film, chemically, is divided to two regions which maps on the structure, La-rich region has a different structure comparing to the rest of the film.

7.5 TEM: Electronic properties

Using electron energy loss spectroscopy (STEM-EELS), the oxidation state of Mn is studied. Fig.7.7a shows the Mn L-edge EELS spectra starting from the interface to the 18th layer. The Mn L-edge of bulk $La_{0.67}Sr_{0.33}MnO_3$ is shown as a reference. Comparing to bulk, all spectras show a shift to lower loss energy which means the oxidation state of Mn less than the bulk value. The Mn L-edge spectra of first layer shows a further reduction in comparison to the rest of the thin film.

The Mn oxidation states was determined by calculating Mn L_{23} ratio. The L_{23} ratio decreases as the increase of Mn oxidation state. The quantitative relationship

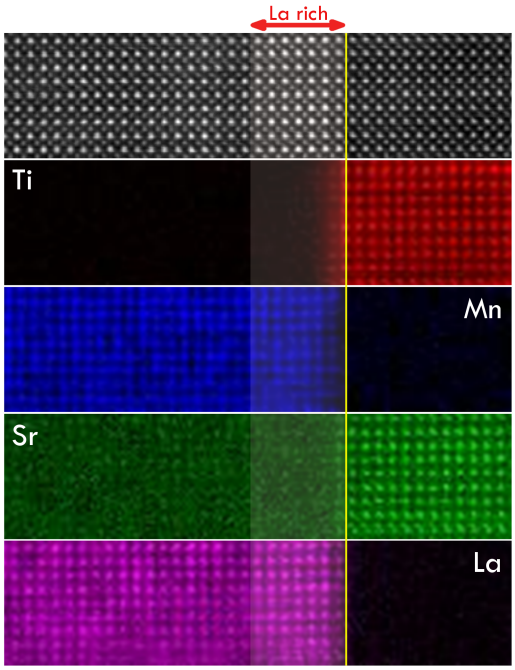

Figure 7.6: The STEM-EELS signal for Ti, Mn, Sr and La. The La-rich is seen where the La signal is stronger.

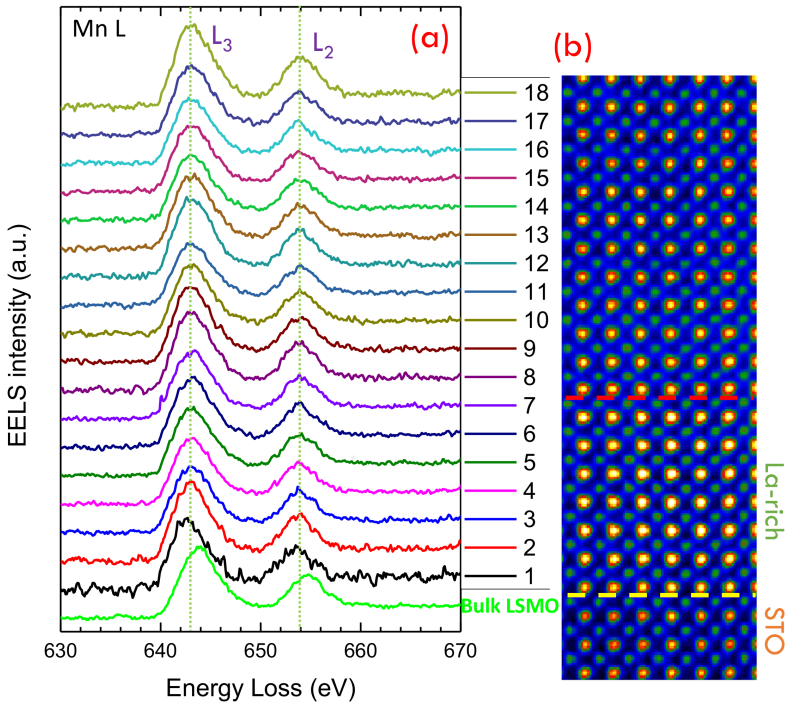

Figure 7.7: a) The EELS spectra of Mn L-edge for each layer. The bulk $La_{0.67}Sr_{0.33}MnO_3$ is shown as a reference. b) The HAADF image shows the layers from which the spectra was extracted.

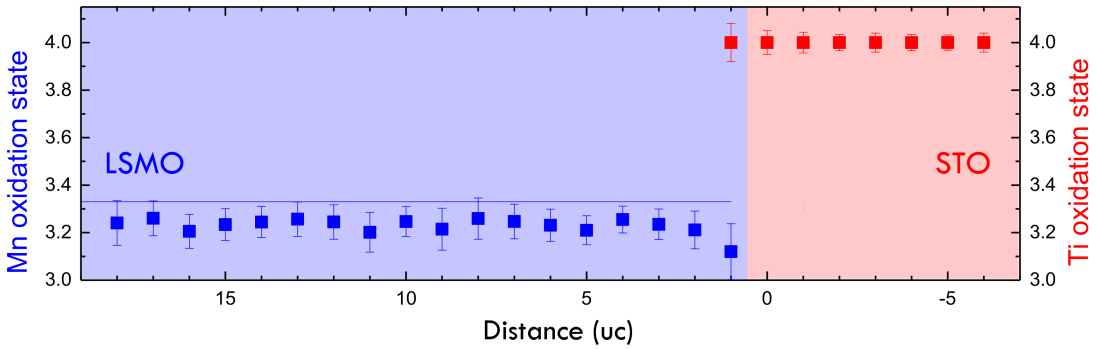

Figure 7.8: The Mn and Ti oxidation state as a function of distance from the interface.

between the L_{23} ratio. Furthermore, the Mn oxidation state was further calibrated by the standard LSMO sample. The Mn L edge results from excitations of 2p electrons into empty 3d band and the continuum. The L_3 edge corresponds to $2p_{3/2}$ to 3d excitation, and the L_2 edge attributes $2p_{1/2}$ to 3d excitation. In general, the Mn oxidation states in $La_{1-x}Sr_xMnO_{3-\delta}$ can be considered as a mixture of Mn^{4+} and Mn^{3+}. The intensity ratio of L_3 to L_2 edges decreases as the oxidation state of Mn increase from 3+ to 4+ [122]. Fig.7.8 shows the oxidation state of Mn and Ti as a function of distance from the interface. As it was seen from EELS spectra, the Mn from the first layer shows a more reduced oxidation state and after that the Mn oxidation state reaches the average Mn oxidation state of +3.26 which is close to the +3.33 bulk value. On the other hand, Ti, preserves its +4 oxidation state regardless of distance from the interface. Reduced Mn oxidation state promotes superexchange magnetic interaction over double exchange. This will be shown to modify the magnetic properties of $La_{1-x}Sr_xMnO_{3-\delta}$.

7.6 Transport properties

Fig.7.9a shows the resistivity as a function of temperature which is measured using four probe method. The resistivity curves show an upturn at very low temperature which is due to localization coming from presence of oxygen vacancies. As the thickness increases the localization effect decreases. It is seen that the metal-to-inslator transition (MIT) temperature decrease which decreasing thickness. 10 and 30 uc thin films show

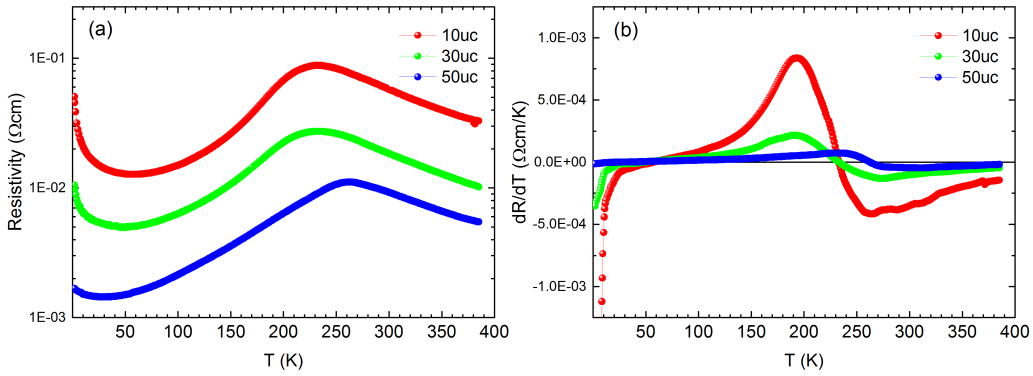

Figure 7.9: a) The resistivity as a function of temperature for three thicknesses is shown. b) The derivative of resistivity with respect to temperature shows the MIT transition for three thicknesses.

an almost equal transition temperature and the 50 uc thin film shows a higher transition temperature, as seen in fig.7.9b. Usually, the MIT and FM transition coincide, however, except for 10 uc thin film, the 30 and 50 uc deviate from this rule. The Curie temperature from magnetic measurement, for 30 and 50 uc thin films is much higher. The reason is due to existence of a magnetically active layer near the interface. Since in four probe measurement, the electrical contacts are on the surface, it is not possible to accurately comment on electrical transport properties of layers near the interface in 30 and 50 uc.

7.7 Magnetic properties

The TEM images showed that the thin film is changed from a monolithic $La_{0.67}Sr_{0.33}MnO_3$, to a two layer $La_{1-x}Sr_xMnO_{3-\delta}$. The magnetic properties of manganites are closely connected to their stoichiometry. As it was shown in fig.6.1, the magnetic properties changes drastically with varying doping level, therefore, one would expect that the magnetic properties of LSMO with artificial interface should deviate from normal $La_{0.67}Sr_{0.33}MnO_3$. In section 6.2.4, it was shown that $La_{0.67}Sr_{0.33}MnO_3$ is a soft ferromagnet with coercivity of 11 Oe. Also, near the interface, broken symmetry will lead to new interactions that manifest themselves in spontaneous magnetic reversal and inverted hysteresis. Similar phenomena happens for $La_{1-x}Sr_xMnO_{3-\delta}$ as well with the addition of considerably larger coercivity and appearance of exchange bias.

Several $La_{1-x}Sr_xMnO_{3-\delta}$ thin films were grown and they were sorted according to their magnetic properties. The magnetic properties are very sensitive to the amount of oxygen vacancy and local distortion of octahedra. Also, thickness is another important factor that can change magnetic properties. The effect of oxygen vacancy and thickness on magnetic properties of $La_{0.67}Sr_{0.33}MnO_3$ has been studied before, although not systematically. But the general consensus is that oxygen vacancy strongly deteriorates magnetism [123]. Here a systematic study of magnetism in $La_{1-x}Sr_xMnO_{3-\delta}$ thin films as a function of thickness and oxygen pressure (as a cruel measure of oxygen vacancy) is presented. Fig.7.10 shows magnetic coercivity and exchange bias as a function of oxygen pressure and thickness. At 40 mTorr and above 20 uc, the coercivity starts to increase drastically. Given the bulk coercivity of $La_{0.67}Sr_{0.33}MnO_3$ is 11 Oe, in $La_{1-x}Sr_xMnO_{3-\delta}$ it can reach to 766 Oe, enhanced by a factor of 70. At the same time, exchange bias appear as well. Its maximum value that we found was at 40 mTorr and 40 uc which was 625 Oe. This shows that controlling the growth parameters enables us to take advantage $La_{1-x}Sr_xMnO_{3-\delta}$ phase diagram to achieve new functionalities. In the following we focus on the spots in phase diagram with exchange bias and enhanced coercivity.

The magnetization vs temperature for a 50 uc LSMO thin film which was grown under 40 mTorr oxygen pressure is shown is fig.7.11. In fig.7.11a, the sample was cooled down to 2 K, under zero magnetic field then the measurement was performed during warm up under different magnetic fields. In fig.7.11b, the sample was cooled down to 2 K under 1000 Oe magnetic field and the measurement was carried out under various magnetic field during warm up.

There are two important features in this figure. First, there are two onsets of FM. One starts around 330 K and the other begins at 250 K. Second, there is a magnetic reversal which depends on external magnetic field (Zeeman[1] energy). Applying a stronger

[1]Pieter Zeeman 1865-1943. Awarded 1902 Nobel Prize "in recognition of the extraordinary service they rendered by their researches into the influence of magnetism upon radiation phenomena"

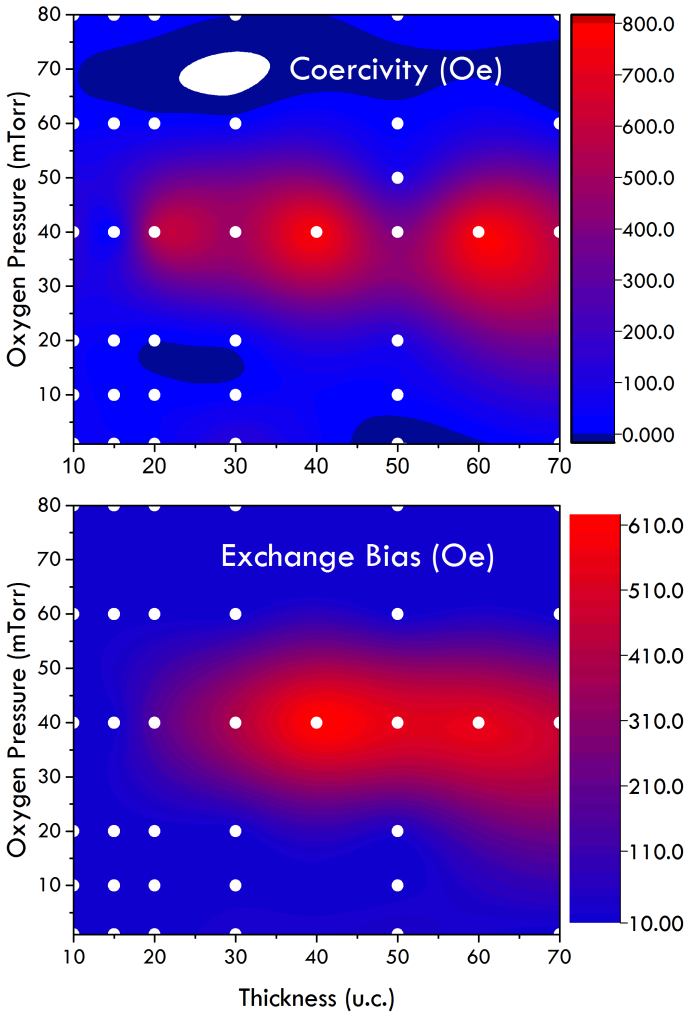

Figure 7.10: The phase diagram of magnetic coercivity and exchange bias at 2 K is shown as a function of thickness and oxygen pressure. Around 40 mTorr and above 20 uc, the magnetic phase of intereset emerges where shows exchange bias and enhanced coercivity.

magnetic field during measurement will result in occurrence of magnetic reversal at lower temperature. Zeeman energy is competing with FM exchange and thermal energy. Since LSMO is a very soft FM and the mangetic moments lie in easy axis direction, it is reasonable to assume domain walls contribution at low temperature is negligible comparing to Zeeman energy.

The TEM data (fig.7.4) showed that the thin film has three main regions.

- First, the first unit cell shows elongation of OOP lattice constant. This was shown in the section 6.2.4 to couple antiferromagnetically to the rest of thin film (A/FM-0).

- Second, La-rich region with strong tilt. The stoichiometry of this portion of the thin film shows that it is a FM. The 6-7 uc thickness of this layer, suggest that it is responsible for the first onset of FM (FM-1).

- Third, the rest of thin film after La-rich region. In this region the stoichimetry fluctuates around the nominal value, while the structure does not show any tilt and OOP is around the bulk value for $La_{0.67}Sr_{0.33}MnO_3$. This portion of the thin film is responsible for the second onset of FM (FM-2).

Magnetic reversal under two mangetic field trainings and their respective schematic magnetic interactions are shown in fig.7.12a-d. In figure 7.12a the sample is cooled to 2 K under no magnetic field and the magnetic moment is measured during warming with 5 Oe magnetic field. Fig.7.12c, shows schematic behavior magnetic moments as function of temperature under this field training. At 2 K, initially the FM-1 and FM-2 are pointing in the same direction while coupled to A/FM-0 antiferromagnetically. Turning on the mangetic field H and increasing the temperature will result in the alignment of magnetic moments with the external magnetic field. FM-2 slowly decrease as temperature increase which is due to first, external magnetic field and second increasing temperature that

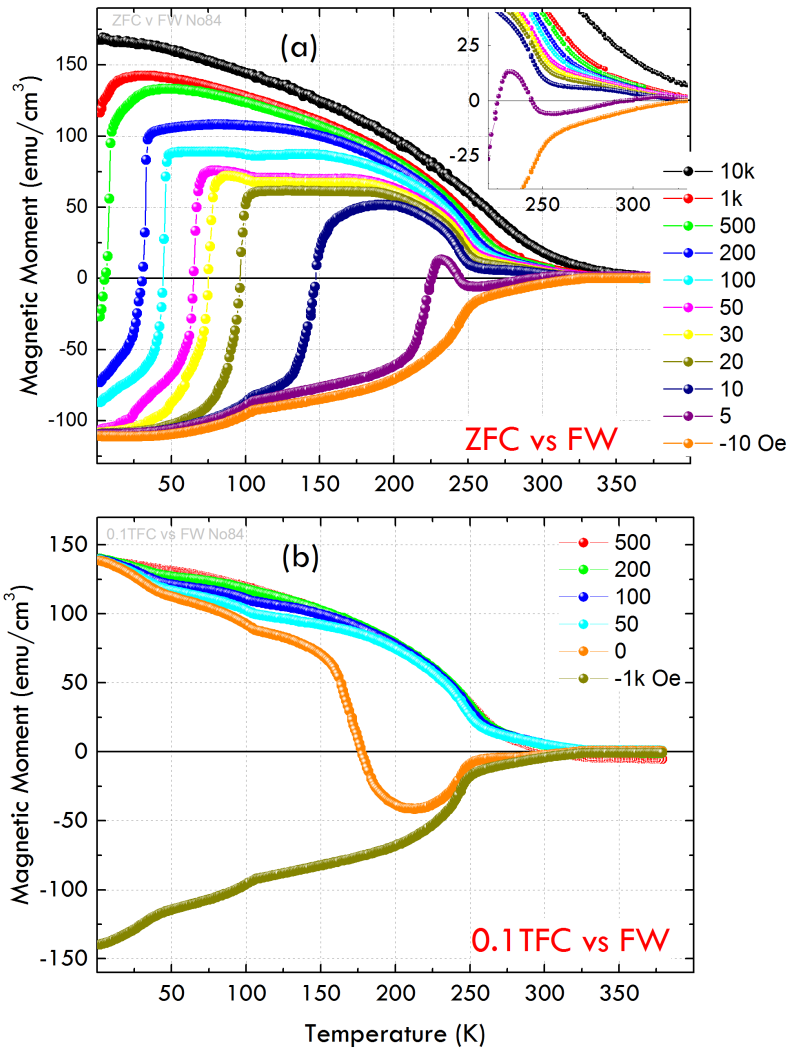

Figure 7.11: Magnetization vs temperature of 50 uc LSMO thin film grown in 40 mTorr oxygen pressure. a) The sample is cooled to 2 K under zero mangnetic field and then measurement was performed during warm up under different magnetic fields. The inset shows the onset of magnetism, also it shows how gradually the magnetic moment reverses. b) The sample was cooled down to 2 K under 1000 Oe magnetic field and the measurement was carried out under various magnetic field during warm up.

promotes thermal fluctuation of magnetic moments. At 225 K, the external magnetic field with the help of thermal energy overcomes the FM coupling of FM-1 and FM-2. As a result, the macroscopic magnetic moment reverses. At 242 K, the FM-2 magnetic moment becomes smaller than FM-1 and the direction of macroscopic magnetic moment reverses again. As shown, FM-1 is locked by A/FM-0 so it does not change its direction. As the temperature crosses 250 K, FM-2 reaches it Curie temperature and goes through a PM transition. At this point, only FM-1 and A/FM-0 are magnetically active. With further increasing the temperature, the FM-1 magnetic moment becomes smaller, when its magnitude becomes comparable to A/FM-0 and the coupling between FM-1 and A/FM-0 is small enough, the external magnetic field causes another reversal at 304 K. At 328 K, FM-1 crosses its Curie temperature and becomes a PM.

Fig.7.12b shows M-T curve where the sample is cooled to 2 K under 1000 Oe external magnetic field and the measurement is performed during warming under zero magnetic field. Fig.7.12d shows the evolution of each FM layer. Initially, all the magnetic moments are locked (frozen) in the direction cooling field, i.e. pointing in the same direction. As the temperature increases, thermal fluctuation helps to activate (un-freeze) the AFM coupling of A/FM-0 and FM-1 layers. Further increase in temperature on one hand, and the FM coupling of FM-1 and FM-2 on the other hand, reverses the macroscopic magnetic moment of the thin film (around 176 K). At this configuration, FM-1 and FM-2 are now in the opposite direction of setting field (cooling field). At 250 K, the FM-2 layer crosses Curie temperature and becomes a PM. Finally, around 326 K, FM-1 becomes a PM as well. As oppose to ZFC 5 OeFW training, there is no reversal at 304 K. This is due to absence of external field, where it could compete with the effect of thermal fluctuation and help align weakly coupled FM moments.

There are two kinks in fig.7.12b which are indicated by circles, one at 49 K and the other at 105 K. The latter comes from the well-know structural phase transition

of $SrTiO_3$. The former at 49 K is rather less trivial. A similar effect was observed in the previous chapter on $La_{0.67}Sr_{0.33}MnO_3/SrTiO_3$ thin films where a complete reversal was happening at a similar temperature. There are two possible explanations for this kink. One, which was suggested before [116], relates this to compressive structural fluctuation of LSMO where was occuring at 120 K, however this temperature is way higher than 49 K, therefore it cannot be the reason for magnetic reversal observed here. Second, structural fluctuation of substrate might modify the magnetic interaction near the interface and trigger the magnetic reversal. It is known that below 105 K, $SrTiO_3$ goes under a antiferrodistortive cubic to tetragonal transition where a phonon softening starts [124]. Instead of a phase transition, this phonon softening saturates at 40 K which prevent a ferroelectric phase transition in $SrTiO_3$. However, the antiferrodistortive pattern of $SrTiO_3$ can affect the magnetic coupling at the interface. Although no direct experimental evidence in this work is present to support this claim, our observation for $La_{0.67}Sr_{0.33}MnO_3$ shows that there is an onset of AFM coupling at the interface around 50 K. This AFM coupling might appear well below 50 K but at low temperature, the magnetic moments could be frozen and thermal fluctuations are required to assist this magnetic reversal.

In the above argument, it is not clear whether the A/FM-0 is ordered AFM or FM (in-plane) since it is a single layer and probing its mangetic order is close to impossible. However, the two field trainings in fig.7.12 show that the coupling between FM-1 and A/FM-0 should be antiferromagnetic. Also, tensile strain is shown to remove the degeneracy of e_g orbital which will promotes AFM coupling by preferential occupation of $d_{x^2-y^2}$ orbital. Having said this, TEM shows the first unit cell OOP lattice constant is enlarged. This should promote the out-of-plane orbital occupation ($d_{3z^2-r^2}$). There are conflicting experimental results trying to understand interfacial magnetic ordering.

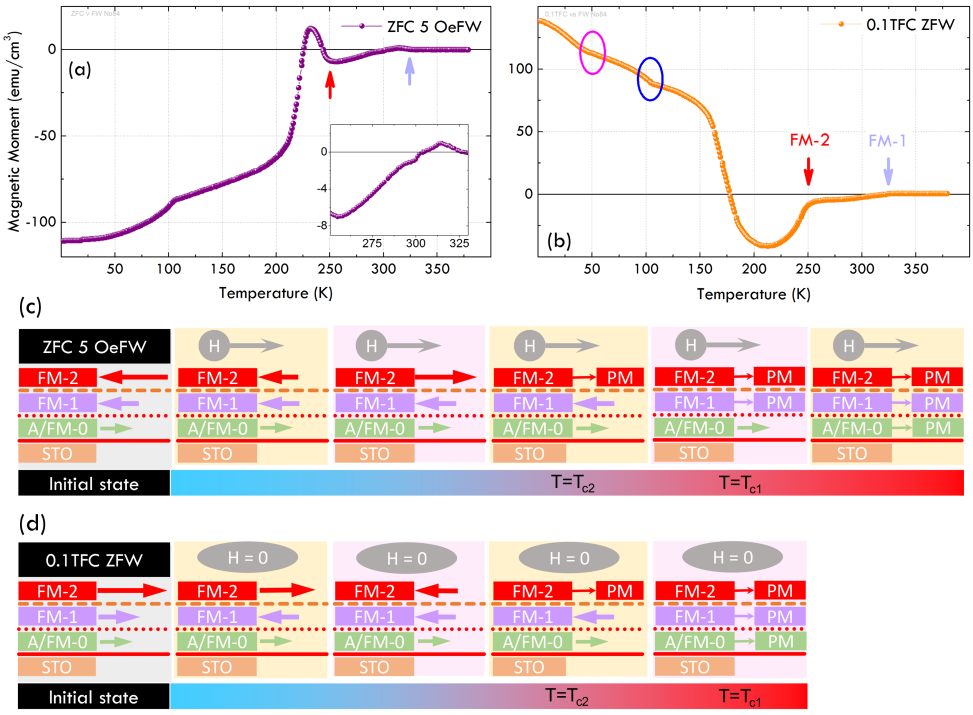

Figure 7.12: a) M-T curve for ZFC 5 OeFW. The inset shows the small magnetic moments at high temperatures. b)M-T curve for 0.1TFC ZFW. The two FM onsets are marked. Circled at 50 and 105 K, there are two kinks which are due to broken symmetry at interface and structural phase transition of $SrTiO_3$, respectively. The 50 K kink is smeared out in part (a) due to presence of magnetic field. c) The schematic magnetic phase as a function of temperature for ZFC 5 OeFW. d) The schematic magnetic phase as a function of temperature for 0.1TFC ZFW.

For example, using XMCD[1] and XLD[2] it was shown that regardless of tensile or compressive strain, the magnetic ordering near the interface will be C-type AFM [125]. In another study [126] with the same technique, it was concluded that throughout the whole $La_{0.67}Sr_{0.33}MnO_3$ thin film, there is a preferential occupation of $d_{x^2-y^2}$ without any orbital reconstruction near the interface. Another study [127], using the same technique showed there is a linear dichroism signature of preferential occupation of $d_{3z^2-r^2}$ orbital where promotes C-type AFM. The issue of magnetic ordering at the interface remains controversial. In the author's opinion, one possible reason for such a discrepancy between the results is the processing. Different groups grow thin films with under different conditions. Although they agree in bulk properties, the fine interactions and structures might vary, such as interfacial magnetic order. As it was shown before, broken symmetry at the interface of $La_{0.67}Sr_{0.33}MnO_3/SrTiO_3$ results in the fine adjustment of magnetic properties. Our data (however indirectly) show that the interface has to couple antiferromagnetically to the rest of the thin film. Our TEM data support this claim as it shows drastic change in the stoichiometry and structure of first unit cell at the interface. Our data underscore the importance understanding the microscopic properties of the complex oxide, such as manganites before making conclusion based on macroscpic data.

To better understand the ferromagnetism in this system, magnetic hysteresis was measured along a M-T curve shown in fig.7.11. Fig.7.13a shows the M-T curve measured under field training of ZFC 50 OeFW. Red arrows show the temperatures at which the ferromagnetic hysteresis is measured. For every ferromagnetic hysteresis, the sample goes through the cycle, i.e. the sample is cooled down in the absence of magnetic field and then warmed up to the target temperature under 50 Oe, then the M-H measurement was carried out. Fig.7.13b-d shows the hysteresis at different temperatures. At 50 K

[1]X-ray magenetic circular dichroism.
[2]X-ray linear dichroism.

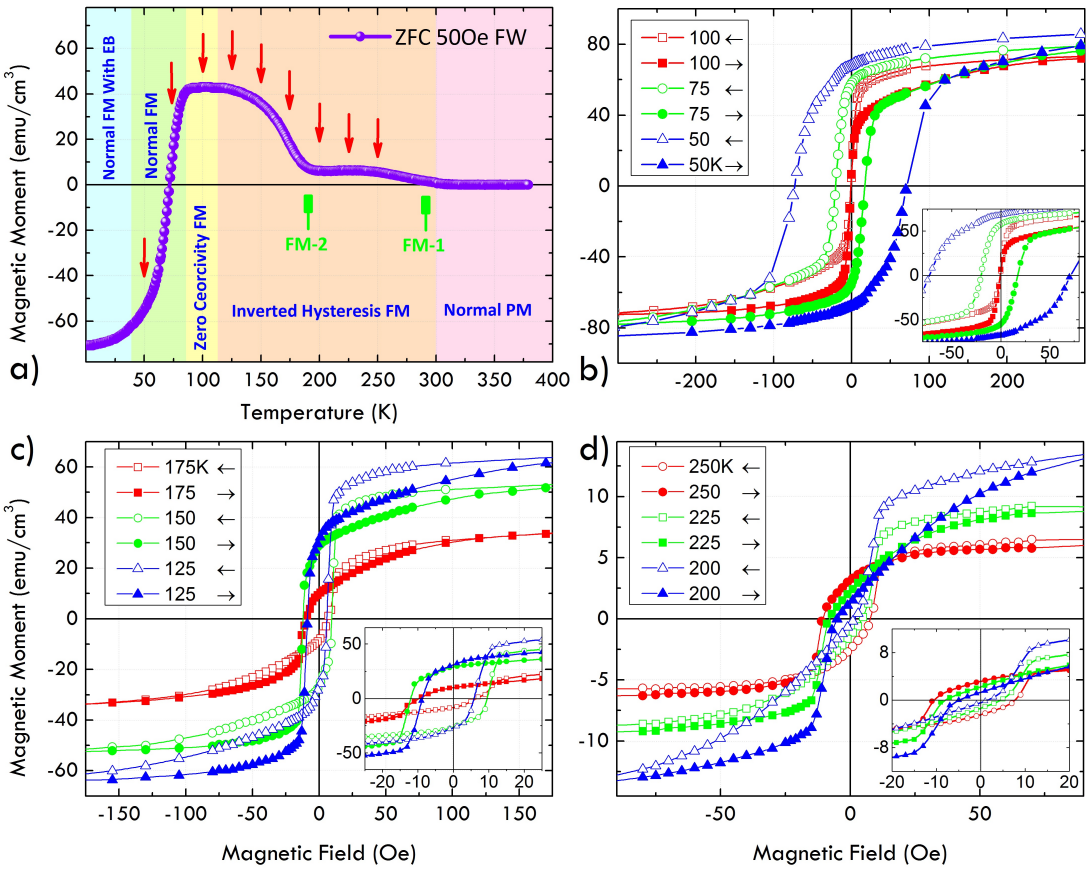

Figure 7.13: a) M-T curve of $La_{1-x}Sr_xMnO_{3-\delta}$. The sample was cooled in the absence of magnetic field from 380 K to 2 K, then it was measured from 2 K to 380 K under 50 Oe magnetic field. The arrows show the points at which the magnetic hysteresis was measured. Two onsets of magnetism, FM-1 and FM-2 are shown. b-d) Magnetic hysteresis as a function of temperature. Sweeping the magnetic field from +1 T to -1 T is shown with empty symbols, while from -1 T to +1 T is shown with solid symbols. The insets magnify the small field regions.

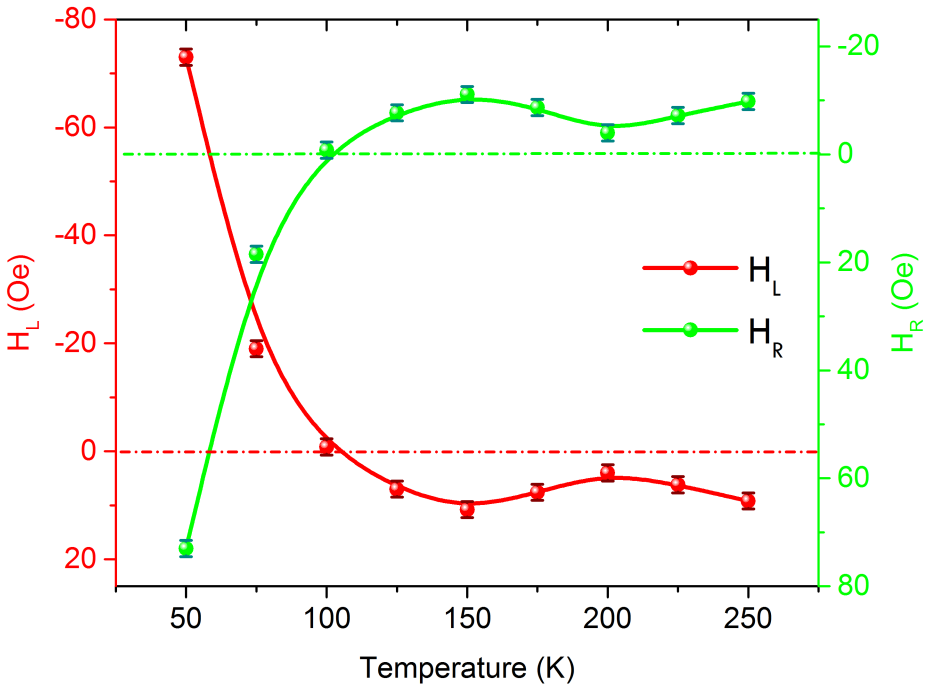

Figure 7.14: Change in left and right coercive field as a function of temperature.

the hysteresis is normal, in the sense that the magnetization changes direction after the direction of magnetic field changes. At 75 K the hysteresis is the normal while the coercivity decreases. The decrease is due to collaborating contribution of thermal activation with Zeeman energy for reversing the magnetic moments. At 100 K, coercivity becomes zero while hysteresis remains non-zero. It means magnetic reversals begins at positive fields and fully develops at zero magnetic field. At 125 K and higher the hysteresis becomes inverted, i.e. left coersive field (right coersive field) is located on the right (left) side of field axis. This means the magnetic moment reverses before reversing the magnetic field. This is another indirect indication of presence of AFM coupling the material. The change in left and right coercive field as a function of temperature is shown in fig.7.14.

To understand the mechanism behind inverted hysteresis, the magnetic hysteresis at 125 K as an example is shown in fig.7.15. The schematic magnetic configuration, in accordance to three regions in the thin film is shown. The top panel shows the field

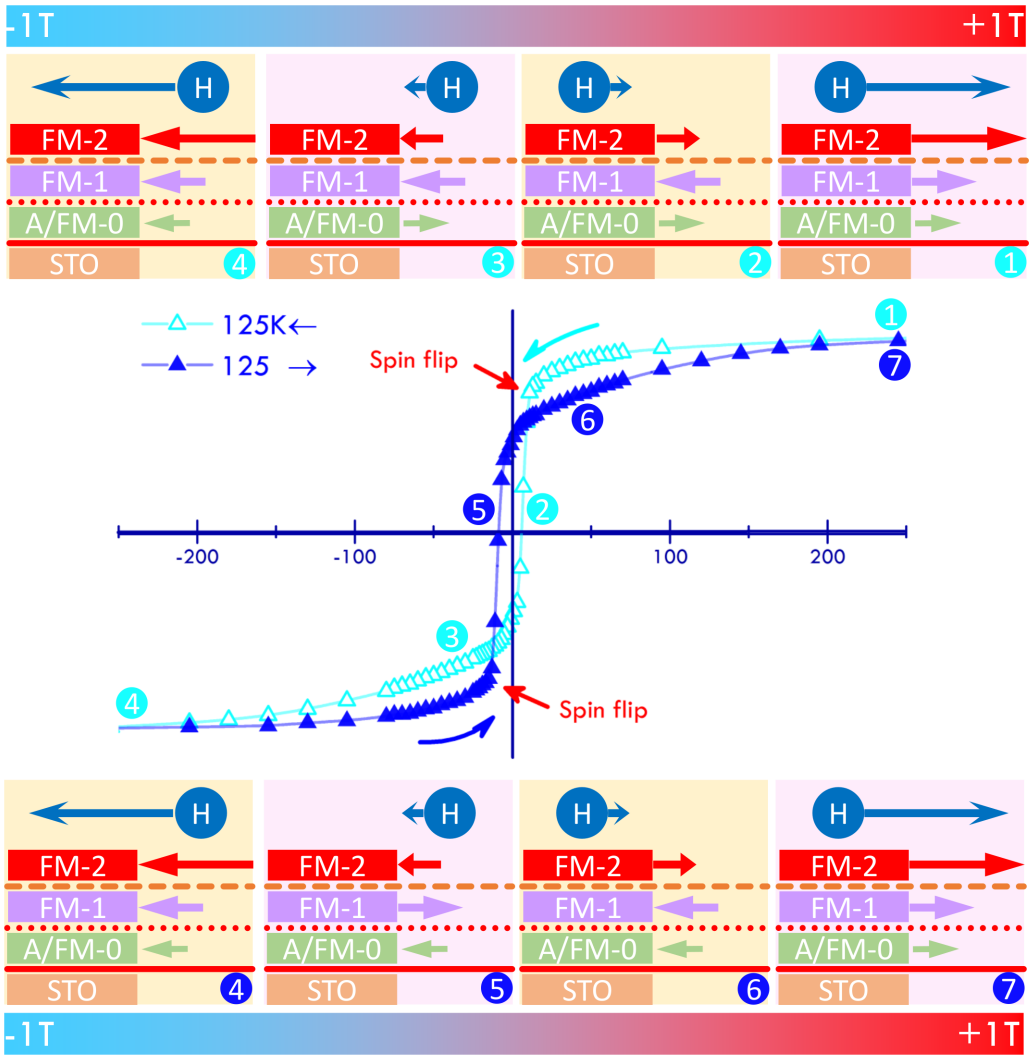

Figure 7.15: The inverted hysteresis at 125 K and the magnetic behavior of the three regions are shown. The top (bottom) schematic panel shows the magnetic configuration while sweeping the magnetic field from +1 (-1) T to -1 (+1) T.

sweeping from +1 T to -1 T and the bottom panel shows the field sweeping from -1 T to +1 T.

There are three main magnetic moments. A/FM-0 which is consist of one or two unit cells near the interface. FM-1 which is a ferromagnetic layer with Curie temperature of near 300 K. FM-2 is another ferromagnetic layer with Curie temperature of 250 K. It is seen that the magnetic interaction between A/FM-0 and the layer above (FM-1) is AFM. However, the 1 or 2 unit cell thickness of this layer makes it hard to determine exactly whether it is G-type or A-type. Although the M-T data (ZFC FW) show a tendency toward A-type. At +1T the magnetic field is strong enough to align all the moments in the field direction (step 1). In this configuration, since the temperature is fixed, the competition is between Zeeman and exchange interaction. As the magnetic field becomes smaller, the AFM exchange interaction becomes stronger (comparatively). At very small magnetic field (8 Oe), the AFM coupling between A/FM-0 and FM-1 overcomes the Zeeman interaction and a spin flip occurs, which is step 2. The FM coupling between FM-1 and FM-2 triggers the the reversal of FM-2 (step 3). As the magnetic field becomes strong again, all the magnetic layers align in the direction of magnetic field (step 4). Going from -1 T to +1 T, the same process happen. At smalle enough magnet field the AFM coupling between A/FM-0 overcomes Zeeman interaction and FM-1 reverses (step 5). This reversal triggers the reversal of FM-2 due to its FM coupling with FM-1 (step 6). Once again, at strong magnetic field all the magnetic layers align with magnetic field (step 7).

The ferromagnetic hysteresis of $La_{1-x}Sr_xMnO_{3-\delta}$ as function of temperature is shown in fig.7.16a. Prior to measurement of each hysteresis, the sample was cooled in the presence of 1000 Oe magnetic field from 380 K (well above Curie temperature) to the desired temperature. The hysteresis shows a horizontal shift which is indicative of exchange bias. Appearance of exchange bias and coercivity enehancement are two common features of

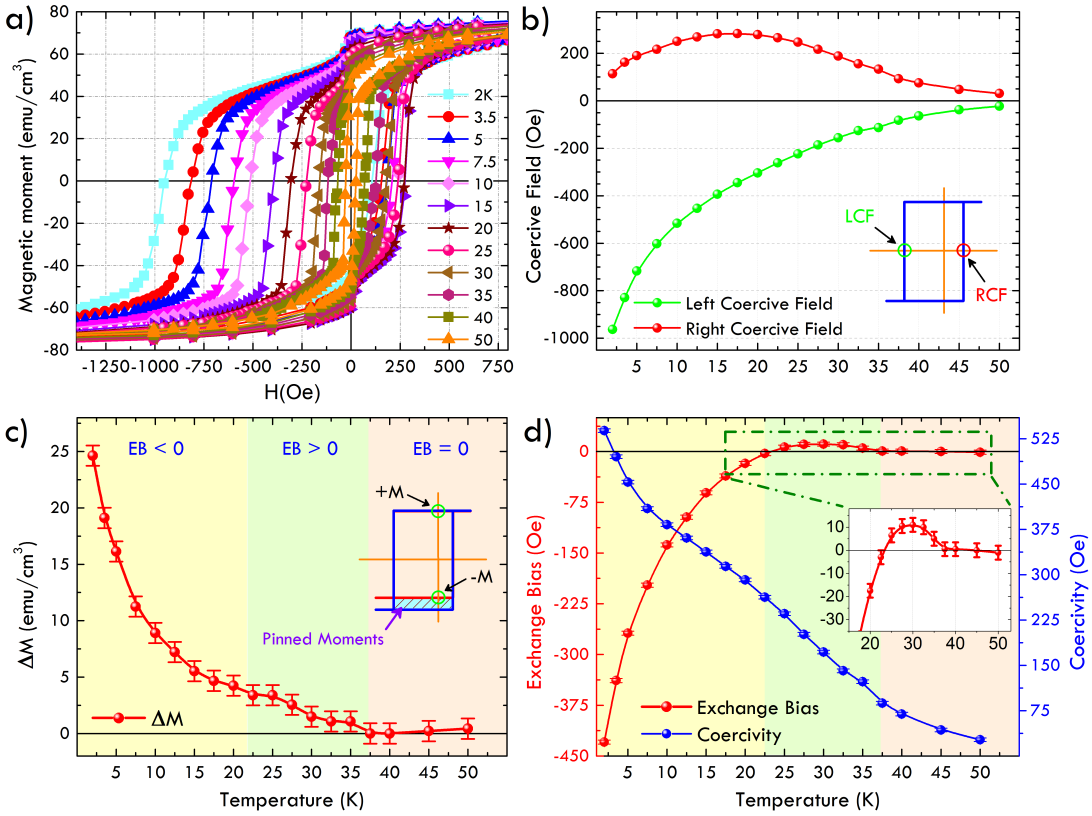

Figure 7.16: a) Magnetic moment vs external magnetic field, i.e. ferromagnetic hysteresis from 2 K to 50 K. b) Left and right coercive field as a function of temperature. Inset shows the position of left and right coercive field. c) The magnitude of pinned moment as a function of temperature. Pinned moments exponentially depend on temperature. The inset shows that the pinned moments are the difference between positive and negative remanent, i.e. a vertical shift of hysteresis. d) Exchange bias and coercivity as a function of temperature. Above 22.5 K the sign of exchange bias changes where it is shown in the inset.

magnetically coupled multi-layer systems [128]. Exchange bias H_{EB} and coercivity H_C are defined as,

$$H_{EB} = \frac{H_R + H_L}{2} \qquad H_C = \frac{H_R - H_L}{2} \tag{7.1}$$

where H_R and H_L are right and left coercive fields, respectively. Left and right coercive fields show a rather different change with temperature as it is shown in fig.7.16b. Left coercive field shows an exponential increase while right coercive field initially increase and then decrease, this behavior is called unidirectional coercivity enhancement [129]. Fig.7.16c shows the difference between positive and negative remenant moment. This difference is attributed to the presence of pinning magnetic moments where they do not change their direction upon changing the direction of magnetic field, hence they can provide a biasing field which leads to the appearance of exchange bias.

Exchange bias and coercivity as a function of temperature is shown in fig.7.16d. At 2 K, the exchange bias is negative 430 Oe and as the temperature increases the exchange bias decrease. At 22.5 K, exchange bias crosses zero and changes sign from negative to positive. Finally, at 37.5 K the exchange bias disappear, concomitantly with disappearance of pinned moments. The magnitude of exchange bias exponentially depends on temperature. The exponential dependence of pinning moments and exchange bias on temperature shows that thermal activation leads to unpinning of biasing moments, where in turn leads to exponential decay of exchange bias. On the other hand, coercivity shows a behavior closer to a linear temperature dependence. At 2 K, the coercivity is 528 Oe where it is larger than the ceorcivity of $La_{0.67}Sr_{0.33}MnO_3$ (11 Oe), almost by a factor of 50. At 50 K, the coercivity drops to 27 Oe. A closer look at the behavior of ceorcivity with temperature show two onsets of exponential decay, one from 2 K to 20 K and the other from 22.5 K to 50 K.

The exponential dependence of exchange bias on temperature sometimes is inter-

preted as a signature of glassy states in the material [130]. One of the experimental evidences for presence of spin glass in a system is the frequency dependence of blocking temperature in ac magnetic susceptibility [131]. Near spin glass transition temperature[1] due to the presence of numerous degenerate and nearly degenerate ground states, the ac magnetic susceptibility shows a peak (at blocking temperature) where its position depends on frequency. In a recent work [132], spin glass state was observed in $La_{0.67}Sr_{0.33}MnO_3$ grown on LSAT substrate in (001) direction. The presence of spin glass was attributed to $LaSrMnO_3$ near the interface (214 RP[2] phase). In the thin films presented here, no 214 phase was observed. Also, the TEM reported in that work showed obvious interface roughening near the interface. Although the stoichiometry and structure of the thin films showed variations from interface to surface, the RP phase was 113 throughout the thin film. To ensure that the observed magnetic properties are not due to a frustrated disorderd phase near the interface, we have performed ac magnetic susceptibility measurement shown in fig.7.17. The pronounced FM-2 transition is seen at 248 K. The FM transition of FM-1 is not observed due to the small signal coming from that region of the thin film. Below 37.5 K where the exchange bias appears no peak is observed. Also, the susceptibility signal under 10 and 1000 Hz does not show any difference where it shows that the system does not show any dynamic behavior. Absence of any feature at low temperature shows that the magnetic ground state is well-defined and it is not highly degenerate or frustrated.

7.8 Discussion

In the previous chapter it was shown that the broken symmetry at the interface of $La_{0.67}Sr_{0.33}MnO_3$ leads to appearance of interfacial magnetic interaction that affects the entire thin films. It was shown the first two unit cell of $La_{0.67}Sr_{0.33}MnO_3$ are responsible for this behavior. Changing the growth conditions, specially the oxygen pressure and

[1] In some literature called blocking temperature, not to be confused with blocking temperature in superparamagnetism.

[2] Ruddlesden-Popper.

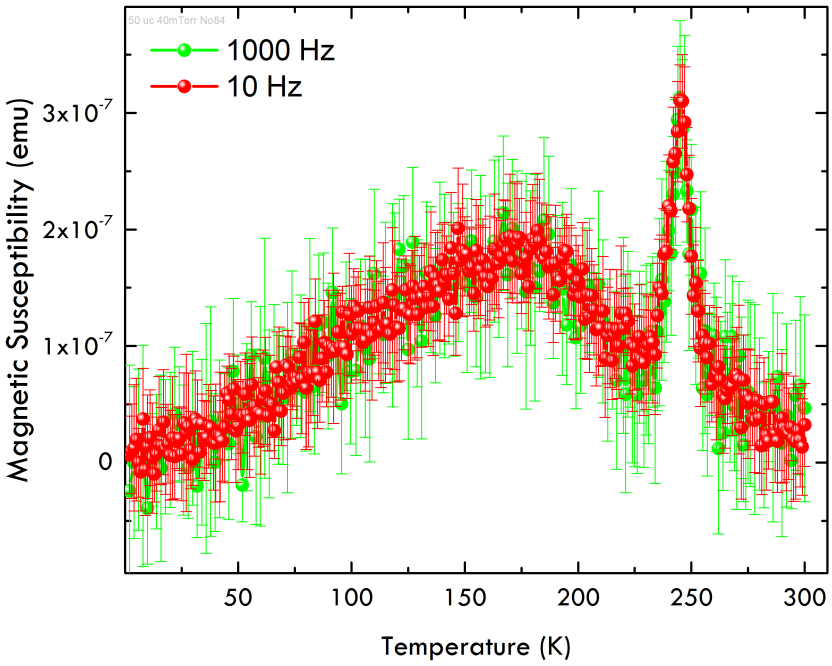

Figure 7.17: AC magnetic susceptibility as a function of temperature at 10 and 1000 Hz.

laser fluence, a new functional monolithic $La_{1-x}Sr_xMnO_{3-\delta}$ thin film was grown. The thin film shows three main structurally and stoichiometrically distinct regions. Each of these regions are magnetically active. The sensitive imbalance between superexchange and double exchange magnetic interaction have lead to a rich magnetic phase diagram where it shows exchange bias, spontaneous magnetic reversal and inverted hysteresis. The exchange bias was previously observed to appear in heavily oxygen deficient LSMO thin films [133]. Although no microscopic structural information was present in that work, the XRD data show that the c-axis of thin film is strongly elongated. No specific value was mentioned for elongated c-axis, however, author's estimation from the reported XRD data is 3.89 Å which is considerably larger than the thin films reported here (3.857 Å). Therefore, this distinguishes the present work from Ref. [133].

The presence of exchange bias, as shown in fig.7.16a, and the unidirectional coercivity enhancement (fig.7.16b) might make it seem reasonable to assume that the domain

wall pinning and presence of domains with different anisotropy is the reason for exchange bias. A similar behavior was seen before in Co/CoO heterostructures [129]. In Co/CoO system, presence of grain boundaries in the AFM layer (CoO) have converted uniaxial anisoptropy to unidirectional aniostropy where two (or more) AFM domains with dissimilar anisotropy were present. In the present work, TEM image shows that structure is coherent on atomic level and no grain boundary is observed. Therefore the presence of exchange bias is not simply due to the imperfections or mosaicity in the thin film. Actually, the change in the sign of exchange bias shows that fine magnetic interactions between three magnetic layers are responsible for it.

When the sample is cooled under external field, all th FM moments stay align with the field and antiferromagnetically coupled moments (near the interface) become antiparallel with the direction of magnetic field (also called setting field). When the temperature goes below blocking temperature, the AFM coupled moments lock in their direction. This is how negative exchange bias occurs. This is an ordered state in a sense that domain wall pinning is minimum, two preferred directions are well define, one direction by FM moments and anther by pinning moments. As the temperature increases, some of the pinning moments start to rotate due to the torque coming from FM moments. At this point, during M-H measurement, when the magnetic field is in the opposite direction of cooling field, the coercivity becomes smaller since some of biasing pinned moments are unpinned[1]. Now, in the second part of M-H measurement, when the magnetic field is sweeping back, the system wants to go from a less ordered state to an ordered state. The portion of FM moments which are under pinning effect, need less energy to rotate since Zeeman and exchange coupling are cooperative. But on the other hand, the portion of FM moments with unpinned AFM moments need more

[1]It should be noted in negative exchange bis, AFM moments pin FM moments. While above blocking temperature, FM moments start to pin AFM moments. The FM torque overcomes AFM anisotropy.

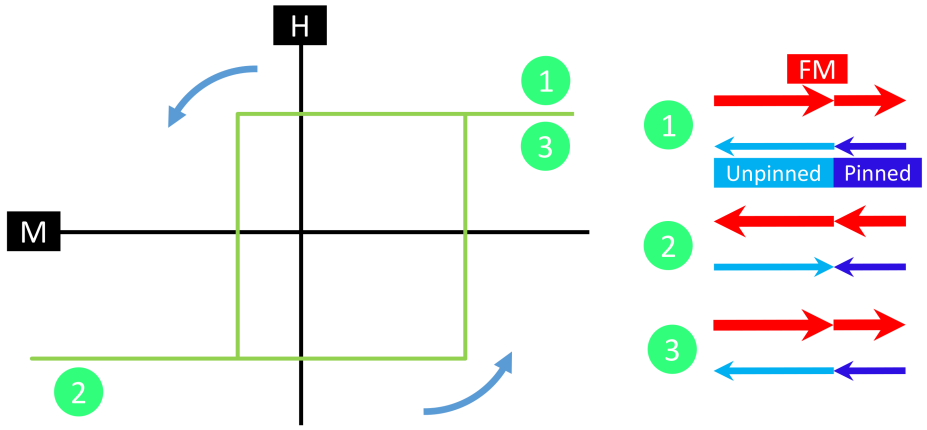

Figure 7.18: The M-H curve under positive exchange bias is shown. There are three magnetic moment types: FM, Unpinned AFM and Pinned AFM. Unpinned AFMs follow the FM moments. Going from step 1 to 2 requires less energy comparing to going from step 2 to 3. Going from 1 to 2, the interface (AFM moments) become disordered. Going from 2 to 3, the disordered AFM moments hinder the domain wall motion, therefore a larger coercivity is observed.

energy to rotate since they do not benefit from exchange coupling, In this case, Zeeman coupling is responsible for rotation of both FM and AFM coupled moments. Under this circumstances, the coercivity in the direction of cooling field enhances. This behavior is shown in fig.7.18. Once the temperature passes well above blocking temperature, then all the moments rotate, therefore left and right coercivity become equal and exchange bias disappear.

Above 40 K, all the AFM moments are unpinned and their direction is determined by considering the competition between Zeeman energy, thermal activation energy and exchange coupling. The interplay of these interaction was shown that leads to inverted hysteresis and spontaneous magnetic reversal.

7.9 Summary and outlook

Previous chapter showed that broken symmetry at the interface can lead to new interactions. In this chapter, it was shown that fine control of growth parameters can drastically change the physical properties of transition metal oxides. Magnetic properties of $La_{1-x}Sr_xMnO_{3-\delta}$ was shown to differ from the target material $La_{0.67}Sr_{0.33}MnO_3$.

Appearance of exchange bias, inverted hysteresis and spontaneous magnetic reversal once more show that intimate competition in electronic, spin and lattice degrees of freedom in transition metal oxides can lead to new functionality, even in a monolithic thin film.

The methodology put forward in this chapter can be used to study other multivalent transition metal oxides. The first step to further investigate this approach would be changing the substrate. This will change the symmetry breaking at the interface, magnetic anisotropy and last but not least, the growth condition. My preliminary work on growing $La_{0.67}Sr_{0.33}MnO_3$ on $LaAlO_3$ shows that changing substrate greatly changes the magnetic properties. This material shows exchange bias and the same RHEED behavior as $SrTiO_3$ was observed. Also, the easy axis of the sample was switched from in-plane to out-of-plane. This shows that this path, processing before, during and after growth can harness the rich physical properties of complicated transition metal oxides.

References

[1] Q Huang, A Santoro, JW Lynn, RW Erwin, JA Borchers, JL Peng, and RL Greene. Structure and magnetic order in undoped lanthanum manganite. *Physical Review B*, 55(22):14987, 1997. vii, 108, 110

[2] *Surface physics*. Oxford physics series. Clarendon Press, 1983. viii, 4

[3] Gerd Binnig, Heinrich Rohrer, Ch Gerber, and E Weibel. Surface studies by scanning tunneling microscopy. *Physical review letters*, 49(1):57, 1982. viii, 7, 8

[4] Stefan Hűfner. *Photoelectron Spectroscopy: principles and applications*. Springer, 2003. xi, 30, 31, 33

[5] A Goldmann, J Tejeda, NJ Shevchik, and M Cardona. Density of valence states of CuCl, CuBr, CuI and AgI. *Physical Review B*, 10(10):4388, 1974. xi, 34

[6] D. M. Riffe, G. K. Wertheim, and P. H. Citrin. Alkali metal adsorbates on w(110): Ionic, covalent, or metallic? *Phys. Rev. Lett.*, 64:571–574, Jan 1990. xi, 49

[7] R. I. Eglitis and David Vanderbilt. First-principles calculations of atomic and electronic structure of srtio$_3$ (001) and (011) surfaces. *Phys. Rev. B*, 77:195408, May 2008. xii, 56, 57

[8] Julia A Mundy, Yasuyuki Hikita, Takeaki Hidaka, Takeaki Yajima, Takuya Higuchi, Harold Y Hwang, David A Muller, and Lena F Kourkoutis. Visualizing the interfacial evolution from charge compensation to metallic screening across the manganite metal–insulator transition. *Nature communications*, 5, 2014. xiv, 73

[9] Yulan Li, Ke Xu, Shenyang Hu, Jon Suter, Daniel K Schreiber, Pradeep Ramuhalli, Bradley R Johnson, and John McCloy. Computational and experimental investigations of magnetic domain structures in patterned magnetic thin films. *Journal of Physics D: Applied Physics*, 48(30):305001, 2015. xv, 86

[10] S. S. P. Parkin and D. Mauri. Spin engineering: Direct determination of the ruderman-kittel-kasuya-yosida far-field range function in ruthenium. *Phys. Rev. B*, 44:7131–7134, Oct 1991. xvii, 102

[11] J. Hemberger, A. Krimmel, T. Kurz, H.-A. Krug von Nidda, V. Yu. Ivanov, A. A. Mukhin, A. M. Balbashov, and A. Loidl. Structural, magnetic, and electrical properties of single-crystalline $La_{1-x}Sr_xMnO_3$ ($0.4 < x < 0.85$). *Phys. Rev. B*, 66:094410, 2002. xvii, 108

[12] Xiaoyan Li, Ionela Lindfors-Vrejoiu, Michael Ziese, Alexandre Gloter, and Peter A van Aken. Impact of interfacial coupling of oxygen octahedra on ferromagnetic order in $La_{0.67}Sr_{0.33}MnO_3/SrTiO_3$ heterostructures. *Scientific Reports*, 7:40068, 2017. xix, 127, 129

[13] CJ Howard and HT Stokes. Group-theoretical analysis of octahedral tilting in perovskites. *Acta Crystallographica Section B: Structural Science*, 54(6):782–789, 1998. xxii, 178, 179

[14] AD Caviglia, Stefano Gariglio, Nicolas Reyren, Didier Jaccard, T Schneider, M Gabay, S Thiel, G Hammerl, Jochen Mannhart, and J-M Triscone. Electric field control of the $LaAlO_3/SrTiO_3$ interface ground state. *Nature*, 456(7222):624–627, 2008. 1

[15] Mark Huijben, Alexander Brinkman, Gertjan Koster, Guus Rijnders, Hans Hilgenkamp, and Dave HA Blank. Structure–property relation of $LaAlO_3/SrTiO_3$ interfaces. *Advanced Materials*, 21(17):1665–1677, 2009. 1

[16] Rossitza Pentcheva and Warren E Pickett. Charge localization or itineracy at $LaAlO_3/SrTiO_3$ interfaces: Hole polarons, oxygen vacancies, and mobile electrons. *Physical Review B*, 74(3):035112, 2006. 1

[17] John H Moore, Christopher C Davis, Michael A Coplan, and Sandra C Greer. Building scientific apparatus. *Building Scientific Apparatus, by John H. Moore, Christopher C. Davis, Michael A. Coplan, Sandra C. Greer, Cambridge, UK: Cambridge University Press, 2009*, 1, 2009. 27

[18] Friedrich Reinert and Stefan Hüfner. Photoemission spectroscopyfrom early days to recent applications. *New Journal of Physics*, 7(1):97, 2005. 29

[19] PW Tasker. The stability of ionic crystal surfaces. *Journal of Physics C: Solid State Physics*, 12(22):4977, 1979. 51, 59

[20] N Bickel, G Schmidt, K Heinz, and K Müller. Ferroelectric relaxation of the $SrTiO_3$ (100) surface. *Physical review letters*, 62(17):2009, 1989. 56

[21] PV Nagarkar, PC Searson, and FD Gealy III. Effect of surface treatment on $SrTiO_3$: An x-ray photoelectron spectroscopic study. *Journal of applied physics*, 69(1):459–462, 1991. 58

[22] PAW Van der Heide, QD Jiang, YS Kim, and JW Rabalais. X-ray photoelectron spectroscopic and ion scattering study of the $SrTiO_3$ (001) surface. *Surface science*, 473(1):59–70, 2001. 58

[23] MP Seah and WA Dench. Quantitative electron spectroscopy of surfaces: a standard data base for electron inelastic mean free paths in solids. *Surface and interface analysis*, 1(1):2–11, 1979. 59, 76

[24] EB Saloman, JH Hubbell, and JH Scofield. X-ray attenuation cross sections for energies 100 ev to 100 kev and elements z= 1 to z= 92. *Atomic Data and Nuclear Data Tables*, 38(1):1–196, 1988. 59, 64

[25] PW Tasker. The surface energies, surface tensions and surface structure of the alkali halide crystals. *Philosophical Magazine A*, 39(2):119–136, 1979. 59

[26] Jacek Goniakowski, Fabio Finocchi, and Claudine Noguera. Polarity of oxide surfaces and nanostructures. *Reports on Progress in Physics*, 71(1):016501, 2007. 60

[27] Claudine Noguera. Polar oxide surfaces. *Journal of Physics: Condensed Matter*, 12(31):R367, 2000. 60, 70

[28] Ann N Chiaramonti, Courtney H Lanier, Laurence D Marks, and Peter C Stair. Time, temperature, and oxygen partial pressure-dependent surface reconstructions on $SrTiO_3$ (111): a systematic study of oxygen-rich conditions. *Surface Science*, 602(18):3018–3025, 2008. 60, 63

[29] Hiroyuki Tanaka and Tomoji Kawai. Surface structure of reduced $SrTiO_3$ (111) observed by scanning tunneling microscopy. *Surface science*, 365(2):437–442, 1996. 60

[30] Bruce C Russell and Martin R Castell. Surface of sputtered and annealed polar $SrTiO_3$ (111): Tio x-rich (n× n) reconstructions. *The Journal of Physical Chemistry C*, 112(16):6538–6545, 2008. 60, 63

[31] Bruce C Russell and Martin R Castell. (13× 13) r 13.9 and (7× 7) r 19.1 reconstructions of the polar $SrTiO_3$ (111) surface. *Physical Review B*, 75(15):155433, 2007. 60, 63

[32] JG Connell, BJ Isaac, GB Ekanayake, DR Strachan, and SSA Seo. Preparation of atomically flat $SrTiO_3$ surfaces using a deionized-water leaching and thermal annealing procedure. *Applied Physics Letters*, 101(25):251607, 2012. 61

[33] Jaewan Chang, Yoon-Seok Park, and Sang-Koog Kim. Atomically flat single-terminated $SrTiO_3$ (111) surface. *Applied Physics Letters*, 92(15):152910–152910, 2008. 61

[34] A Biswas, PB Rossen, C-H Yang, W Siemons, M-H Jung, IK Yang, R Ramesh, and YH Jeong. Universal ti-rich termination of atomically flat $SrTiO_3$ (001),(110), and (111) surfaces. *Applied Physics Letters*, 98(5):051904–051904, 2011. 61

[35] JL Blok, X Wan, G Koster, DHA Blank, and G Rijnders. Epitaxial oxide growth on polar (111) surfaces. *Applied Physics Letters*, 99(15):151917, 2011. 61, 70

[36] S Middey, P Rivero, D Meyers, M Kareev, X Liu, Y Cao, JW Freeland, S Barraza-Lopez, and J Chakhalian. Polarity compensation in ultra-thin films of complex oxides: The case of a perovskite nickelate. *Scientific reports*, 4, 2014. 61, 70, 75, 81

[37] Jaewan Chang, Yoon-Seok Park, Jong-Woo Lee, and Sang-Koog Kim. Layer-by-layer growth and growth-mode transition of srruo 3 thin films on atomically flat single-terminated $SrTiO_3$ (111) surfaces. *Journal of crystal growth*, 311(14):3771–3774, 2009. 61

[38] Jiagui Feng, Xuetao Zhu, and Jiandong Guo. Reconstructions on $SrTiO_3$ (111) surface tuned by ti/sr deposition. *Surface Science*, 614:38–45, 2013. 63

[39] LD Marks, AN Chiaramonti, SU Rahman, and MR Castell. Transition from order to configurational disorder for surface reconstructions on $SrTiO_3$ (111). *Physical review letters*, 114(22):226101, 2015. 63

[40] Shigeo Tanuma, Cedric J Powell, and David R Penn. Calculations of electron inelastic mean free paths. v. data for 14 organic compounds over the 50–2000 ev range. *Surface and Interface Analysis*, 21(3):165–176, 1994. 64

[41] GM Vanacore, LF Zagonel, and N Barrett. Surface enhanced covalency and madelung potentials in nb-doped $SrTiO_3$ (100),(110) and (111) single crystals. *Surface Science*, 604(19):1674–1683, 2010. 65

[42] A Shchukarev and D Korolkov. Xps study of group ia carbonates. *Open Chemistry*, 2(2):347–362, 2004. 65

[43] Erik Lewin, PO Å Persson, Martina Lattemann, M Stüber, M Gorgoi, A Sandell, C Ziebert, F Schäfers, W Braun, J Halbritter, et al. On the origin of a third spectral component of c1s xps-spectra for nc-TiC/aC nanocomposite thin films. *Surface and Coatings Technology*, 202(15):3563–3570, 2008. 65

[44] MK Rajumon, MS Hegde, and CNR Rao. Adsorption of carbon monoxide on Ni/Ti and Ni/Tio2 surfaces preparedin situ in the electron spectrometer: A combined ups-xps study. *Catalysis letters*, 1(11):351–359, 1988. 65

[45] NC Plumb, M Salluzzo, E Razzoli, M Månsson, M Falub, J Krempasky, CE Matt, J Chang, M Schulte, J Braun, et al. Mixed dimensionality of confined conducting electrons in the surface region of $SrTiO_3$. *Physical review letters*, 113(8):086801, 2014. 67

[46] TC Rödel, C Bareille, F Fortuna, C Baumier, F Bertran, P Le Fèvre, M Gabay, O Hijano Cubelos, MJ Rozenberg, T Maroutian, et al. Orientational tuning of the fermi sea of confined electrons at the $SrTiO_3$ (110) and (111) surfaces. *Physical Review Applied*, 1(5):051002, 2014. 67

[47] S McKeown Walker, Alberto De La Torre, Flavio Yair Bruno, Anna Tamai, TK Kim, M Hoesch, M Shi, MS Bahramy, PDC King, and Félix Baumberger. Control of a two-dimensional electron gas on $SrTiO_3$ (111) by atomic oxygen. *Physical review letters*, 113(17):177601, 2014. 67

[48] Ariana Pojani, Fabio Finocchi, and Claudine Noguera. Polarity on the $SrTiO_3$ (111) and (110) surfaces. *Surface science*, 442(2):179–198, 1999. 67

[49] A Pojani, F Finocchi, and C Noguera. A theoretical study of the unreconstructed polar (111) face of sto. *Applied surface science*, 142(1):177–181, 1999. 67

[50] Pavlo Zubko, Stefano Gariglio, Marc Gabay, Philippe Ghosez, and Jean-Marc Triscone. Interface physics in complex oxide heterostructures. *Annu. Rev. Condens. Matter Phys.*, 2(1):141–165, 2011. 68

[51] Julie A Bert, Beena Kalisky, Christopher Bell, Minu Kim, Yasuyuki Hikita, Harold Y Hwang, and Kathryn A Moler. Direct imaging of the coexistence of ferromagnetism and superconductivity at the $LaAlO_3/SrTiO_3$ interface. *Nature physics*, 7(10):767–771, 2011. 68

[52] A Ohtomo and HY Hwang. A high-mobility electron gas at the laalo3/srtio3 heterointerface. *Nature*, 427(6973):423–426, 2004. 68

[53] Nicolas Reyren, S Thiel, AD Caviglia, L Fitting Kourkoutis, G Hammerl, C Richter, CW Schneider, T Kopp, A-S Rüetschi, Didier Jaccard, et al. Superconducting interfaces between insulating oxides. *Science*, 317(5842):1196–1199, 2007. 68

[54] Harold Y Hwang, Yoh Iwasa, Masashi Kawasaki, Bernhard Keimer, Naoto Nagaosa, and Yoshinori Tokura. Emergent phenomena at oxide interfaces. *Nature materials*, 11(2):103–113, 2012. 68

[55] Jak Chakhalian, JM Rondinelli, Jian Liu, BA Gray, M Kareev, EJ Moon, N Prasai, JL Cohn, M Varela, IC Tung, et al. Asymmetric orbital-lattice interactions in ultrathin correlated oxide films. *Physical review letters*, 107(11):116805, 2011. 68

[56] JH Ngai, FJ Walker, and CH Ahn. Correlated oxide physics and electronics. *Annual Review of Materials Research*, 44:1–17, 2014. 68

[57] M Gibert, M Viret, P Zubko, N Jaouen, J-M Tonnerre, A Torres-Pardo, S Catalano, A Gloter, O Stéphan, and J-M Triscone. Interlayer coupling through a dimensionality-induced magnetic state. *Nature communications*, 7, 2016. 68

[58] Marta Gibert, Pavlo Zubko, Raoul Scherwitzl, Jorge Íñiguez, and Jean-Marc Triscone. Exchange bias in $LaNiO_3/LaMnO_3$ superlattices. *Nature materials*, 11(3):195–198, 2012. 68

[59] Marta Gibert, Michel Viret, Almudena Torres-Pardo, Cinthia Piamonteze, Pavlo Zubko, Nicolas Jaouen, J-M Tonnerre, Alexandra Mougin, Jennifer Fowlie, Sara Catalano, et al. Interfacial control of magnetic properties at $LaNiO_3/LaMnO_3$ interfaces. *Nano letters*, 15(11):7355–7361, 2015. 68

[60] David Doennig, Warren E Pickett, and Rossitza Pentcheva. Confinement-driven transitions between topological and mott phases in $(LaNiO_3)_n/(LaAlO_3)_m$ (111) superlattices. *Physical Review B*, 89(12):121110, 2014. 68

[61] Haoming Wei, Marius Grundmann, and Michael Lorenz. Confinement-driven metal-insulator transition and polarity-controlled conductivity of epitaxial lanio3/laalo3 (111) superlattices. *Applied Physics Letters*, 109(8):082108, 2016. 68

[62] David Doennig, Warren E Pickett, and Rossitza Pentcheva. Massive symmetry breaking in $LaAlO_3/SrTiO_3$ (111) quantum wells: A three-orbital strongly correlated generalization of graphene. *Physical review letters*, 111(12):126804, 2013. 68

[63] Jak Chakhalian, AJ Millis, and J Rondinelli. Whither the oxide interface. *Nature materials*, 11(2):92–94, 2012. 68

[64] Di Xiao, Wenguang Zhu, Ying Ran, Naoto Nagaosa, and Satoshi Okamoto. Interface engineering of quantum hall effects in digital transition metal oxide heterostructures. *Nature communications*, 2:596, 2011. 68

[65] G Catalan. Progress in perovskite nickelate research. *Phase Transitions*, 81(7-8):729–749, 2008. 69

[66] I Hallsteinsen, JE Boschker, M Nord, S Lee, M Rzchowski, PE Vullum, JK Grepstad, R Holmestad, CB Eom, and T Tybell. Surface stability of epitaxial $La_{0.67}Sr_{0.33}MnO_3$ thin films on (111)-oriented $SrTiO_3$. *Journal of Applied Physics*, 113(18):183512, 2013. 70

[67] Naoyuki Nakagawa, Harold Y Hwang, and David A Muller. Why some interfaces cannot be sharp. *Nature materials*, 5(3):204–209, 2006. 70

[68] Annunziata Savoia, D Paparo, P Perna, Z Ristic, M Salluzzo, F Miletto Granozio, U Scotti di Uccio, C Richter, S Thiel, J Mannhart, et al. Polar catastrophe and electronic reconstructions at the $LaAlO_3/SrTiO_3$ interface: Evidence from optical second harmonic generation. *Physical Review B*, 80(7):075110, 2009. 70

[69] S Middey, J Chakhalian, P Mahadevan, JW Freeland, AJ Millis, and DD Sarma. Physics of ultrathin films and heterostructures of rare-earth nickelates. *Annual Review of Materials Research*, (0), 2016. 70

[70] M Sankararaman and D Perry. Valence determination of titanium and iron using electron energy loss spectroscopy. *Journal of materials science*, 27(10):2731–2733, 1992. 71

[71] A Ohtomo, DA Muller, JL Grazul, and HY Hwang. Epitaxial growth and electronic structure of latio x films. *Applied physics letters*, 80(21):3922–3924, 2002. 71

[72] Q Qiao, Robert F Klie, S Öğüt, and JC Idrobo. Atomic and electronic structures of $SrTiO_3$/gaas heterointerfaces: An 80-kv atomic-resolution electron energy-loss spectroscopy study. *Physical Review B*, 85(16):165406, 2012. 71

[73] M Abbate, FMF De Groot, JC Fuggle, A Fujimori, Y Tokura, Y Fujishima, O Strebel, M Domke, G Kaindl, J Van Elp, et al. Soft-x-ray-absorption studies of the location of extra charges induced by substitution in controlled-valence materials. *Physical Review B*, 44(11):5419, 1991. 71

[74] Liang Qiao and Xiaofang Bi. Direct observation of ni3+ and ni2+ in correlated $LaNiO_{3-\delta}$ films. *EPL (Europhysics Letters)*, 93(5):57002, 2011. 76

[75] Paul S Bagus, Eugene S Ilton, and Connie J Nelin. The interpretation of xps spectra: Insights into materials properties. *Surface Science Reports*, 68(2):273–304, 2013. 81

[76] P.R. Wallace and O.P. Gupta. Low temperature magnetic susceptibility of pure graphite in strong magnetic fields. *Solid State Communications*, 15(10):1577 – 1580, 1974. 84

[77] H.A Kramers. L'interaction entre les atomes magntognes dans un cristal paramagntique. *Physica*, 1(1):182 – 192, 1934. 98

[78] P. W. Anderson. Antiferromagnetism. theory of superexchange interaction. *Phys. Rev.*, 79:350–356, Jul 1950. 98

[79] M. A. Ruderman and C. Kittel. Indirect exchange coupling of nuclear magnetic moments by conduction electrons. *Phys. Rev.*, 96:99–102, Oct 1954. 102

[80] Kei Yosida. Magnetic properties of cu-mn alloys. *Phys. Rev.*, 106:893–898, Jun 1957. 102

[81] Tadao Kasuya. A theory of metallic ferro-and antiferromagnetism on zener's model. *Progress of theoretical physics*, 16(1):45–57, 1956. 102

[82] J. Friedel. Metallic alloys. *Il Nuovo Cimento (1955-1965)*, 7(2):287–311, 1958. 103

[83] I. Dzyaloshinsky. A thermodynamic theory of weak ferromagnetism of antiferromagnetics. *Journal of Physics and Chemistry of Solids*, 4(4):241 – 255, 1958. 103

[84] J-S Zhou and JB Goodenough. Paramagnetic phase in single-crystal $LaMnO_3$. *Physical Review B*, 60(22):R15002, 1999. 110

[85] J Töpfer and JB Goodenough. Lamno 3+ δ revisited. *Journal of Solid State Chemistry*, 130(1):117–128, 1997. 110

[86] Koji Kuroda, Nobuo Ishizawa, Nobuyasu Mizutani, and Masanori Kato. The crystal structure of α- $SrMnO_3$. *Journal of Solid State Chemistry*, 38(3):297–299, 1981. 110

[87] PD Battle, TC Gibb, and CW Jones. The structural and magnetic properties of $srmno_3$: a reinvestigation. *Journal of Solid State Chemistry*, 74(1):60–66, 1988. 110

[88] BL Chamberland, AW Sleight, and JF Weiher. Preparation and characterization of bamno3 and srmno3 polytypes. *Journal of Solid State Chemistry*, 1(3-4):506–511, 1970. 110

[89] Rune Søndenå, P Ravindran, Svein Stølen, Tor Grande, and Michael Hanfland. Electronic structure and magnetic properties of cubic and hexagonal $SrMnO_3$. *Physical Review B*, 74(14):144102, 2006. 110

[90] Takayoshi Takeda and Soji Ohara. Magnetic structure of the cubic perovskite type $SrMnO_3$. *Journal of the Physical Society of Japan*, 37:275, 1974. 111

[91] K Kikuchi, H Chiba, M Kikuchi, and Y Syono. Syntheses and magnetic properties of $la_{1-x}sr_xmno_y$ (0.5 x 1.0) perovskite. *Journal of Solid State Chemistry*, 146(1):1–5, 1999. 111

[92] O Chmaissem, B Dabrowski, S Kolesnik, J Mais, DE Brown, R Kruk, P Prior, B Pyles, and JD Jorgensen. Relationship between structural parameters and the néel temperature in $Sr_{1-x}Ca_xMnO_3$ (0¡˜ x¡˜ 1) and sr 1- y ba y mno 3 (y¡˜ 0. 2). *Physical Review B*, 64(13):134412, 2001. 111

[93] T. Saitoh, A. E. Bocquet, T. Mizokawa, H. Namatame, A. Fujimori, M. Abbate, Y. Takeda, and M. Takano. Electronic structure of $la_{1-x}sr_xmno_3$ studied by photoemission and x-ray-absorption spectroscopy. *Phys. Rev. B*, 51:13942–13951, May 1995. 111

[94] G Zampieri, F Prado, A Caneiro, J Briatico, MT Causa, M Tovar, B Alascio, M Abbate, and E Morikawa. Electronic structure of camno x with 2.66¡˜ x¡˜ 3.00 studied with photoemission and x-ray-absorption spectroscopy. *Physical Review B*, 58(7):3755, 1998. 111

[95] M. Abbate, F. M. F. de Groot, J. C. Fuggle, A. Fujimori, O. Strebel, F. Lopez, M. Domke, G. Kaindl, G. A. Sawatzky, M. Takano, Y. Takeda, H. Eisaki, and S. Uchida. Controlled-valence properties of $la_{1-x}sr_xfeo_3$ and $la_{1-x}sr_xmno_3$ studied by soft-x-ray absorption spectroscopy. *Phys. Rev. B*, 46:4511–4519, Aug 1992. 111

[96] WC Mackrodt and E-A Williamson. First principles description of the valence states in manganese oxides. *Berichte der Bunsengesellschaft für physikalische Chemie*, 101(9):1215–1221, 1997. 111

[97] R_ von Helmolt, J Wecker, B Holzapfel, L Schultz, and K Samwer. Giant negative magnetoresistance in perovskitelike $La_{2/3}Ba_{1/3}Mn_{O-x}$ ferromagnetic films. *Physical Review Letters*, 71(14):2331, 1993. 111

[98] S Jin, Th H Tiefel, M McCormack, RA Fastnacht, R Ramesh, LH Chen, et al. Thousandfold change in resistivity in magnetoresistive la-ca-mn-o films. *Science-AAAS-Weekly Paper Edition-including Guide to Scientific Information*, 264(5157):413–414, 1994. 111

[99] JZ Sun, WJ Gallagher, PR Duncombe, L Krusin-Elbaum, RA Altman, A Gupta, Yu Lu, GQ Gong, and Gang Xiao. Observation of large low-field magnetoresistance in trilayer perpendicular transport devices made using doped manganate perovskites. *Applied Physics Letters*, 69(21):3266–3268, 1996. 111

[100] J O'Donnell, AE Andrus, S Oh, EV Colla, and JN Eckstein. Colossal magnetoresistance magnetic tunnel junctions grown by molecular-beam epitaxy. *Applied Physics Letters*, 76, 2000. 111

[101] M Bowen, M Bibes, A Barthélémy, J-P Contour, A Anane, Y Lemaıtre, and A Fert. Nearly total spin polarization in $La_{0.67}Sr_{0.33}MnO_3$ from tunneling experiments. *Applied Physics Letters*, 82(2):233–235, 2003. 111

[102] Yasushi Ogimoto, Makoto Izumi, Akihito Sawa, Takashi Manako, Hiroshi Sato, Hiroshi Akoh, Masashi Kawasaki, and Yoshinori Tokura. Tunneling magnetoresistance above room temperature in $La_{0.67}Sr_{0.33}MnO_3$/ $SrTiO_3$/ $La_{0.67}Sr_{0.33}MnO_3$ junctions. *Japanese journal of applied physics*, 42(4A):L369, 2003. 111

[103] FM Postma, R Ramaneti, T Banerjee, H Gokcan, E Haq, DHA Blank, R Jansen, and JC Lodder. Epitaxial diodes of a half-metallic ferromagnet on an oxide semiconductor. *interface*, 4:6, 2004. 111

[104] N Nakagawa, M Asai, Y Mukunoki, T Susaki, and HY Hwang. Magnetocapacitance and exponential magnetoresistance in manganite–titanate heterojunctions. *Applied Physics Letters*, 86(8):082504, 2005. 111

[105] Yasuyuki Hikita, Mitsuru Nishikawa, Takeaki Yajima, and Harold Y Hwang. Termination control of the interface dipole in $La_{0.67}Sr_{0.33}MnO_3$/nb: $SrTiO_3$ (001) schottky junctions. *Physical Review B*, 79(7):073101, 2009. 111

[106] W Eerenstein, M Wiora, JL Prieto, JF Scott, and ND Mathur. Giant sharp and persistent converse magnetoelectric effects in multiferroic epitaxial heterostructures. *Nature materials*, 6(5):348–351, 2007. 111

[107] Hajo JA Molegraaf, Jason Hoffman, Carlos AF Vaz, Stefano Gariglio, Dirk Van Der Marel, Charles H Ahn, and Jean-Marc Triscone. Magnetoelectric effects in complex oxides with competing ground states. *Advanced Materials*, 21(34):3470–3474, 2009. 111

[108] ZY Chen, Amlan Biswas, Igor Žutić, T Wu, SB Ogale, RL Greene, and T Venkatesan. Spin-polarized transport across a $La_{0.7}Sr_{0.3}MnO_3/YBa_2Cu_3O_{7-x}$ interface: role of andreev bound states. *Physical Review B*, 63(21):212508, 2001. 111

[109] Albina Y Borisevich, Hye Jung Chang, Mark Huijben, Mark P Oxley, Satoshi Okamoto, Manish K Niranjan, JD Burton, EY Tsymbal, Ying-Hao Chu, P Yu, et al. Suppression of octahedral tilts and associated changes in electronic properties at epitaxial oxide heterostructure interfaces. *Physical review letters*, 105(8):087204, 2010. 111

[110] H Boschker, M Huijben, A Vailionis, J Verbeeck, S v van Aert, M Luysberg, S Bals, G v van Tendeloo, EP Houwman, G Koster, et al. Optimized fabrication of high-quality $La_{0.67}Sr_{0.33}MnO_3$ thin films considering all essential characteristics. *Journal of Physics D: Applied Physics*, 44(20):205001, 2011. 112, 116, 120, 123, 135

[111] Zhaoliang Liao, Fengmiao Li, Peng Gao, Lin Li, Jiandong Guo, Xiaoqing Pan, R Jin, EW Plummer, and Jiandi Zhang. Origin of the metal-insulator transition in ultrathin films of $La_{0.67}Sr_{0.33}MnO_3$. *Physical Review B*, 92(12):125123, 2015. 112, 113, 120

[112] PG Radaelli, G Iannone, M Marezio, HY Hwang, SW Cheong, JD Jorgensen, and DN Argyriou. Structural effects on the magnetic and transport properties of perovskite $A_{1-x}A'_xMnO_3$ (x= 0.25, 0.30). *Physical Review B*, 56(13):8265, 1997. 113

[113] AM Glazer. The classification of tilted octahedra in perovskites. *Acta Crystallographica Section B: Structural Crystallography and Crystal Chemistry*, 28(11):3384–3392, 1972. 113, 119, 178

[114] Haizhong Guo, Jia-ou Wang, Xu He, Zhenzhong Yang, Qinghua Zhang, Kuijuan Jin, Chen Ge, Ruiqiang Zhao, Lin Gu, Yaqing Feng, et al. The origin of oxygen vacancies controlling $La_{0.67}Sr_{0.33}MnO_3$ electronic and magnetic properties. *Advanced Materials Interfaces*, 2016. 123

[115] F Tsui, MC Smoak, TK Nath, and CB Eom. Strain-dependent magnetic phase diagram of epitaxial $La_{0.67}Sr_{0.33}MnO_3$ thin films. *Applied Physics Letters*, 76(17):2421–2423, 2000. 123

[116] J-S Lee, DA Arena, P Yu, CS Nelson, R Fan, CJ Kinane, S Langridge, MD Rossell, R Ramesh, and C-C Kao. Hidden magnetic configuration in epitaxial $La_{1-x}Sr_xMnO_3$ films. *Physical review letters*, 105(25):257204, 2010. 126, 152

[117] J-S Lee, DA Arena, TS Santos, CS Nelson, SI Hyun, JH Shim, and C-C Kao. Controlling competing interactions at oxide interfaces: Enhanced anisotropy in $La_{0.67}Sr_{0.33}MnO_3$ films via interface engineering. *Physical Review B*, 85(23):235125, 2012. 126

[118] Hans Boschker, Jaap Kautz, Evert P Houwman, Wolter Siemons, Dave HA Blank, Mark Huijben, Gertjan Koster, Arturas Vailionis, and Guus Rijnders. High-temperature magnetic insulating phase in ultrathin $La_{0.67}Sr_{0.33}MnO_3$ films. *Physical review letters*, 109(15):157207, 2012. 127

[119] A Vailionis, H Boschker, Z Liao, JRA Smit, G Rijnders, M Huijben, and G Koster. Symmetry and lattice mismatch induced strain accommodation near and away from correlated perovskite interfaces. *Applied physics letters*, 105(13):131906, 2014. 129

[120] HY Hwang, SW Cheong, PG Radaelli, M Marezio, and B Batlogg. Lattice effects on the magnetoresistance in doped lamn o 3. *Physical Review Letters*, 75(5):914, 1995. 132

[121] A Bhattacharya, X Zhai, M Warusawithana, JN Eckstein, and SD Bader. Signatures of enhanced ordering temperatures in digital superlattices of (la mn o 3) m/(sr mn o 3) 2 m. *Applied physics letters*, 90(22):222503, 2007. 141

[122] M Varela, MP Oxley, W Luo, J Tao, Masashi Watanabe, Andrew R Lupini, ST Pantelides, and SJ Pennycook. Atomic-resolution imaging of oxidation states in manganites. *Physical Review B*, 79(8):085117, 2009. 145

[123] Chen Ge, Kui-Juan Jin, Lin Gu, Li-Cong Peng, Yong-Sheng Hu, Hai-Zhong Guo, Hong-Fei Shi, Jian-Kun Li, Jia-Ou Wang, Xiang-Xin Guo, et al. Metal–insulator transition induced by oxygen vacancies from electrochemical reaction in ionic liquid-gated manganite films. *Advanced Materials Interfaces*, 2(17), 2015. 147

[124] W Zhong and David Vanderbilt. Effect of quantum fluctuations on structural phase transitions in $SrTiO_3$ and $BaTiO_3$. *Physical Review B*, 53(9):5047, 1996. 152

[125] C Aruta, G Ghiringhelli, V Bisogni, L Braicovich, NB Brookes, A Tebano, and G Balestrino. Orbital occupation, atomic moments, and magnetic ordering at interfaces of manganite thin films. *Physical Review B*, 80(1):014431, 2009. 154

[126] M Huijben, LW Martin, Y-H Chu, MB Holcomb, P Yu, G Rijnders, DHA Blank, and R Ramesh. Critical thickness and orbital ordering in ultrathin $La_{0.67}Sr_{0.33}MnO_3$ films. *Physical Review B*, 78(9):094413, 2008. 154

[127] A Tebano, C Aruta, Simone Sanna, PG Medaglia, G Balestrino, AA Sidorenko, R De Renzi, G Ghiringhelli, L Braicovich, V Bisogni, et al. Evidence of orbital reconstruction at interfaces in ultrathin $La_{0.67}Sr_{0.33}MnO_3$ films. *Physical review letters*, 100(13):137401, 2008. 154

[128] Josep Nogués and Ivan K Schuller. Exchange bias. *Journal of Magnetism and Magnetic Materials*, 192(2):203–232, 1999. 160

[129] T Gredig, IN Krivorotov, P Eames, and E Dan Dahlberg. Unidirectional coercivity enhancement in exchange-biased co/coo. *Applied physics letters*, 81(7):1270–1272, 2002. 160, 163

[130] Mannan Ali, Patrick Adie, Christopher H Marrows, Denis Greig, Bryan J Hickey, and Robert L Stamps. Exchange bias using a spin glass. *Nature Materials*, 6(1):70–75, 2007. 161

[131] Kurt Binder and A Peter Young. Spin glasses: Experimental facts, theoretical concepts, and open questions. *Reviews of Modern physics*, 58(4):801, 1986. 161

[132] B Cui, C Song, GY Wang, HJ Mao, F Zeng, and F Pan. Strain engineering induced interfacial self-assembly and intrinsic exchange bias in a manganite perovskite film. *Scientific reports*, 3:2542, 2013. 161

[133] D Schumacher, A Steffen, J Voigt, J Schubert, Th Brückel, H Ambaye, and V Lauter. Inducing exchange bias in la 0.67 sr 0.33 mno 3- δ/srtio 3 thin films by strain and oxygen deficiency. *Physical Review B*, 88(14):144427, 2013. 162

[134] Patrick M Woodward. Octahedral tilting in perovskites. i. geometrical considerations. *Acta Crystallographica Section B: Structural Science*, 53(1):32–43, 1997. 178

[135] Patrick M Woodward. Octahedral tilting in perovskites. ii. structure stabilizing forces. *Acta Crystallographica Section B: Structural Science*, 53(1):44–66, 1997. 178

Appendix A
Glazer's notation for octahedral tilt

In ABO_3 perovskite structures, the tilt and rotation of octahedral can drastically change the electronic and magnetic properties of the material. Hence, quantification of the various types of tilt with respect to the symmetry of the crystal structure is important. The changes in unit cell symmetry due to octahedral tilt and rotation has been systematically studies by Glazer [113] and later further studied by Woodward [134, 135]. Since Glazer's notation is widely used in the literature, this notation is introduced in this section.

In provskite structures it is helpful to study the tilting of the octahedron about three symmetry axes. For small tilt angles, it is a reasonable assumption that the tilt is about the pseudocubic axes. For large angle tilts the order of tilt is important, while for small angle tilt the order of tilting is only second order effect. In this notation, the magnitude of tilts is indicated by three letters a,b and c which each refer to the axes of rotation [100], [010] and [001], respectively. For example, aac means that there is an equal tilt around [100] and [010] while there is a different tilt around [001]. The tilt in consecutive layers along tilt axis, between corner shared octahedrans, can be in the same direction, in-phase or opposite direction, out-of-phase that is shown by superscript + and -, respectively. If there is no tilt then the superscript is 0. In this notation, The assumption is that the three tilt direction are not coupled and are independent. Fig.A.1 shows the two stacked layers of octahedra. The tilt is only about c-axis [001], and there is no tilt along [100] and [010] direction, therefor this system is shown by "$a^0a^0c^-$". [13]

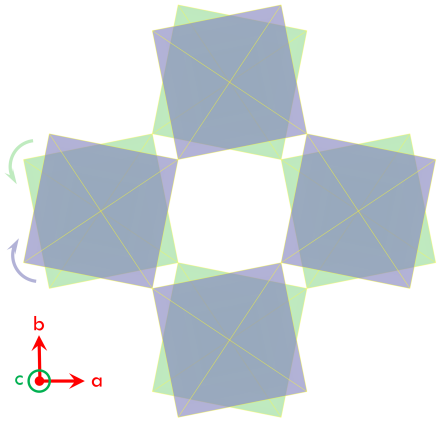

Figure A.1: An example of $a^0a^0c^-$ tilt in Glazer's notation.

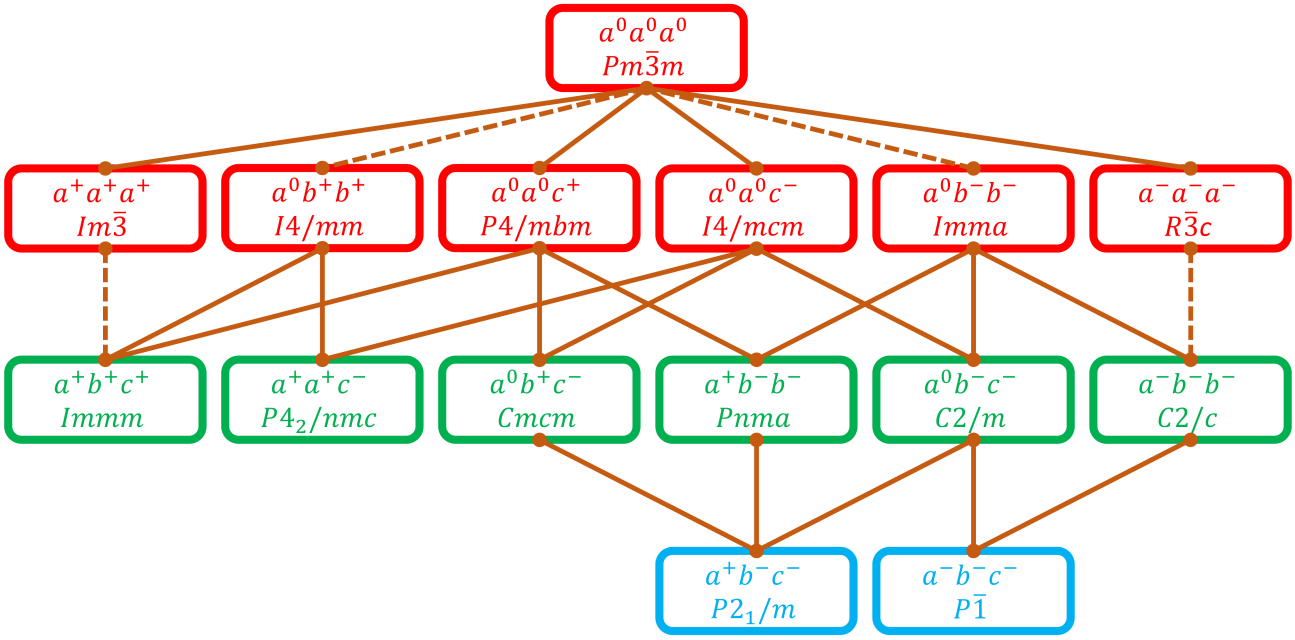

Figure A.2: Schematic diagram shows the group relations among 15 space groups from cubic perovskite to triclinic symmetry. The dash line from a group to a sub-group indicates that the transition is first order as requited by Landau theory. The figure is re-created from Ref. [13]

Vita

Mohammad Saghayezhian was born in July 1986 in Dezfoul, Khuzestan province, Iran. He finished his undergraduate degree in physics in the department of basic sciences in Shahed University in June 2008. Immediately after, he started his master degree at Isfahan university of technology and graduated in May 2011. He entered Louisiana State University in August 2011 as a PhD candidate in department of physics and astronomy. He is expected to graduate with a doctor of philosophy degree in condensed matter physics in May 2017.